

# Università degli Studi di Milano Bicocca

Department of Physics

PhD program in Physics and Astronomy, Cycle XXXV



A new electronic Readout for Kinetic inductance detectors for  
the experiment COSMO

**Surname: Limonta Name: Andrea**

**Registration Number: 726837**

**Tutor: Mario Zannoni**

**Coordinator: Stefano Ragazzi**

**ACADEMIC YEARS 2019/2023**

*To my parents*

*Who gave me life*

*To Marika and Simone*

*who have become my life*

# Contents

|   |           |
|---|-----------|
| <b>Introduction</b>                               | <b>1</b>  |
| 0.1 Olber's Paradox . . . . .                     | 3         |
| 0.2 Hubble's Law . . . . .                        | 4         |
| <b>1 CMB</b>                                      | <b>6</b>  |
| 1.1 Hystory of CMB . . . . .                      | 7         |
| 1.2 Spectral Distortions . . . . .                | 9         |
| 1.2.1 Thermalization Era . . . . .                | 11        |
| 1.2.2 $\mu$ -distortion era . . . . .             | 12        |
| 1.2.3 $\gamma$ -distortion era . . . . .          | 13        |
| <b>2 COSMO</b>                                    | <b>15</b> |
| 2.1 Subsystem . . . . .                           | 17        |
| 2.1.1 The Shelter . . . . .                       | 17        |
| 2.1.2 The Cryogenic System . . . . .              | 17        |
| 2.1.3 Sky Scanner . . . . .                       | 19        |
| 2.1.4 The Forebaffle . . . . .                    | 19        |
| 2.1.5 The Telescope and FTS . . . . .             | 20        |
| 2.1.6 Reference Blackbody . . . . .               | 21        |
| 2.1.7 Delay Line Cryomechanism . . . . .          | 21        |
| 2.1.8 The Multimode Feed Arrays . . . . .         | 23        |
| <b>3 KIDS</b>                                     | <b>26</b> |
| 3.1 Superconductivity . . . . .                   | 27        |
| 3.1.1 The impedance of a superconductor . . . . . | 33        |
| 3.1.2 Photon detection . . . . .                  | 34        |
| 3.2 Lumped Element Kinetic Inductance . . . . .   | 36        |
| 3.2.1 Scattering parameters . . . . .             | 37        |

|          |   |           |
|----------|---|-----------|
| 3.2.2    | S21 gain parameter . . . . .                | 39        |
| 3.2.3    | Parameter S21, real and imaginary . . . . . | 42        |
| 3.2.4    | Increase sensitivity . . . . .              | 44        |
| <b>4</b> | <b>Electronic Readout</b>                   | <b>46</b> |
| 4.1      | Operation of the state machine . . . . .    | 47        |
| 4.1.1    | First State . . . . .                       | 47        |
| 4.1.2    | Second State . . . . .                      | 49        |
| 4.1.3    | Third State . . . . .                       | 50        |
| 4.2      | Hardware . . . . .                          | 52        |
| 4.2.1    | Cryostat . . . . .                          | 55        |
| 4.3      | Software . . . . .                          | 57        |
| 4.3.1    | FPGA . . . . .                              | 57        |
| 4.3.2    | Host Computer . . . . .                     | 59        |
| <b>5</b> | <b>Laboratory measurement</b>               | <b>63</b> |
| 5.1      | Measurements with KIDs . . . . .            | 68        |
| 5.2      | Measurement of Warm and Cold Loop . . . . . | 71        |
| 5.2.1    | Warm Loop . . . . .                         | 73        |
| 5.2.2    | Cold Loop . . . . .                         | 76        |
| 5.3      | New measurement . . . . .                   | 80        |
| 5.4      | Comparison with other experiments . . . . . | 86        |
|          | <b>Conclusions</b>                          | <b>88</b> |

# List of Figures

|     |  |    |
|-----|--|----|
| 1.1 | The FIRAS experiment result on CMB. The dot represents the data founded by the experiment, with an error multiplied by $400\sigma$ to be visible in the graph. The solid line represents a theoretical blackbody curve. . . . .  | 6  |
| 1.2 | Evolution of data about CMB. On the far left the anisotropies founded by Cobe in 1992, next the anisotropies founded by WMAP in 2003 an on the right the anisotropies founded by Planck in 2013. . . . .   | 8  |
| 1.3 | Predicted spectra of E and B modes. The blue lines represent the B-mode. The parameter $r$ is the amplitude of the gravity wave spectrum relative to the density perturbation of the spectrum. Current experiment constrain $r = 0.3$ , value of $r$ as low as 0.01 should be attainable in the future experiments. The curves labeled EPIC show the noise levels of the experiment EPIC, the dashed curves labeled "WMAP" and "Planck" are the statistical noise limits for these satellites.[14] . . . . . | 9  |
| 1.4 | Evolution of Big Bang. A $\mu$ -type distortion arises from energy is created at redshift $5 * 10^4 < z < 2 * 10^6$ , while a $y$ -type arises at $z \leq 5 * 10^4$ .[15] .  | 10 |
| 1.5 | Evolution of spectral distortion across time. The distortions are a probe for the thermal history, deep into the primordial Universe. The shape of the distortion contains information dependent from the epoch. . . . .   | 11 |
| 1.6 | CMB spectral distortion, from the temperature shift (in red), to the pure $\mu$ -distortion appearing at $z \cong 3 * 10^5$ (in blue) and eventually the $y$ -distortion (in black). At all intermediate stages the signal is given by a superposition of the cases. . . . .   | 14 |

|      |   |    |
|------|---|----|
| 2.1  | Geometry of the sky scan for the COSMO experiment. Left: the COSMO instrument with the external spinning wedged flat mirror. The arrows identifies the spin axis, while the mirror is sketched in two positions (red and blue) corresponding to maximum and minimum elevation of the beams. Right: Resulting scan of the beam over the celestial sphere. The blue and red spot mark the maximum and minimum elevatons explored by the beam. | 16 |
| 2.2  | Example of expected interferogram obtained while the flat wedged mirror is spinning. The zoomed inset shows how the interferograms, corresponding to the maximum and minimum elevations, can be obtained by properly resampling the measured interferogram.   | 16 |
| 2.3  | 3d rendering of the COSMO's FTS with an insight of the inner vessel housing the optical elements and the blackbody.   | 17 |
| 2.4  | 3d rendering of the COSMO's stilt house and shelter   | 18 |
| 2.5  | 3d rendering of the COSMO cryogenic system  | 19 |
| 2.6  | The strategy for the sky scanner of COSMO, using the azimuth-elevation control system   | 20 |
| 2.7  | The design of the forebaffle with respect to the scanning beam to envelope  | 20 |
| 2.8  | Machine shop drawing for the forebaffle assembly of the COSMO experiment  | 21 |
| 2.9  | Left: ray tracing of COSMO. Right: position of the component inside the cryostat of COSMO. L1-2-3 are the optics, BSP is the beam splitter, RF1-2 the roof mirror and FP1-FP2 the focal planes.   | 22 |
| 2.10 | Left: inner mold for the reference blackbody (scaled model). Right: outer mold for the reference blackbody  | 22 |
| 2.11 | Roof-mirror for COSMO   | 23 |
| 2.12 | Top left and bottom: Feedhorns assemblies for the low frequency array. Top right: Feedhorns assemblies for the high frequency array   | 24 |

|      |   |    |
|------|---|----|
| 3.1  | Representative geometry of a Lumped Element Kinetic Inductance Detectors, on the left a plan view with the substrate thickness making up the third dimension. . . . .   | 27 |
| 3.2  | Cooper Pair; the first electron (right) moves in the ion lattice distorting it and the second chases the positive charge left by the distortion. . . . .  | 28 |
| 3.3  | London Penetration in a superconducting material: the magnetic field within the material is quickly expelled. . . . .   | 29 |
| 3.4  | Two-fluid model equivalent, we assume two types of carriers, on the left the Cooper pair witha dissipation for the alternating current and on the right side the quasiparticles, which behave like classical electrons . . . . .  | 31 |
| 3.5  | Difference from thick and thin film and the current flow on the surface of the material. . . . .  | 33 |
| 3.6  | Left: working principle of KIDs. A Cooper pair is destroyed by a photon with sufficient energy, modifying the impedance of the circuit and modifying the amplitude and phase of the signal. Right: array of KIDs with different resonance frequencies . . . . .   | 35 |
| 3.7  | Left: The LEKID equivalent circuit. Right: a schematic of a LEKID device. $M$ is the mutual inductance between the LEKID and the feedline, $R$ is the resistance of the meander section, $L_{ext} + L_{int}$ is the total inductance of the meander section, $C$ is the capacitance and $G$ is the conductance of the inter-digital capacitor section respectively. . . . . | 36 |
| 3.8  | Scattering Parameter . . . . .  | 38 |
| 3.9  | The ABCD matrix formalism. . . . .  | 38 |
| 3.10 | Schematic of a LEKID . . . . .  | 40 |
| 4.1  | The logic of the finite state machine. . . . .  | 47 |
| 4.2  | Example of a chirp signal . . . . .   | 48 |
| 4.3  | The result of the chirp through the KIDs. We can see all the resonances of our array of KIDs . . . . .  | 49 |

|      |   |    |
|------|---|----|
| 4.4  | Comparison of the result of a generated signal with a different number of iteration. . . . .  | 50 |
| 4.5  | Logic of the Channelization process. . . . .  | 50 |
| 4.6  | Logic block of the Direct Down Conversion . . . . .   | 51 |
| 4.7  | Block Diagram of the readout electronic. To cover a wider band, the signal is generated by 2 transceiver, added together by a Wilkinsons power splitter and attenuated by an attenuator before entering the cryocooler. Before being received by the transeiver the signal is split by an identical Wilkinsons. | 52 |
| 4.8  | The insulated rack with all the warm electronic components. . . . .   | 53 |
| 4.9  | Inside of the cryostat, with all the cold component of the set-up. . . . .  | 56 |
| 4.10 | Block diagram for the writing of the Look-up table on the FPGA. The data are stored in memory as an array of U32 elements, with the top 16 bit representing the I signal and the bottom 16 bit representing the Q signal. .   | 58 |
| 4.11 | Block diagram for the transmission of the signals. Cyan rectangle: the reading of the Look-up table. Red rectangle: DSP of every element I and Q. Orange rectangle: transmission of the I and Q element to the DAC . .  | 59 |
| 4.12 | Block diagram to receive the signals. The signal pass through a DSP before being sent to the host as an U32 element. . . . .  | 59 |
| 4.13 | GUI for the host. The graph show the comb received from the ADC of the NI 5791 . . . . .  | 60 |
| 4.14 | Generation of the Chirp signal . . . . .  | 61 |
| 4.15 | DDC block logic. The signal received as a Waveform pass through a DDS (Direct Digital Synthesis), a low passfilter and a downsampler, them for each element the phase and the amplitude of the signal is calculated. . . .  | 62 |
| 5.1  | Design of the array of 25 Niobium KIDs, from Astroparticule et Cosmologie lab in Paris. . . . .   | 64 |
| 5.2  | The sweep response of the 25 Niobium Kids. 23 resonance are visible in the figure. . . . .  | 64 |

|      |   |    |
|------|---|----|
| 5.3  | The result of the chirp through the KIDs. We can see all the resonances of our array of KIDs . . . . .  | 68 |
| 5.4  | Blue: temperature oscillation. Red: phase oscillation of the tone at 2.0093 GHz. Yellow: phase oscillation of the test tone at 1.9760 GHz. . . . .  | 69 |
| 5.5  | IQ for the tone at frequency 2.0093 GHz . . . . .   | 70 |
| 5.6  | IQ for the test tone at frequency 1.9760 GHz . . . . .  | 70 |
| 5.7  | Phase Noise for the tone at frequency 2.0093 GHz. . . . .   | 71 |
| 5.8  | Phase Noise for the test tone at frequency 1.9760 GHz. . . . .  | 71 |
| 5.9  | Sample of detected Phase for the tone at frequency 2.0093 GHz. . . . .  | 74 |
| 5.10 | Sample of detected Phase for the test tone at frequency 1.9760 GHz. . . . .   | 74 |
| 5.11 | IQ for the tone at frequency 2.0093 GHz. . . . .  | 75 |
| 5.12 | IQ for the test tone at frequency 1.9760 GHz. . . . .   | 75 |
| 5.13 | Phase Noise for the tone at frequency 2.0093 GHz. . . . .   | 76 |
| 5.14 | Phase Noise for the test tone at frequency 1.9760 GHz. . . . .  | 76 |
| 5.15 | Phase for the tone at frequency 2.0093 GHz. . . . .   | 78 |
| 5.16 | Phase for the test tone at frequency 1.9760 GHz. . . . .  | 78 |
| 5.17 | IQ for the tone at frequency 2.0093 GHz. . . . .  | 79 |
| 5.18 | IQ for the test tone at frequency 1.9760 GHz. . . . .   | 79 |
| 5.19 | Phase Noise for the tone at frequency 2.0093 GHz. . . . .   | 80 |
| 5.20 | Phase Noise for the test tone at frequency 1.9760 GHz. . . . .  | 80 |
| 5.21 | Chunk of the phase time stream. The test tone (frequency 1.976 GHz) is plotted in orange, the resonant tone (2.00940 GHz) is in red and the temperature oscillations are in blue. . . . .                                 | 83 |
| 5.22 | Amplitude and temperature time stream. The resonant tone (2.00940 GHz) is in red and the temperature is in blue. . . . .  | 84 |
| 5.23 | Phase noise of the reference tone (2.00940 GHz) in three different conditions. Up: when the signal passes through the KIDs. Middle: when there are no KIDs. Down: when the signal does not enter in the cryostat. . . . . | 85 |

5.24 Phase noise of the test tone (1.976 GHz) in three different conditions. Up: when the signal passes through the KIDs. Middle: when there are no KIDs. Down: when the signal does not enter in the cryostat. . . . . 85

5.25 Noise calculated by the experiment OLIMPO . . . . . 86

5.26 Noise calculated by the experiment Origins Space Telescope . . . . . 87

5.27 Noise calculated by the Demonstration Instrument "DemoCam" as a function of power, under 77 K load. The horizontal black line is drawn at  $6 * 10^{-16} W / \sqrt{Hz}$  for a scale relationship. . . . . 87

5.28 The configuration for the new electronic readout of COSMO . . . . . 89

5.29 The new electronics placed on the plate for the insulated rack. . . . . 90

# Introduction

Since ancient times humanity has wondered about every aspect of physics and science, a Latin word that means "Knowledge". Humanity's interest in understanding natural phenomena in the physical world goes hand in hand with man's history itself: starting from prehistory, the discovery of fire, the development of agriculture, then the first physical laws still used today (just think of Archimedes' principle, formulated in 250 BC by Archimedes of Syracuse), to bring man to the moon and arriving to the present day, with the development of the first quantum technologies.

The use of new technologies and new tools also involves the development of suitable electronics electronic readout for Kinetic Inductance Detectors, using commercial components and without depending on the use of pre-existing technologies, which currently do not reach the specifications necessary for the experiment. The development of electronic readout for cryogenic detectors is a key factor for any field of study. However, one of the most interesting and most important studies for mankind is cosmology: the study of the universe as a whole, of which it attempts to explain its origin and evolution. Although it has very ancient origins, only in 1917 we can speak of Modern Cosmology, thanks to the formulation of general relativity by Einstein, and to the construction of the metric by Friedmann-Lemaitre-Robertson-Walker.[1]

Generally, the 4-dimensional metric can be described by:

$$ds^2 = -c^2 dt^2 + dr^2 + r^2 d\Omega^2 \quad (1)$$

From general relativity the curvature of spacetime can be very complicated, however if the universe is homogeneous and isotropic, according to the principle of cosmology, then we can reduce to 3 cases: flat with euclidean metric, positive curvature and negative curvature. The Friedmann-Lemaitre-Robertson-Walker can be written as:

$$ds^2 = -c^2 dt^2 + a^2(t) [dr^2 + S_k(r^2) d\Omega^2] \quad (2)$$

$S_k(r^2)$  depends on the value of  $k$ , the constant curvature:

$$\begin{aligned}
 S_k(r^2) &= R_0^2 \sin^2\left(\frac{r}{R_0}\right) \quad \text{for } k = 1 \\
 S_k(r^2) &= r^2 \quad \text{for } k = 0 \\
 S_k(r^2) &= R_0^2 \sinh^2\left(\frac{r}{R_0}\right) \quad \text{for } k = -1
 \end{aligned} \tag{3}$$

The assumption of an homogeneous and isotropic universe is extremely powerful. With this assumption, all we need to know about spacetime curvature are:

- curvature constant ( $k = 1, 0, -1$ )
- radius of curvature  $R_0$  (if  $k$  different from 0)
- scale factor  $a(t)$

Other important variable:

- $t$  is the cosmic (or proper) time, measured by an observer seeing an isotropic expansion
- $r$  is the proper distance, the distance between us and any point measured today, at time  $t_0$ .

The curvature of spacetime is related to its energy content by Einstein's Field equation:

$$G_{\mu\nu} = \frac{8\pi G}{c^4} T_{\mu\nu} \tag{4}$$

If space is homogeneous and isotropic, this reduces to the Friedmann equation:

$$\left(\frac{\dot{a}}{a}\right)^2 = \frac{8\pi G}{3c^2} \varepsilon(t) - \frac{kc^2}{R_0^2} \frac{1}{a(t)^2} \tag{5}$$

where  $G$  is the Einstein Tensor and  $\varepsilon(t)$  is the energy density.

One of the most classic errors one can fall into when speaking of cosmology is the idea that it arises only from theoretical studies, not supported by real observations: on the contrary, the basis of all cosmology is determined by 3 very important observations: Olber's paradox, Hubble's law and the CMB.

## 0.1 Olber's Paradox

Olber's paradox[2] is an extremely simple observation on a phenomenon that we have all observed in our lives: it gets dark at night. As simple as it may seem, it hides a very important question. The brightness of the dark sky is measured as:

$$\Sigma_{night} \sim 5 * 10^{-17} \frac{W}{m^2 arcsec^2} \quad (6)$$

while the day is:

$$\Sigma_{day} \sim 5 * 10^{-3} \frac{W}{m^2 arcsec^2} \quad (7)$$

The question is: why is the night sky dark? Why is not glowing as if it was uniformly covered by stars? Assuming a cylinder starting from our eye and with a diameter equal to that of the sun and with an height of  $\lambda$ , how big  $\lambda$  must be (on average) to contain at least one star, given the density of stars we know? The density of stars we know is:

$$n \sim \frac{10^9}{Mpc^3} \quad (8)$$

Assuming a star of radius  $R = 7 * 10^8 m$  we can calculate:

$$\begin{aligned} V * n &= 1 \\ [\lambda \pi R^2] * n &= 1 \\ \lambda &= \frac{1}{\pi R^2 * n} \sim 10^{18} Mpc \end{aligned} \quad (9)$$

It's a finite number! In an infinite universe, or greater in radius than  $\lambda$ , we should see the sky completely filled with stars, but we know it is about 14 orders of magnitude less bright! There are different possible solutions, the one that is adopted and is explainable with the standard model is that the universe as a finite age ( $ct \ll 10^{18} Mpc$ ), that is a finite dimension.

## 0.2 Hubble's Law

When we take the spectrum of a galaxy, we observe that the absorption lines of a known element, like the 21 centimeter Hydrogen line, are different from the lines that we measure on Earth. The wavelength shift due to the Doppler effect is indicated by  $z$ :

$$z = \frac{\lambda_0 - \lambda_e}{\lambda_e} \quad (10)$$

with  $\lambda_0$  the observed value and  $\lambda_e$  the emitted value. In the 1923 Vesto Slipher[3] measured the Doppler shift of 41 galaxy. 31 had  $z > 0$  (redshift) only 5 had  $z < 0$  (blueshift). In 1929 Edwin Hubble[4] measured the distance of the galaxy in Andromeda (M31), and some others founding a linear relation, known as Hubble's Law, that links the distance of a galaxy to his redshift:

$$z = \frac{H_0}{c} r \quad (11)$$

Where  $H_0$  is the Hubble constant. Hubble interpreted the observed redshift of galaxies due to their radial velocity away from Earth. Today the best current estimate of the Hubble Constant is[5]:

$$H_0 \sim 67.4 \pm 0.5 \frac{Km/s}{Mpc} \quad (12)$$

It is possible to connect the expansion law and the scale factor  $a(t)$  to the Hubble law, as:

$$r_{ij}(t) = a(t)r_{ij}(t_0) \quad (13)$$

where the scale factor  $a(t)$  is totally independent of location or direction. This means that the scale factor is:

- Homogeneous:  $a$  is function of  $t$ , but not of  $\vec{r}$
- Isotropic:  $a$  is a scalar, not a tensor
- $a(t_0) = 1$  by convention

Note that Hubble's law is consistent with the Big Bang, but does not necessarily require it. The Steady State, a rival cosmological model, was totally compatible until the Cosmic Microwave Background was discovered.

# 1. CMB

The Cosmic Microwave Background was founded while not being searched by the physicist Arno Allan Penzias and Radio-Astronomer Robert Woodrow Wilson in the 1964. While taking measurements with an antenna in the Crawford Hill labs, they found an effective zenith noise 3.5 K higher than expected. As they stated [6] they could not explain the mechanism behind this phenomenon, first of all trying to eliminate it believing it was a systematic error, by cleaning the antenna thoroughly. Only later, learning of a paper on the theory of CMB [7], they linked this effect to cosmic radiation hitherto only theorized, and what they had found coincided with the radiation predicted by Robert H. Dicke.

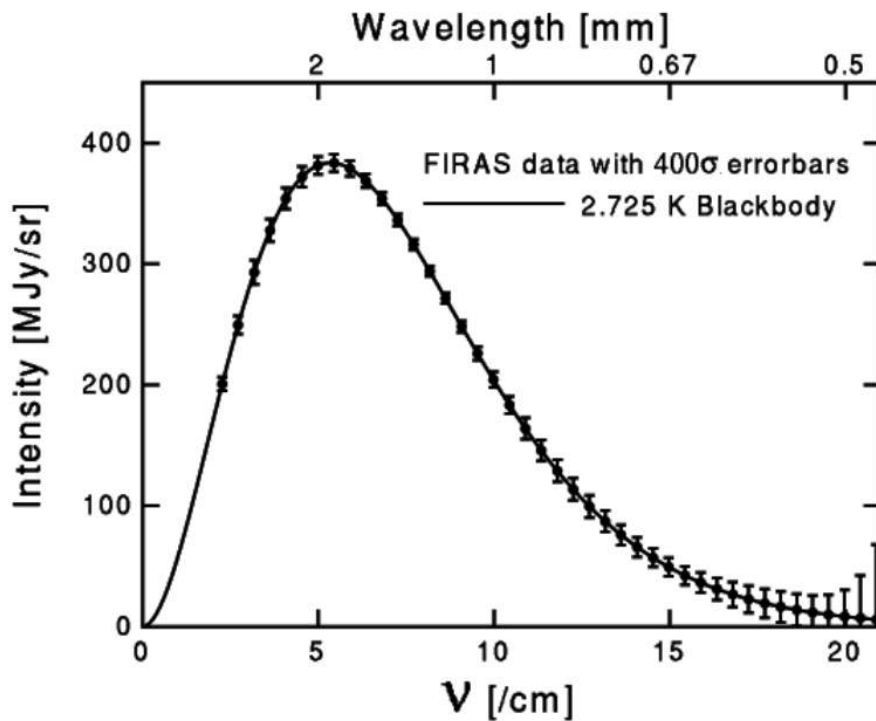


Figure 1.1: The FIRAS experiment result on CMB. The dot represents the data founded by the experiment, with an error multiplied by  $400\sigma$  to be visible in the graph. The solid line represents a theoretical blackbody curve.

## 1.1 Hystory of CMB

The CMB has a black body spectrum with a temperature of  $2.72548 \pm 0.00057K$  [8] as found by FIRAS experiment on board COBE satellite (see fig. 1.1). In the last 25 years, numerous instruments from the ground, from balloons - including Boomerang [9] - and from space - such as the WMAP[10] and Planck satellites[11] - have accurately measured the CMB anisotropies up to angular scales of a few arcminutes, giving us the currently most precise determination, in the order of percent, of the cosmological parameters that characterize the constituents and the evolution of the universe. Thanks to these measurements, we know that our universe is composed of 95% dark matter and energy and 5% ordinary matter, has a flat spatial geometry, and agrees with the predictions of inflation theory, which describes a phase of accelerated expansion in which the primordial density perturbations were generated by quantum fluctuations.

Although two Nobel prizes have already been awarded, the CMB is still a mine of information for cosmology and fundamental physics, with a constant evolution on the resolution of the data analyzed (see fig. 1.2). An ever more accurate measurement of CMB polarization anisotropies – smaller than those in temperatures by at least one order of magnitude – remains one of the frontiers in this field (see fig. 1.3). From a more accurate measurement of mode E in polarization, revealed for the first time by the DASI (Degree Angular Scale Interferometer) instrument [12] at the South Pole in 2002, it will be possible to know how the era of reionization developed or to better characterize the properties of dark matter. Polarization mode B is instead produced by gravitational waves generated during inflation, of a wavelength nine orders of magnitude greater than those detected by LIGO [13] and generated by the coalescence of black holes.

Recently, one of the most interesting aspects of the CMB, the spectral distortions, gained new interest.

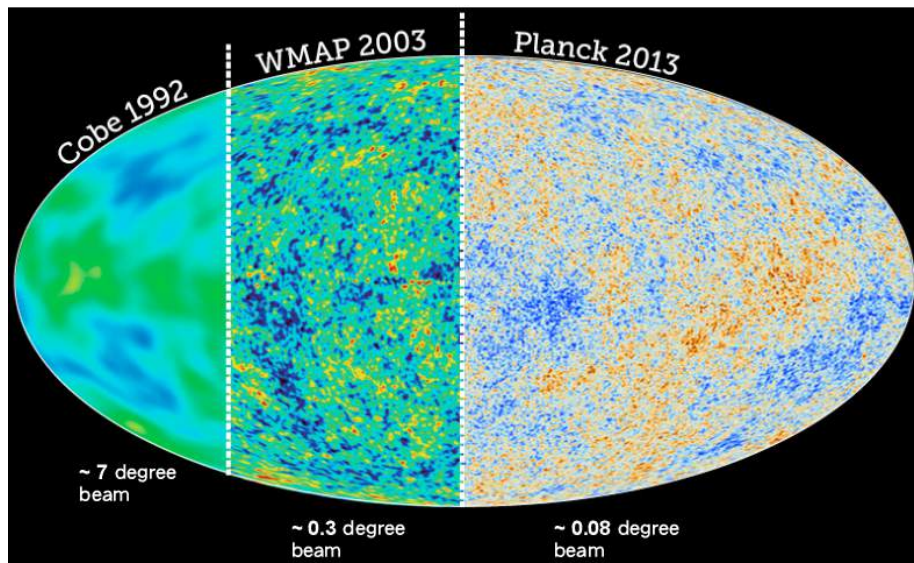


Figure 1.2: Evolution of data about CMB. On the far left the anisotropies founded by Cobe in 1992, next the anisotropies founded by WMAP in 2003 an on the right the anisotropies founded by Planck in 2013.

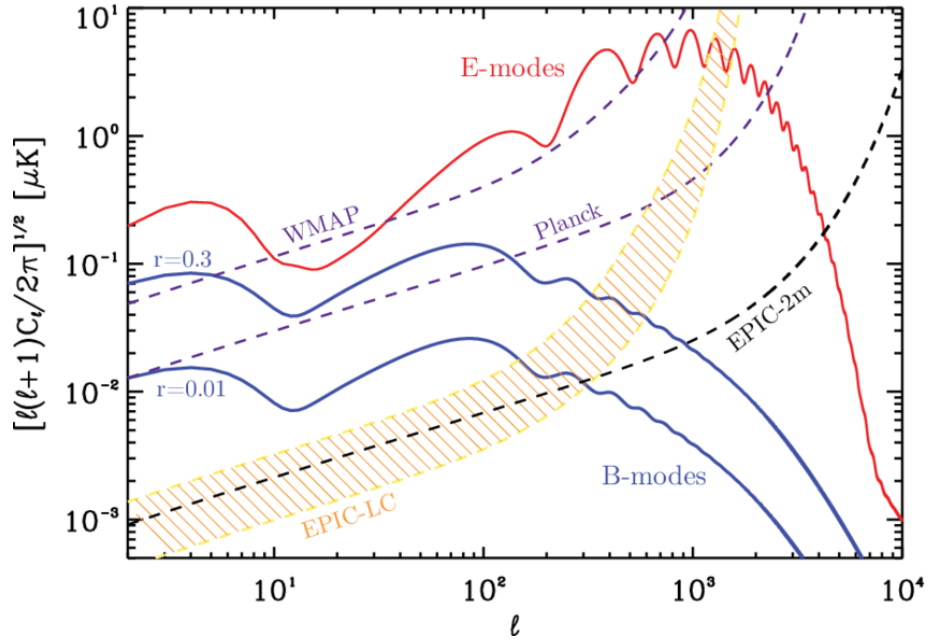


Figure 1.3: Predicted spectra of E and B modes. The blue lines represent the B-mode. The parameter  $r$  is the amplitude of the gravity wave spectrum relative to the density perturbation of the spectrum. Current experiment constrain  $r = 0.3$ , value of  $r$  as low as 0.01 should be attainable in the future experiments. The curves labeled EPIC show the noise levels of the experiment EPIC, the dashed curves labeled "WMAP" and "Planck" are the statistical noise limits for these satellites.[14]

## 1.2 Spectral Distortions

The CMB spectral distortions are small differences from the average value of the CMB frequency spectrum as predicted by a perfect black body. They can be produced by processes that occurred in the earliest cosmological eras and therefore are a useful tool for probing these periods. We must not confuse the spectral distortions of the CMB with the anisotropies of the angular power spectrum, the latter related to the spatial fluctuations of the temperature of the CMB in different points of the sky.

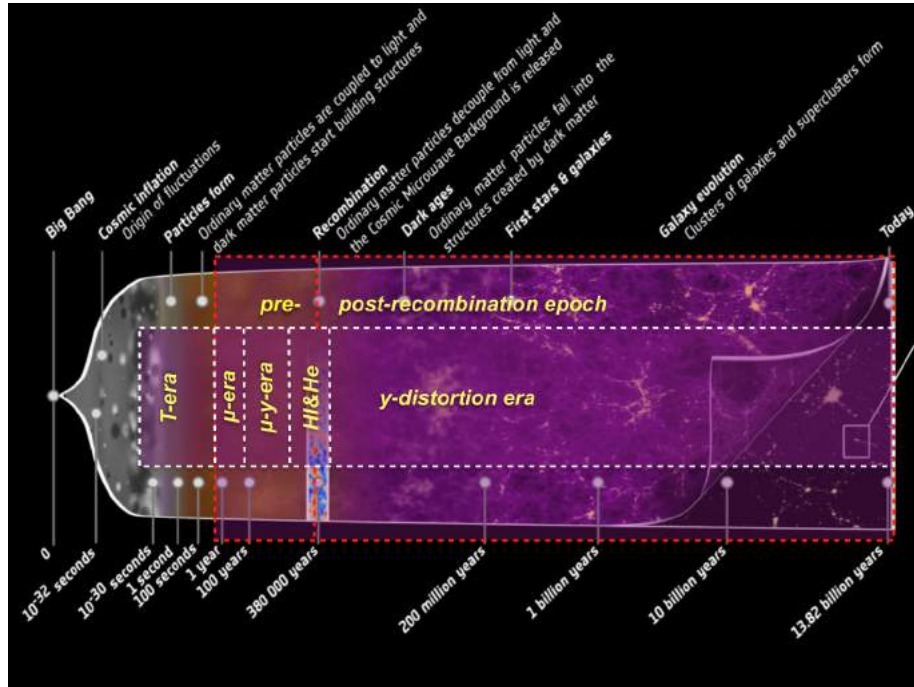


Figure 1.4: Evolution of Big Bang. A  $\mu$ -type distortion arises from energy is created at redshift  $5 * 10^4 < z < 2 * 10^6$ , while a  $y$ -type arises at  $z \leq 5 * 10^4$ . [15]

As we have seen, the CMB has the spectrum of a black body with a temperature of  $2.72548 \pm 0.00057K$  [8]. However, at redshift  $z < 2 * 10^6$  many mechanisms come into play that can modify the CMB spectrum, introducing differences from an ideal black body spectrum. These differences are known as spectral distortions and are related to the average of the CMB spectrum across the sky, i.e. the monopole spectrum of the CMB. The main source of spectral distortions is the injection of energy in the early Universe, for example due to the decay of particles, the evaporation of primordial black holes or the dissipation of acoustic waves generated by Inflation [16]. Because of the injection of energy, the baryons heat up and transfer some of their excess energy to the photon bath of the CMB via Compton scattering. This can cause a distortion which can be characterized by the  $\mu$  and  $y$  parameters. These dimensionless parameters represent a measure of the total energy input into the CMB. For this reason, spectral distortions represent a powerful probe for early-universe physics and an estimate of the epoch at which these injections occur. The observational limit was set in 1990 by the COBE-FIRAS experiment with  $|\mu| < 9 * 10^{-5}$  and  $|y| < 1.5 * 10^{-5}$  with a 95% confidence level. TRIS experiment [17] set

a new limit, with  $|\mu| < 6 * 10^{-5}$  and  $-6.3 * 10^{-6} < |y| < 12 * 10^{-6}$  with a 95% confidence level. From the  $\Lambda$ CDM theory we expect  $\mu \sim 2 * 10^{-8}$  and  $y \sim 1 * 10^{-6}$  [18]. These signals are extremely weak, the largest distortion, generated by the cumulative flux of all the hot phases of the universe, has an amplitude of an order of magnitude smaller than of the COBE-FIRAS limit.[18]

Going into more detail, let's try to explain the differences of these spectral distortions. There are 3 distinguishable eras: the thermalization, the  $\mu$ -era and the  $y$ -era (see fig. 1.4 and fig. 1.5, all with different physical conditions due to the temperature-density variations of the particles caused by the Hubble expansion.[19]

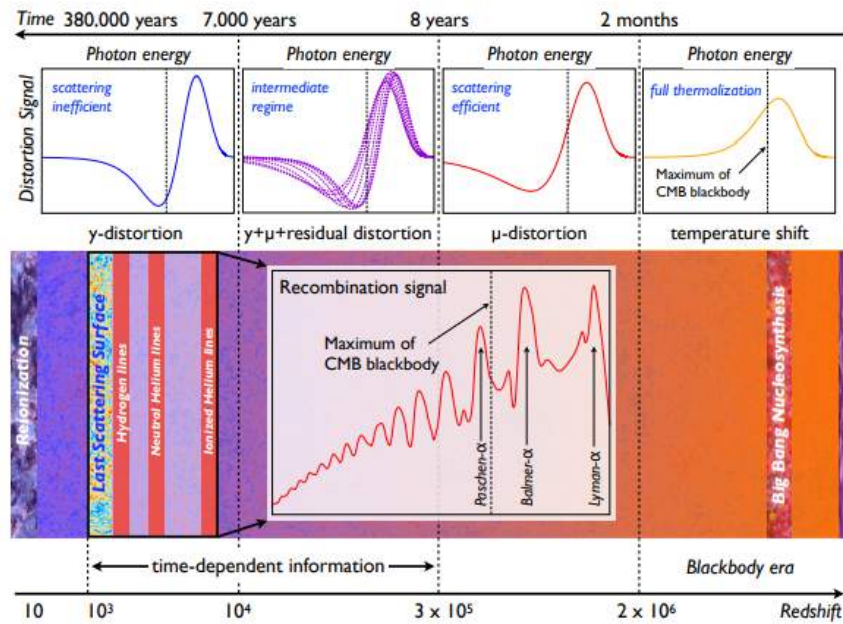


Figure 1.5: Evolution of spectral distortion across time. The distortions are a probe for the thermal history, deep into the primordial Universe. The shape of the distortion contains information dependent from the epoch.

### 1.2.1 Thermalization Era

In the very early stages of cosmic history [19] (until redshift  $z \sim 2 * 10^6$ ), photons and baryons are efficiently coupled by scattering processes and therefore are in perfect ther-

modynamic equilibrium. The energy injected into the medium is rapidly redistributed by photons, mainly by Compton scattering while the photon number density adjusts by non-conservative photonic processes, such as for example double Compton, and thermal Bremsstrahlung. This allows the photon field to relax rapidly to the Planckian distribution, even if short spectral distortions appear. Today's observations cannot notice any differences in this case, since there are no independent cosmological predictions for the CMB temperature monopole. This regime is defined as thermalization or thermal-era and ends at a redshift  $z \sim 2 * 10^6$ .

### 1.2.2 $\mu$ -distortion era

At redshift  $5 * 10^4 < z < 2 * 10^6$  the efficient exchange of energy through Compton scattering continues and maintains the kinetic equilibrium between matter and radiation, but the process of density variations stops being efficient. Since the photon number density is conserved but the energy density is changed, the photons gain an effectively non-zero chemical potential, and acquire a Bose-Einstein distribution. This distortion is called  $\mu$ -distortion due to the known chemical potential in standard thermodynamics. Its value can be estimated by combining the photon energy density and the photon number density before and after the energy injection. This leads to the formula[20]:

$$\mu \sim 1.4 \frac{\Delta\rho}{\rho} \tag{1.1}$$

where  $\frac{\Delta\rho}{\rho}$  determines the total energy that is injected into the photon field of the CMB. Compared to the equilibrium of the black body spectrum, the  $\mu$ -distortions are characterized by a deficit of photons at low frequencies and an increase of the same at high frequencies. The most significant variation occurs at  $\nu \sim 130 \text{ GHz}$ [21] allowing us to distinguish them from other distortions. It is theorized that they can be generated by particle decays, by primordial evaporation of black holes, by primordial magnetic fields and, in  $\Lambda\text{CDM}$  theory by the adiabatic cooling of matter and the dissipation of acoustic waves caused by inflation, which generate a value of  $\mu$  in the range of  $10^{-8}$ . This signal can be a powerful test for inflation, as it is sensitive in amplitude to density fluctuations on scales

of 0.6kpc[20].

### 1.2.3 y-distortion era

At redshift  $z \leq 5 * 10^4$  also Compton scattering becomes inefficient. Plasma has a temperature lower than  $10^5 K$ , low enough for the CMB photons to be accelerated by non-relativistic Compton scattering, causing a y-distortion, given by the line of sight integral over the electron pressure:

$$y = \int \frac{kT_e}{m_e c^2} N_e \sigma_T dl \quad (1.2)$$

where  $\sigma_T$  is the Thomson cross section,  $N_e$  the electron number density and  $T_e$  the electron temperature. Considering the total energies of the system and using photon number conservation, it is possible to derive [22]:

$$y \sim \frac{1}{4} \frac{\Delta\rho}{\rho} \quad (1.3)$$

The name comes from a paper published by Zeldovich and Sunyaev in 1969 [22] where they chose y to describe a dimensionless variable. The major contribution appears to come from the cumulative signal of Sunyaev-Zeldovich effect (SZ) inside Galaxy clusters [23], and providing us with a constrain to the amount of hot gases in the universe. As long as  $z < 10^4$  the cosmic plasma has on average a relatively low temperature, the electrons inside the clusters reach temperatures of a few KeV. These electrons can have velocities of  $v \sim 0.1c$ , such that relativistic corrections to Compton processes become relevant. These relativistic corrections carry electron temperature information that can be used to measure the energy of the clusters. One can demonstrate that the corresponding difference in the radiation temperature can be written as[24]:

$$\frac{\Delta T}{T} = y * \left[ \frac{e^x + 1}{e^x - 2} - 3 \right] \quad (1.4)$$

where  $x = \frac{h\nu}{kT_0}$  is the dimensionless frequency,  $\nu$  is the photon frequency,  $T_0$  is the temperature of the incoming radiation.

The final result of all the previous effects can be seen in fig. 1.6

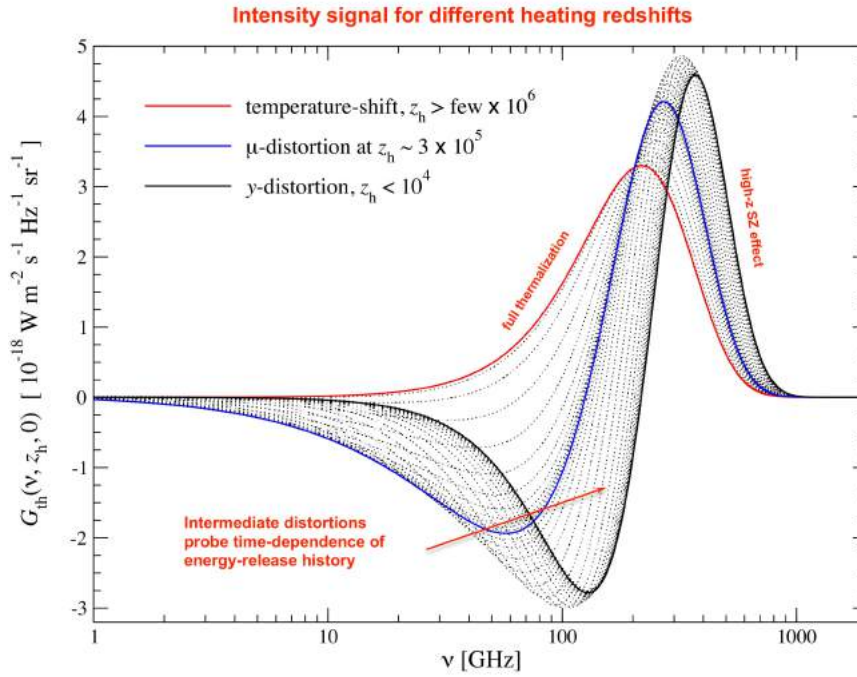


Figure 1.6: CMB spectral distortion, from the temperature shift (in red), to the pure  $\mu$ -distortion appearing at  $z \cong 3 * 10^5$  (in blue) and eventually the  $y$ -distortion (in black). At all intermediate stages the signal is given by a superposition of the cases.

## 2. COSMO

COSMO[25] is a pathfinder experiment to search for CMB spectral distortions (in fig. 2.3 a 3d rendering of the Fourier Transform Spectrometer). Although the final measurements will necessarily have to be performed from space or from a long duration stratospheric balloon, the current experiment is ground-based, in the best site in the world for this kind of measurement: the Antarctic plateau.

COSMO uses a Fourier Transform Spectrometer (FTS) in Martin-Puplett configuration[26]. The spectrometer has two input ports and is intrinsically differential, measuring the spectrum of the difference in brightness from the two inputs. In normal configuration one port looks at the sky and the other at a cryogenic internal reference blackbody. This can be described as:

$$I_{sky}(x) = R \int_0^{\infty} A\Omega(\sigma)[B_{sky}(\sigma) - B_{ref}(T_{ref}, \sigma)]e(\sigma)[\cos(4\pi\sigma x)] d\sigma \quad (2.1)$$

with  $I_{sky}(x)$  the signal measured by the detector as a function of the optical path difference  $x$  between the two mirror of the interferometer,  $\sigma = \frac{1}{\lambda}$  the wavenumber,  $A\Omega(\sigma)$  is the optical throughput of the detector,  $B_{sky}$  the sky brightness present at the input port of the sky,  $B_{ref}(T_{ref}, \sigma)$  is the brightness of the reference blackbody at temperature  $T_{ref}$  in the input port of the reference,  $e(\sigma)$  is the spectral efficiency of the instrument, the constant  $R$  is the responsivity of the instrument. The quantity  $RA\Omega(\sigma)e(\sigma)$  can be estimated using an external blackbody at a known temperature filling the input port of the sky. To coping with atmospheric emission, the COSMO instrument uses an external spinning wedged flat mirror, steering the instrument beam in the sky while spinning (see fig. 2.1). This allows a real-time separation of the atmospheric contribution, which varies with elevation, from the sky monopole (constant with elevation).

Adapting a fast enough sampling rate it is possible to follow the signal modulation due to the different elevation and consequent atmospheric loading (see fig. 2.2). In this way we can reconstruct the different interferograms for every elevation angle and disentangle the atmospheric contribution. Since the instrument measures one interferogram every few second, faster atmospheric fluctuations are impossible to sample.

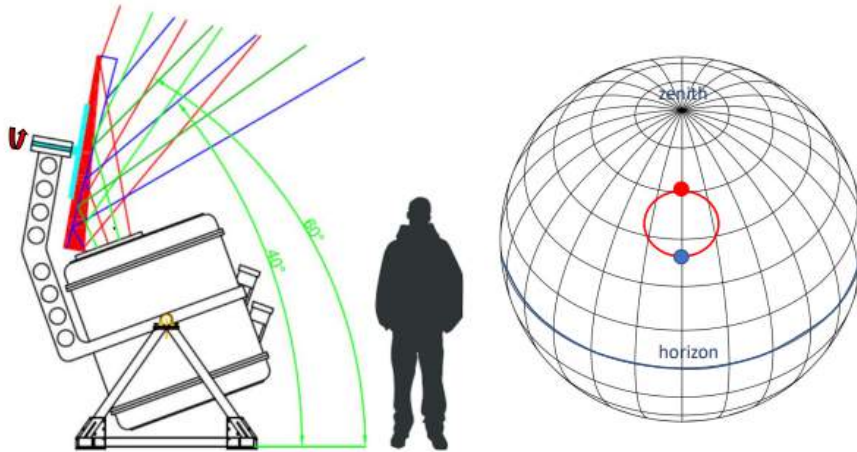


Figure 2.1: Geometry of the sky scan for the COSMO experiment. Left: the COSMO instrument with the external spinning wedged flat mirror. The arrows identifies the spin axis, while the mirror is sketched in two positions (red and blue) corresponding to maximum and minimum elevation of the beams. Right: Resulting scan of the beam over the celestial sphere. The blue and red spot mark the maximum and minimum elevations explored by the beam.

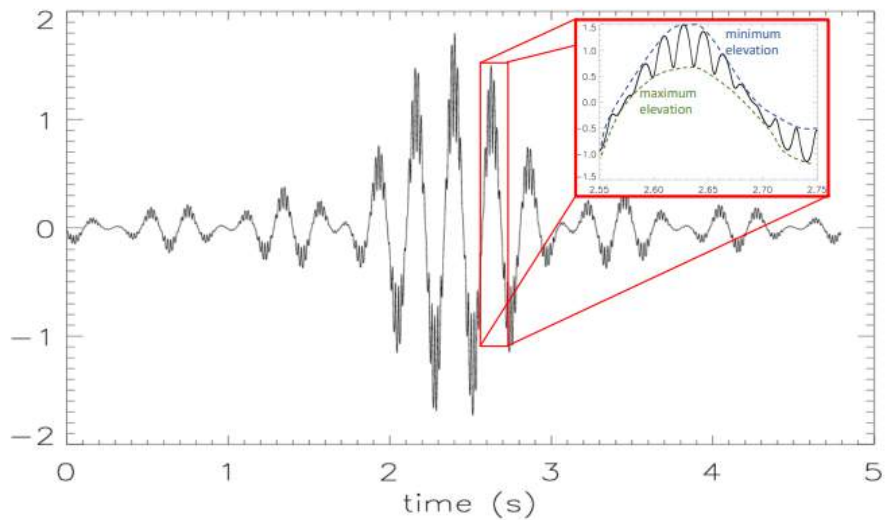


Figure 2.2: Example of expected interferogram obtained while the flat wedged mirror is spinning. The zoomed inset shows how the interferograms, corresponding to the maximum and minimum elevations, can be obtained by properly resampling the measured interferogram.

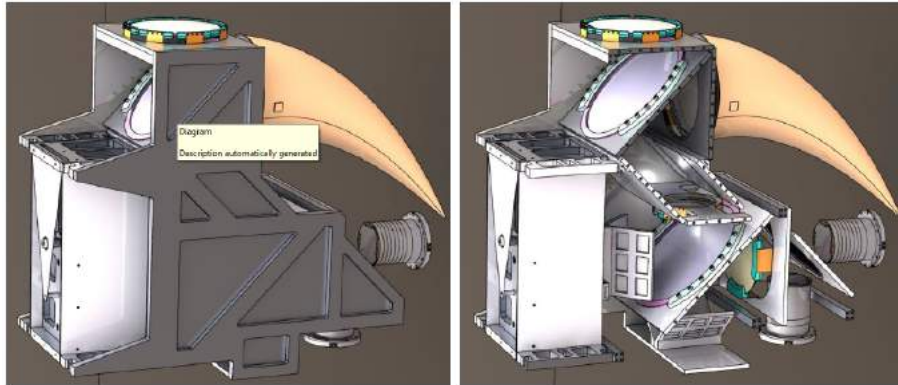


Figure 2.3: 3d rendering of the COSMO's FTS with an insight of the inner vessel housing the optical elements and the blackbody.

## 2.1 Subsystem

### 2.1.1 The Shelter

COSMO's spectrometer will be installed in Concordia Station, on the Antarctic plateau, and will be operational during the Antarctic winter. We designed a specific shelter to accommodate the experiment, seen in fig. 2.4 with a thermally insulated section to protect the most sensitive electronics of the experiment from extremely low temperatures, and a section with a remotely operated roof to accommodate the receiver. The shelter will be mounted on a stilt house to avoid problems with snow drifting and accumulation, a typical difficulty for this kind of equipment in Antarctica.

### 2.1.2 The Cryogenic System

The spectrometer must be operated at cryogenic temperatures, and given the size of the optics and cryogenic reference, a large cold volume is required. The Cryostat is operated by two pulse tube refrigerators, model SRP-082B2S-F70H from Sumitomo Heavy Industries. The Cryostat design is similar to the model used for the QUBIC experiment[27] (see fig. 2.5, a cylindrical shell 1.8 m high and 1.6 m in diameter, which opens to the sky with a 45 cm diameter window made of ultra high molecular weight polyethylene, transparent to the microwave radiation that the experiment seeks to measure (around 150 GHz and 220

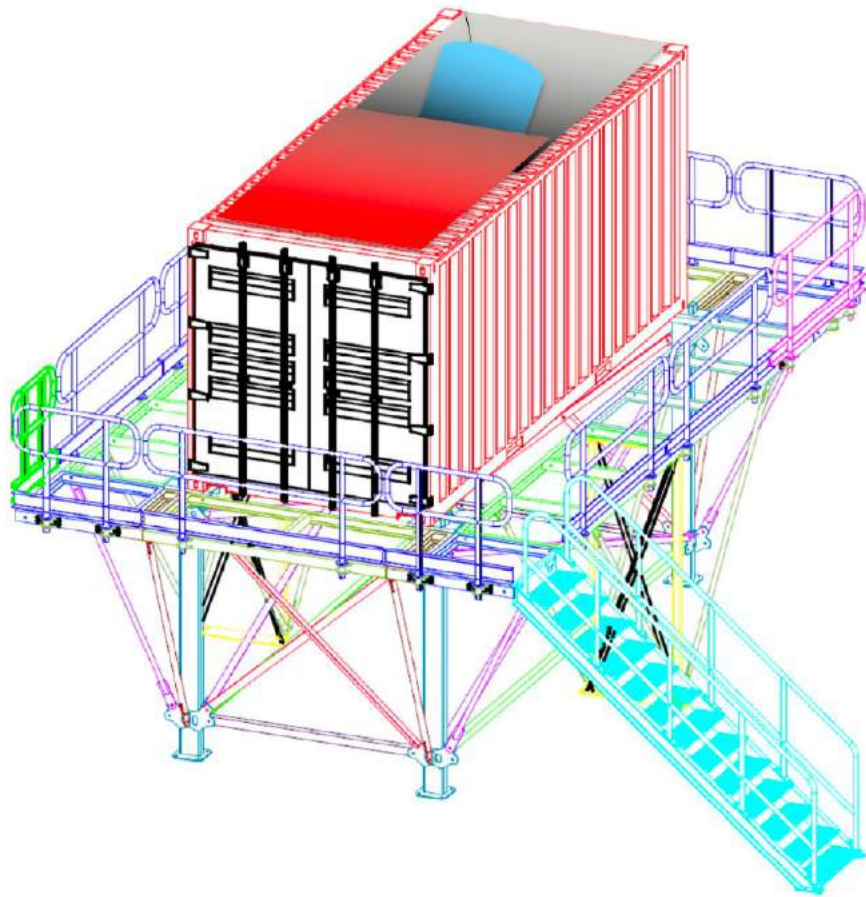


Figure 2.4: 3d rendering of the COSMO's stilt house and shelter

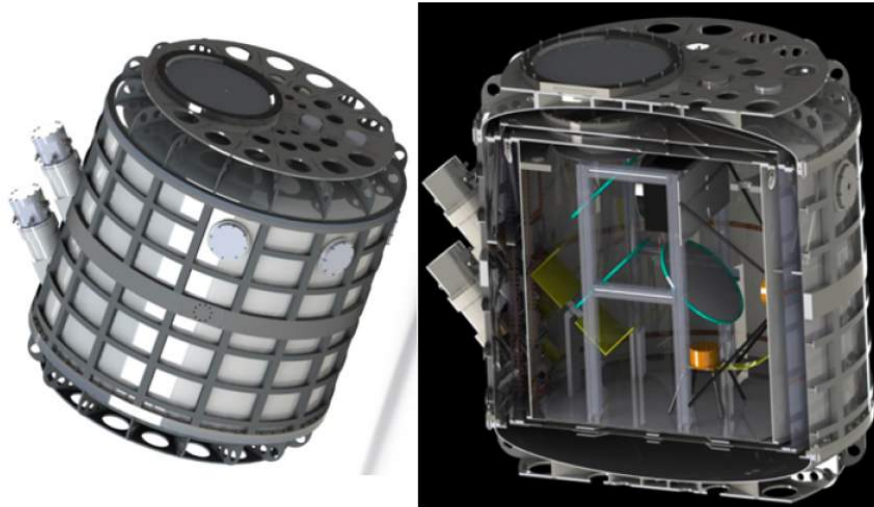


Figure 2.5: 3d rendering of the COSMO cryogenic system

GHz)

### 2.1.3 Sky Scanner

A fundamental subsystem for the functioning of the COSMO experiment is the sky scanner, i.e. a flat, spinning wedge mirror, used to maneuver the telescope beam in the sky along a circle with a diameter of 20 degrees as seen in fig. 2.6. This circle can move thanks to an azimuth-elevation control system. The scan must take place very fast, up to 2500 rpm, in order to measure the atmospheric emission, subtract it in real-time and eliminate the  $1/f$  noise of the atmospheric emission. A lightweighted 6061Al mirror was designed and optimized to minimize mirror inertia. A careful study of the off-axis moments of inertial and their minimization was performed to choose the motor and shaft suitable for these specifications.

### 2.1.4 The Forebaffle

One of the major problems during these measurements is the rejection of ground radiation. A custom forebaffle was designed as a first defense against ground spillover. This forebaffle moves with the receiver and is complemented by a much larger fixed ground shield. The entire internal surface will be covered with microwave absorbing materia. The shield

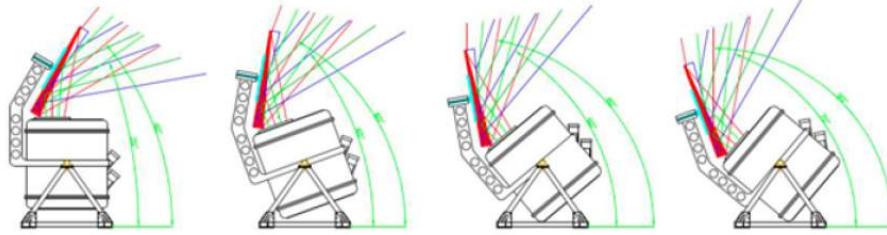


Figure 2.6: The strategy for the sky scanner of COSMO, using the azimuth-elevation control system

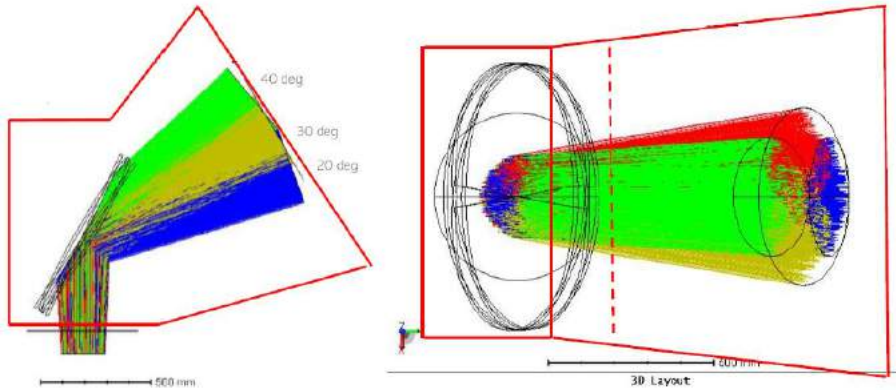


Figure 2.7: The design of the forebaffle with respect to the scanning beam to envelope

has been shaped so as not to modulate the spillover from the surface by the rotations of the wedge mirror. Heaters and temperature sensors allow to evaluate the spillover contribution and measure the signal with custom calibrations campaigns. The forebaffle (fig. 2.7 and fig. 2.8) has been sized to accommodate the wedge mirror angles, which are up to 10 degrees wide, and has been oversized to minimize spillover.

## 2.1.5 The Telescope and FTS

The optical system is composed (see fig. 2.9) by a refractor telescope, a Fourier transform differential spectrometer, and 2 arrays of KIDs. All optical elements must be maintained at a temperature of 2.7 K to mitigate the systematic effect due to stray light during measurements of the CMB spectrum. The aperture telescope is 25 cm in diameter, producing a diffraction limited beam at a maximum wavelength (2.4mm) of 0.7 degrees FWHM. The optical system is optimized to produce a near-parallel beam in two delay lines of the spec-

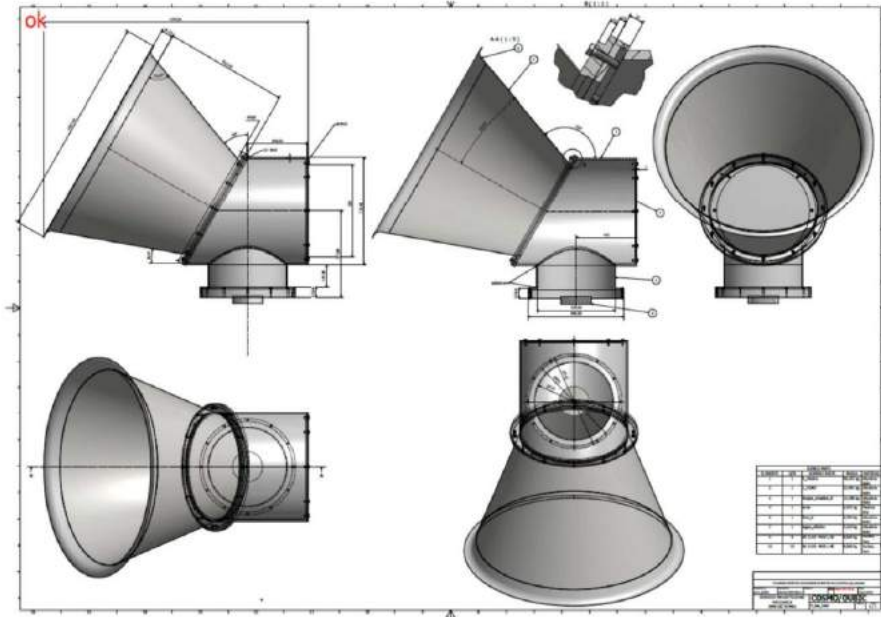


Figure 2.8: Machine shop drawing for the forebaffle assembly of the COSMO experiment

trometer, so that no systematic effects are introduced by scanning the interferogram. The maximum optical path difference introduced by the motion of the movable mirror is + or - 1 cm, corresponding to a coarse spectral resolution of 15 GHz.

### 2.1.6 Reference Blackbody

The reference blackbody[28] is a key element of the experiment. Its accuracy is closely related to the accuracy of the instrument. For this reason, its emissivity must be very close to 1 (within 100 ppb). Following the results of simulations to control the impact on the measurements from the emissivity of the calibrator, a procedure for the construction of the reference black body has been defined, and the molds for the construction of a scaled model have been fabricated and is visible in figure 2.10

### 2.1.7 Delay Line Cryomechanism

The FTS is a MPI (Martin Puplett Interferometer). MPI uses two delay lines terminating in two roof mirrors. The interferogram is obtained by changing the relative length of the

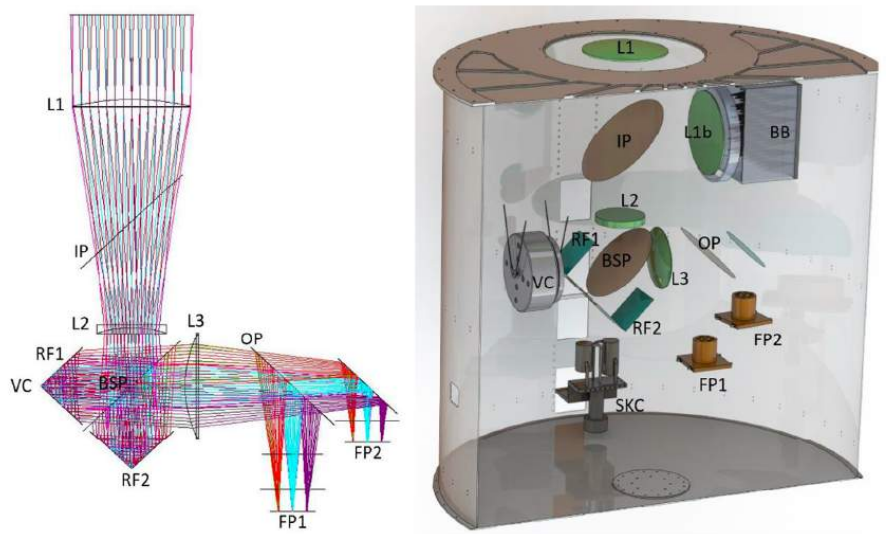


Figure 2.9: Left: ray tracing of COSMO. Right: position of the component inside the cryostat of COSMO. L1-2-3 are the optics, BSP is the beam splitter, RF1-2 the roof mirror and FP1-FP2 the focal planes.

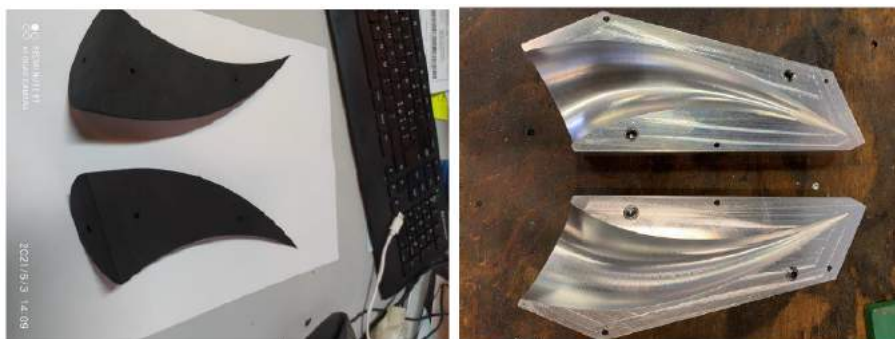


Figure 2.10: Left: inner mold for the reference blackbody (scaled model). Right: outer mold for the reference blackbody

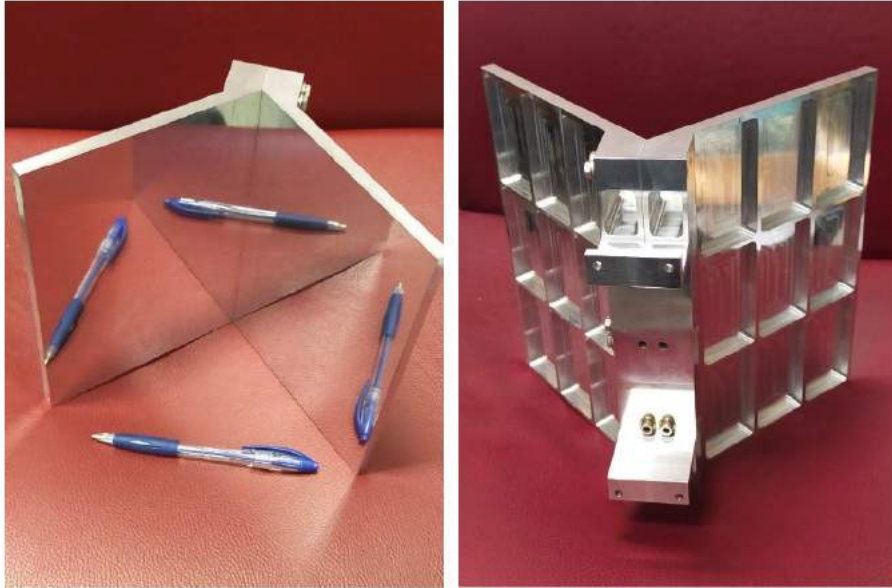


Figure 2.11: Roof-mirror for COSMO

delay lines. This is achieved with the linear movement of one of the two mirrors (fig. 2.11, the active element is a large voice coil. It's a resonant oscillator, based on two planar harmonic steel flexure blades supporting the moving coil and the roof-mirror, with a total excursion of  $\pm 25$  mm, corresponding to a resolution of 6 GHz for symmetric interferograms. Since we operate at cryogenic temperatures, great care was taken to minimize the friction produced by the movement of the roof mirror.

### 2.1.8 The Multimode Feed Arrays

The radiation is coupled to the detectors via two arrays, each of 9 smooth-walled feed-horns operating between 120-180 GHz and 210-300 GHz, respectively (fig. 2.12. Multimoded Feed-horns are a great way to provide greater throughput and higher signal-to-noise level than traditional single-mode receivers, thereby increasing instrument sensitivity without extending the focal plane.

The required specifications are:

- 2x9 Pixels per array, one operates in the 120-180 GHz band (for the low frequency channel), one operates in the 210-300 GHz band (for the high frequency channel)

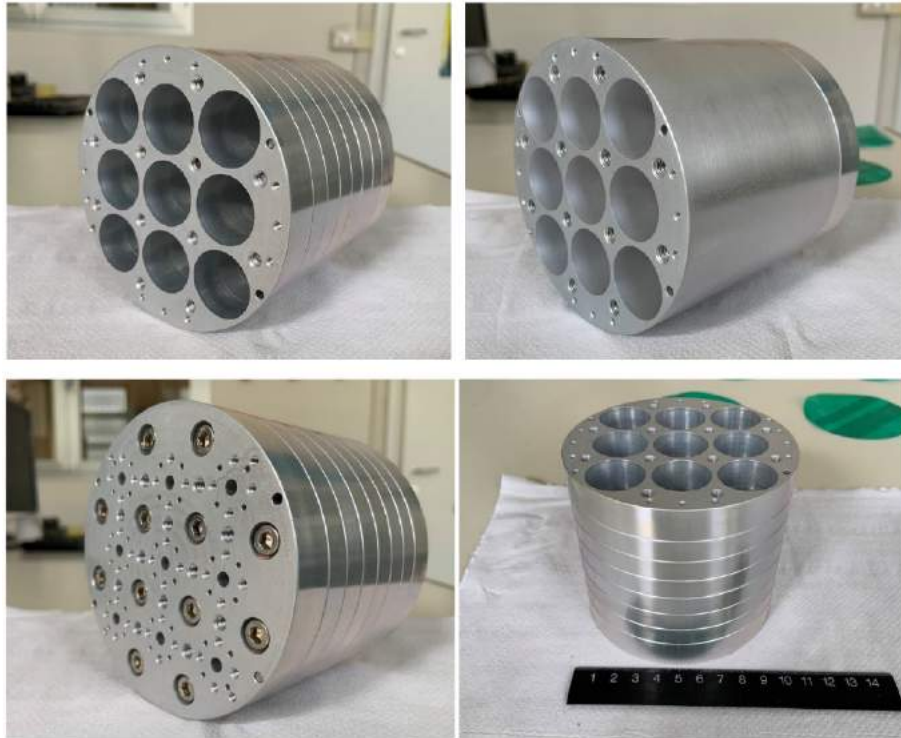


Figure 2.12: Top left and bottom: Feedhorns assemblies for the low frequency array. Top right: Feedhorns assemblies for the high frequency array

- Maximum input aperture of 24 mm, and minimum distance between horns of 26 mm.
- Illumination f/#: f/5
- Coupling to wafer through a circular wave guide of 4.5 mm (low frequency) or 4 mm (high frequency) and a flare
- Total length of feedhorns + waveguide + flare: less than 200 mm.

The low frequency channel consists of Winston Cone Antennas, while the high frequency channel consists of an array of linear profile antennas. It is a trade-off between the multimode requirement for the waveguide and the mechanical constraints of the antenna aperture and the optimization of the antenna directivity within the COSMO cryostat window aperture. These arrays are obtained by superimposing metal plates aligned through dowel-pins and tightening them with screws. The low-frequency array consists of 7 plates and a circular waveguide floor, while the high-frequency array is one piece with a separate circular waveguide floor. Both are in ergal (Al7075) and will be tightened with ergal screws, in order to be compliant with the rest of the focal plane and to avoid differential thermal contractions during the cryostat cooling phase.

### 3. KIDS

The need for rapid data sampling due to the rotating mirror leads to numerous constraints on the choice of detectors. The Kinetic Inductance Detectors were chosen because of their speed of response and the possibility of creating a custom electronic readout based on COTS (Commercial Off-The-Shelf).

The design of Kinetic Inductance Detectors (KIDs) is based on the know-how developed from the successfully tested payload of the OLIMPO experiment (fig. 3.7). The KIDs are made with a thin layer of superconductive aluminum over a high-resistivity silicon substrate. The thickness of the substrate defines a Fabry-Perot cavity for the incident radiation and its value is particularly important to maximize the coupling efficiency of the radiation to be detected. A thickness of the silicon substrate of 150  $\mu\text{m}$  and 85  $\mu\text{m}$  respectively at the two arrays was calculated, considering a  $\lambda/4$  deep cavity. Thicknesses lower than 100  $\mu\text{m}$  are not normally available for 4" silicon wafers as they cannot guarantee a mechanical resistance. We are studying strategies to reduce wafer thickness only at the resonance sites of the KIDs, keeping the rest of the wafer at its native thickness of 260  $\mu\text{m}$ . But let's see in detail what KIDs are, their properties and their use.

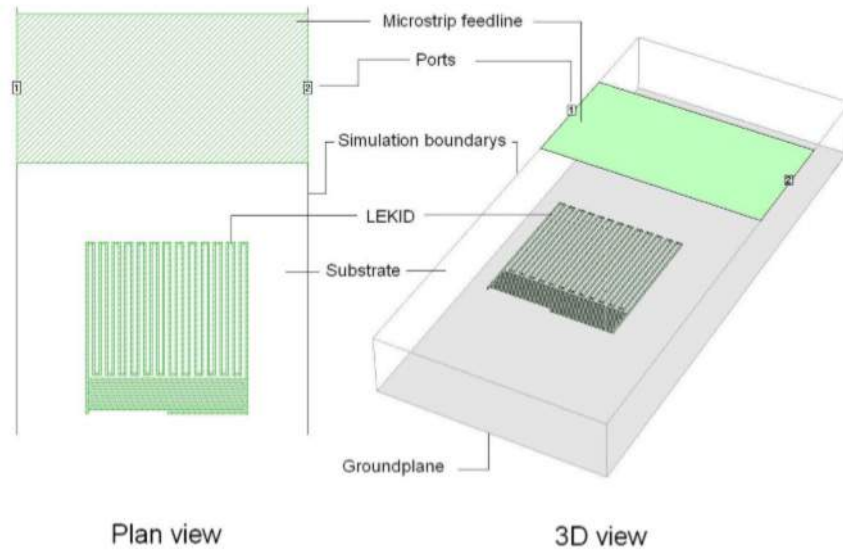


Figure 3.1: Representative geometry of a Lumped Element Kinetic Inductance Detectors, on the left a plan view with the substrate thickness making up the third dimension.

### 3.1 Superconductivity

Superconductivity was discovered in 1911 by H. Kamerlingh Onnes, who noted that a current induced in mercury at the temperature of liquid helium showed no decay over time.[29] To understand this phenomenon it is essential to start from the electrodynamics of superconductors. As the name suggests, a superconductor at a temperature below the critical temperature  $T_c$  characteristic of the specific material exhibits a resistance of  $0\Omega$  to a DC current. This current is carried by pairs of electrons, known as Cooper pairs (see fig. 3.2, bound together by the electron-phonon interaction[30] as seen in figure 3.2. An intuitive explanation of this phenomenon is given by the BCS theory (Barden, Cooper and Schriffer)[31][32], assuming that when an electron moves in the ion lattice it distorts the lattice itself.

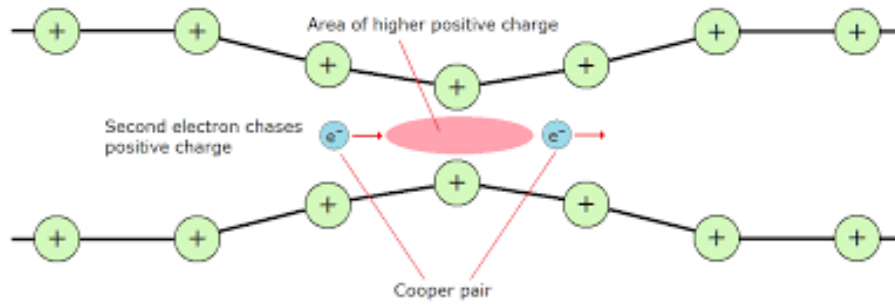


Figure 3.2: Cooper Pair; the first electron (right) moves in the ion lattice distorting it and the second chases the positive charge left by the distortion.

If the temperature is low enough and the ions do not immediately return to their original position, after its passage there is a slight excess of positive charge which tends to attract another electron, which then moves bound to the first. The energy of this bond at  $T=0$  is equal to:

$$2\Delta \approx 3.5k_bT_c \quad (3.1)$$

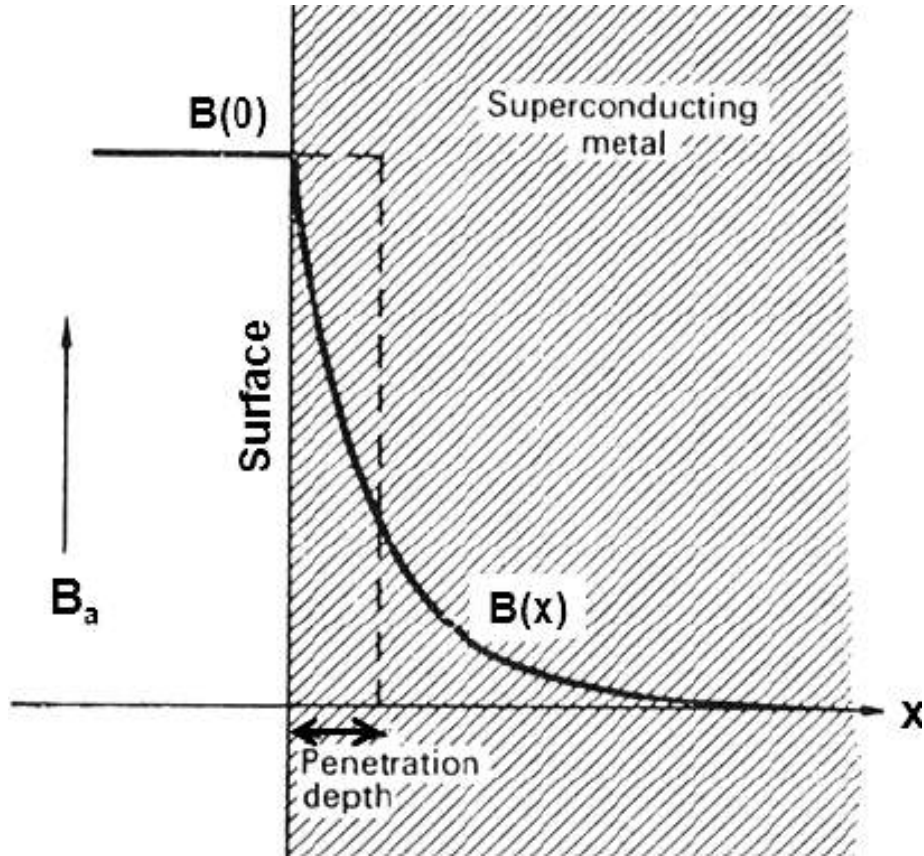


Figure 3.3: London Penetration in a superconducting material: the magnetic field within the material is quickly expelled.

The energy gap of a superconductor  $\Delta$  varies little as the temperature varies below  $T_c$ . Since Cooper pairs have an integer spin, they behave like bosons, conducting the current without dissipating energy. As a consequence, peculiar properties occur, such as the complete expulsion of the magnetic field inside the material (fig. 3.3, explained by H. London[33]. The basic idea is to apply the classical equations of motion to Cooper pairs. Since there are no friction forces, we have:

$$2m_e \frac{d\vec{v}}{dt} = 2e\vec{E} \quad (3.2)$$

With  $m_e$  the effective electron mass.

$$\vec{J} = 2n_{cp}e\vec{v} \quad (3.3)$$

And then:

$$\frac{d\vec{J}}{dt} = 2n_{cp}e\frac{d\vec{v}}{dt} = \frac{n_s e^2}{m_e}\vec{E} \quad (3.4)$$

Where  $n_{cp}$  is the Cooper pair density and  $n_s = 2n_{cp}$  is the bonded electron density. Thus, using Maxwell's equations it can be shown that:

$$\nabla^2 \vec{H} = \frac{1}{\lambda_L^2} \vec{H} \quad (3.5)$$

where:

$$\lambda_L = \sqrt{\frac{m}{\mu_0 n_s e^2}} \quad (3.6)$$

is the London penetration length. We see that, assuming a magnetic field parallel to the surface of the superconductor and denoting with  $x$  the depth inside it, the field decreases as:

$$\vec{H}(x) = \vec{H}(0)e^{-\frac{x}{\lambda_L}} \quad (3.7)$$

Thus each field is shielded exponentially, this effect is known as the Meissner effect.[34]

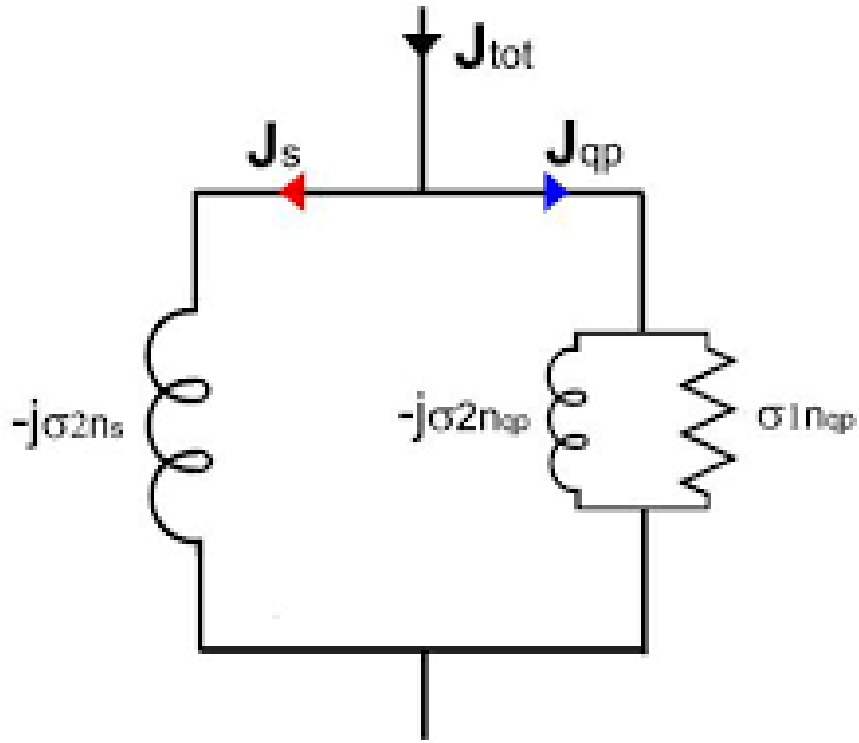


Figure 3.4: Two-fluid model equivalent, we assume two types of carriers, on the left the Cooper pair with dissipation for the alternating current and on the right side the quasiparticles, which behave like classical electrons

In 1934 Gorter and Casimir[35], to explain the electrodynamics in superconductors, described a two-fluid model (fig. 3.4) since the conduction of current without losses occurs only in the case of direct current, while in alternating current a small resistance is created which determines the dissipation of energy. This phenomenon is therefore described assuming that below the critical temperature  $T_c$  there are two types of carriers: a part of electrons, called quasiparticles, equal to those which in normal conditions collide against the lattice generating resistance and a part of electrons in the superconducting state bind in Cooper pairs. The population density of the two types of electrons is described by the empirical law[35]

$$\frac{n_{cp}}{n_{tot}} = 1 - \left(\frac{T}{T_c}\right)^4 \quad (3.8)$$

Neglecting the contribution of the imaginary part of the quasiparticles, we can write the conductivity as:

$$\sigma = \sigma_{qp} - j\sigma_{cp} \quad (3.9)$$

Where  $\sigma_{qp}$  is associated with the quasiparticle density  $n_{qp}$  while  $\sigma_{cp}$  is associated with the Cooper pair density  $n_{cp}$

The variation of density with temperature means that the London penetration length also varies with temperature, according to the formula:

$$\lambda_L(T) = \lambda_L(0) \left[ 1 - \left( \frac{T}{T_c} \right)^4 \right]^{-\frac{1}{2}} \quad (3.10)$$

The total inductance [36][37] of a superconductor consists of two parts, a kinetic inductance  $L_K$  and a magnetic inductance  $L_m$ . The kinetic inductance is associated with the kinetic energy of the Cooper pairs while the magnetic one is associated with the energy of the magnetic field created by the current  $J_S$ . To calculate the kinetic inductance we need to calculate the kinetic energy, given by:

$$E_k = \frac{1}{2} n_{cp} m v_{cp}^2 \quad (3.11)$$

Writing  $v_{cp}^2$  in terms of current density  $J_S = -n_{cp} e v_{cp}$  leads us to write:

$$E_k = \frac{1}{2} \frac{m}{n_s e^2} J_S^2 = \frac{1}{2} \mu_o \lambda^2 J_s^2 \quad (3.12)$$

Kinetic inductance is usually written as:

$$U_k = \frac{1}{2} L_k I^2 = \frac{1}{2} \mu_o \lambda^2 \int_S J_s^2 ds \quad (3.13)$$

With  $U_k$  the total kinetic energy per unit length. Two cases can be distinguished, both with a superconducting film of length  $W$  much greater than the thickness  $t$ . In the first case  $t \gg \lambda_L$ , while in the second case  $t \ll \lambda_L$  (see fig. 3.5).

In the first case the superconducting section will be given by  $S = 2W\lambda_L$  while in the second case it will be given by  $S = Wt$

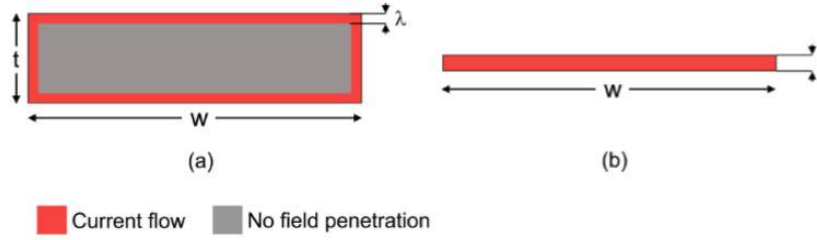


Figure 3.5: Difference from thick and thin film and the current flow on the surface of the material.

In the first case  $J_S = I/2W\lambda$  with  $I$  the total current, and we can calculate  $L_k$

$$\frac{1}{2}L_k I^2 = \frac{\mu_0 I^2}{8W^2 \lambda^2} 2W\lambda \rightarrow L_k = \frac{1}{2} \frac{\mu_0 \lambda}{W} \quad (3.14)$$

For the thin film  $J_S = I/Wt$  and we get:

$$\frac{1}{2}L_k I^2 = \frac{\mu_0 I^2}{8W^2 t^2} Wt \rightarrow L_k = \frac{\mu_0 \lambda^2}{Wt} \quad (3.15)$$

In addition to the kinetic inductance term there is a further magnetic inductance term due to the variation of the magnetic field in the length of penetration at the surface of the superconductor. However, working with thin films and using a specific geometry to break down this term, its contribution is negligible.

### 3.1.1 The impedance of a superconductor

The impedance of a superconductor[37] can be divided into two parts: a complex part which contains the contributions of kinetic inductance and magnetic inductance, and a real part which is equivalent to a resistance. The complex part is given by:

$$X_S = \omega(L_k + L_m) \quad (3.16)$$

While the resistive part can be calculated starting from:

$$RI^2 = Re \int_S \frac{J_S^2}{\sigma_{qp} - j\sigma_{cp}} ds \quad (3.17)$$

Taking the real part and writing the surface integral in terms of the kinetic inductance written above we obtain:

$$R = \frac{\sigma_{qp}}{\sigma_{qp}^2 + \sigma_{cp}^2} \frac{L_k}{\mu_0 \lambda^2} = L_k \omega \frac{\sigma_{qp} \sigma_{cp}}{\sigma_{qp}^2 + \sigma_{cp}^2} \quad (3.18)$$

In the limit  $\sigma_{qp} \ll \sigma_{cp}$  for  $T \ll T_c$ , we can write R as:

$$R = L_k \omega \frac{\sigma_{qp}}{\sigma_{cp}} \quad (3.19)$$

### 3.1.2 Photon detection

Let's try to understand how the impedance changes when energy is absorbed in the superconductor (see fig. 3.6). When a photon arrives with an energy higher than the energy gap ( $h\nu > 2\Delta$ ) it is absorbed inside the superconductor. The photon energy can break one or more Cooper pairs, creating a cascade of interacting quasiparticles. This cascade generates a population of quasiparticles equal to:

$$N_{qp} \approx \eta h\nu / \Delta \quad (3.20)$$

with energies slightly above that of the gap and phonons below the gap in the superconductor.  $\eta \approx 0.57$  is the typical value of the efficiency with which photons are converted into quasiparticles. These quasiparticles exist until they meet and emit a phonon, recombining into Cooper pairs. The time necessary for this to happen is the average lifetime of the quasiparticle,  $\tau_{qp}$  calculated by Kaplan theory[38] as:

$$\frac{1}{\tau_{qp}} = \frac{\sqrt{\pi}}{\tau_0} \left( \frac{2\Delta}{k_B T_C} \right)^{\frac{5}{2}} \left( \frac{T}{T_C} \right)^{\frac{1}{2}} e^{\frac{-\Delta}{k_B T_C}} \quad (3.21)$$

During this time, the quasiparticles can diffuse over a distance equal to  $l \simeq \sqrt{D\tau_{qp}}$  where  $D$  is the diffusion constant of the material. If the photon energy is too low, or if the photon count is too high to count individual photons, the absorption of a photon beam will increase the quasiparticle density by  $\delta n_{qp} = \eta P \tau_{qp} / \Delta$  with  $P$  the power of the incident photon flux.

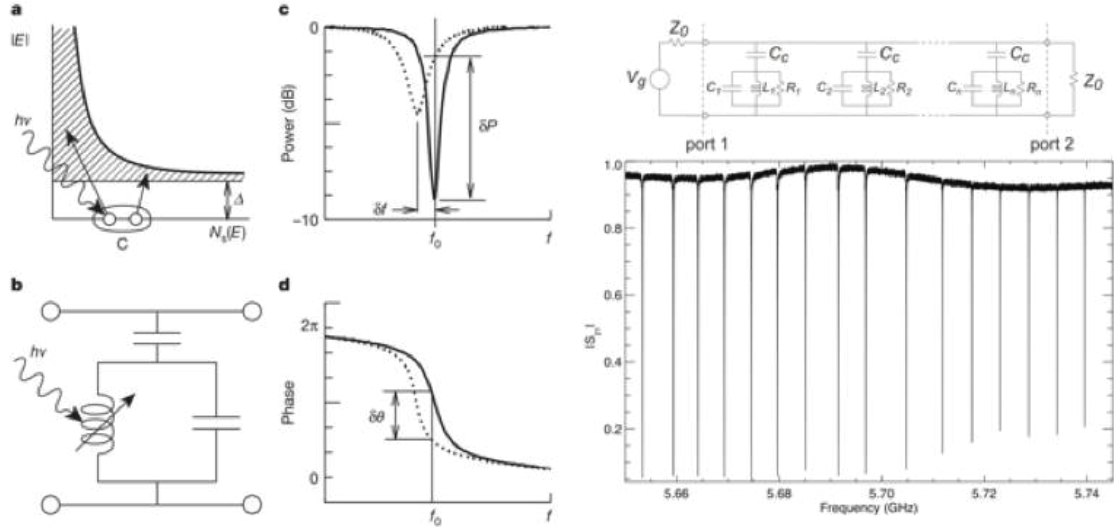


Figure 3.6: Left: working principle of KIDs. A Cooper pair is destroyed by a photon with sufficient energy, modifying the impedance of the circuit and modifying the amplitude and phase of the signal. Right: array of KIDs with different resonance frequencies

An excess of quasiparticles in a superconducting film changes the surface impedance  $Z_s$  similarly to what happens with a temperature rise.  $Z_s$  changes with temperature, so we expect a similar change when the density of quasiparticles is varied. Approximately, we get:

$$\frac{\delta Z_s}{Z_s} \approx \frac{\eta_{qp}}{2N_0\Delta} \quad (3.22)$$

Although the changes in  $Z_s$  may be small, we can obtain a very sensitive measurement using a resonant circuit (fig. 3.6). Changes in  $L_s$  and  $R_s$  change the resonant frequency and width, respectively, change the amplitude and phase of a signal transmitted along the loop. The phase shift times the number of quasiparticles created  $\frac{d\Theta}{dn_{qp}}$  is the detector response as we will see in the chapter 3.2.3.

## 3.2 Lumped Element Kinetic Inductance

A lumped element KID (also called a Lumped Element Kinetic Inductance Detector, LEKID)[24] (fig. 3.7 consists of an inductor and a capacitor connected to form a resonant circuit. By varying the physical and geometrical characteristics of the apparatus, such as the length of the inductor or of the capacitor, it is possible to place several LEKIDs in series on a single transmission line, and this leads to an enormous reduction of the heat load by conduction with respect to a detector with multiple power and reading lines (as in the case of TES, which requires a SQUID in order to achieve multiplexing).

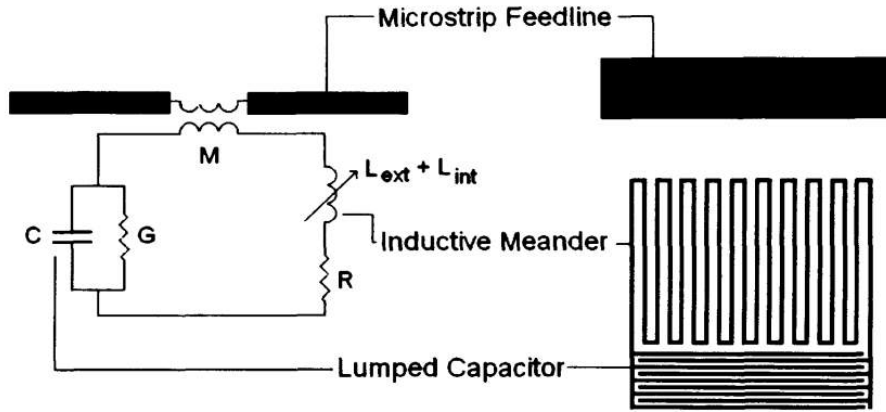


Figure 3.7: Left: The LEKID equivalent circuit. Right: a schematic of a LEKID device.  $M$  is the mutual inductance between the LEKID and the feedline,  $R$  is the resistance of the meander section,  $L_{ext} + L_{int}$  is the total inductance of the meander section,  $C$  is the capacitance and  $G$  is the conductance of the inter-digital capacitor section respectively.

We can assimilate the architecture of a LEKID to that of an RLC resonant circuit and study a resonant frequency and the gain of this circuit. The resonance frequency is given by:

$$\omega_0 = \frac{1}{\sqrt{(L + L_k)C}} \quad (3.23)$$

$L$  and  $C$  depend on the chosen geometry, so we can modify it and place several LEKIDs on the same transmission line. Each of these will be characterized by its own resonant

frequency. The parameter  $L_k$  depends on the quasiparticle concentration (as discussed in the previous chapter) and its variation contains information on the received photon flux.

The quality factor  $Q$  is a dimensionless value which expresses the ratio between the resonance frequency and the width at half depth of the resonance itself. From an energy point of view it can be interpreted as the ratio between stored energy and dissipated power.

$$Q = \omega_0 \frac{E_i}{P_d} \quad (3.24)$$

The greater the  $Q$  factor, the greater the resolution of the detector, since as  $Q$  increases, the depth increases and the bandwidth decreases, thus narrowing the range of frequencies observable around the characteristic resonance frequency. We can also redefine the quality factor as:

$$Q = \frac{\omega_0}{\Delta\omega} \quad (3.25)$$

with  $\omega_0$  the resonant frequency and with  $\Delta\omega$  the bandwidth.

### 3.2.1 Scattering parameters

Microwave circuits are typically characterized by the scattering parameters  $S$ . They return the fraction of potential between the gates in an  $n$ -port system. In our case we have only one input and one output, so it reduces to a two-port system with 4 scattering parameters,  $S_{11}, S_{12}, S_{21}, S_{22}$ . Denoting with  $V_1^+$  and  $V_2^+$  the incident signal respectively from the first and second port, and with  $V_1^-$  and  $V_2^-$  the reflected signal, we have: (fig. 3.8

$$\begin{aligned}
 S_{11} &= \frac{V_1^-}{V_1^+} \\
 S_{12} &= \frac{V_1^-}{V_2^+} \\
 S_{21} &= \frac{V_2^-}{V_1^+} \\
 S_{22} &= \frac{V_2^-}{V_2^+}
 \end{aligned}
 \tag{3.26}$$

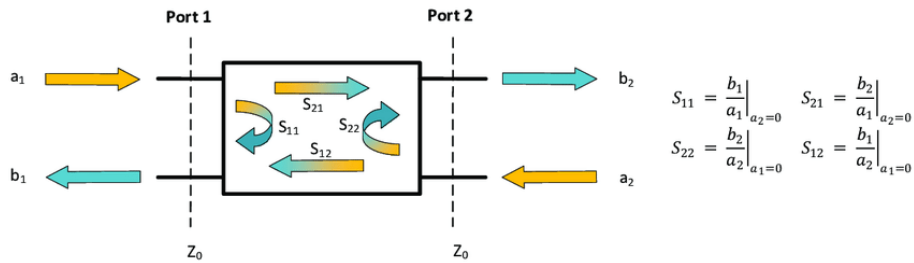


Figure 3.8: Scattering Parameter

The first subscript indicates the port where the signal is received, the second the port transmitting the signal.  $S_{21}$  therefore represents the signal injected into port 1 and outgoing from port 2. The theoretical calculation of the coefficients  $S$  for a circuit is possible through the construction of the ABCD formalism matrix: these letters represent different coefficients calculated on the basis of the circuit architecture (fig. 3.9).

| Circuit | ABCD Parameters    |                    |
|---------|--------------------|--------------------|
|         | $A = 1$<br>$C = 0$ | $B = Z$<br>$D = 1$ |
|         | $A = 1$<br>$C = Y$ | $B = 0$<br>$D = 1$ |

Figure 3.9: The ABCD matrix formalism.

The ABCD matrix is calculated knowing the values of the potential and of the current

measured on the two ports:

$$\begin{bmatrix} V_1 \\ I_1 \end{bmatrix} = \begin{bmatrix} A & B \\ C & D \end{bmatrix} \begin{bmatrix} V_2 \\ -I_2 \end{bmatrix} \quad (3.27)$$

The minus sign of  $I_2$  is needed because conventionally the positive direction of the current is taken towards the inside of the door. From (3.27) we get:

$$V_1 = AV_2 - BI_2 \quad (3.28)$$

$$I_1 = CV_2 - DI_2$$

The case of LEKIDs is a series of impedances, so:

$$I_1 = -I_2 \quad (3.29)$$

$$V_1 - V_2 = Z_{tot}I_1$$

The matrix ABCD is therefore given by:

$$\begin{bmatrix} 1 & Z_{tot} \\ 0 & 1 \end{bmatrix} \quad (3.30)$$

Conversion tables computed by Frickey[39] are used to convert from the ABCD matrix to the scattering parameters S. The parameter  $S_{21}$  is given by:

$$S_{21} = \frac{2}{A + \frac{B}{Z_0} + CZ_0 + D} \quad (3.31)$$

With  $Z_0$  which is the characteristic impedance of the circuit.

### 3.2.2 S21 gain parameter

We can calculate the parameter  $S_{21}$  by describing it as a complex series of impedances.

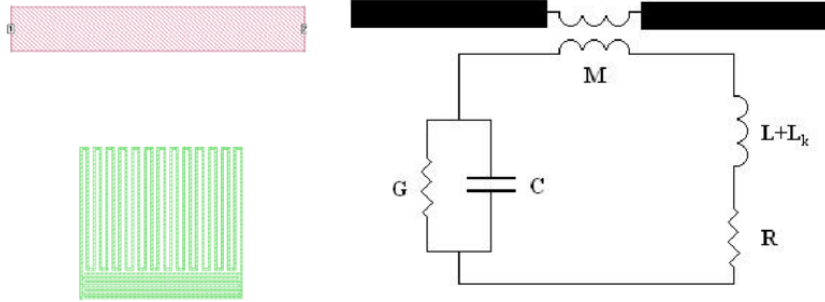


Figure 3.10: Schematic of a LEKID

Defining:

$$V = j\omega M I_{res} \quad (3.32)$$

the potential difference on the power line (with  $M$  inductance of the line and  $I_{res}$  the current flowing in the resonant section of the circuit) and with

$$Z_{res} = j\omega L + \frac{1}{j\omega C} + R \quad (3.33)$$

the impedance of the resonant section, we can use Kirchhoff's first law in the circuit of fig. 3.10 to write:

$$j\omega M I_l + I_{res} Z_{res} = 0 \quad (3.34)$$

from which the values of  $I_{res}$  are obtained:

$$I_{res} = -\frac{j\omega M I_l}{Z_{res}} \quad (3.35)$$

And so

$$V = -\frac{\omega^2 M^2 I_l}{Z_{res}} \quad (3.36)$$

$$Z_{eff} = \frac{V}{I_l} = \frac{\omega^2 M^2}{Z_{res}} \quad (3.37)$$

Eventually, the  $Z_{eff}$  of the circuit can be calculated:

$$Z_{eff} = \frac{V_l}{I_{res}} = \frac{\omega^2 M^2}{Z_{res}} \quad (3.38)$$

Once this parameter has been calculated, it is therefore possible to obtain the value of  $S_{21}$

$$S_{21} = \frac{2}{2 + \frac{Z_{eff}}{Z_0}} = \frac{2}{2 + \frac{\omega^2 M^2}{Z_{res} Z_0}} \quad (3.39)$$

Considering  $Z_{res} = j\omega L + \frac{1}{j\omega C} + R$  the value  $\frac{1}{j\omega C}$  remains constant, while both  $L$  and  $R$  increase as the kinetic inductance (which depends on the population of quasiparticles) increases. Since the resonant frequency (which indicates the point where the transmitted signal is most attenuated) is  $\omega_0 = \frac{1}{\sqrt{LC}}$  the resonant frequency increases by  $L$  decreases. Increasing  $R$ , on the other hand, the peak widens, since the  $Q$  factor depends on the resistance according to the relationship:

$$Q_i = \frac{1}{\omega_0 RC} = \frac{\sqrt{L}}{\sqrt{CR}} = \frac{\sqrt{L+L_k}}{\sqrt{CR}} \propto \frac{\sqrt{L_k}}{R} \quad (3.40)$$

As we have seen previously, we can write  $R = L_k \omega \frac{\sigma_1}{\sigma_2}$  and therefore  $Q$  decreases as the population of quasiparticles increases, and the resonance peak gets wider.

We actually need a power supply to send the resonance monitor signal, and the impedance of the power supply lowers the total  $Q$  which can be calculated from the law of mutual inductance:

$$Q_s = \frac{LZ_0}{\omega_0 M^2} \quad (3.41)$$

Therefore:

$$\frac{1}{Q} = \frac{1}{Q_s} + \frac{1}{Q_i} \quad (3.42)$$

### 3.2.3 Parameter S<sub>21</sub>, real and imaginary

The response of a LEKID to the energy released by the photons are encoded in the variation of the phase and amplitude of the test signal transmitted through the feeding line[40]. It is convenient to write  $S_{21}$  in terms of real and imaginary parts, since amplitude and phase can be calculated using the matrix:

$$\begin{bmatrix} 1 & Z_{tot} \\ 0 & 1 \end{bmatrix} \quad (3.43)$$

The signals at the LEKIDs output already comes in the form of the real and imaginary parts, as we will see later. Being able to link these data to the physical characteristics of the resonator allows us to calculate the flux of incident photons.

To this aim it is better to rewrite  $Z_{res}$  considering that  $C$  and  $L$  are linked together through the resonance frequency  $\omega_0 = \frac{1}{\sqrt{LC}}$  where  $L$  is the total inductance:

$$Z_{res} = j\omega L + \frac{1}{j\omega C} + R = R + j\omega L \left( \frac{\omega^2 - \omega_0^2}{\omega^2} \right) \quad (3.44)$$

For small variations in frequency from the resonance value, we can write that:

$$\omega^2 - \omega_0^2 = (\omega - \omega_0)(\omega + \omega_0) = \Delta\omega(2\omega - \Delta\omega) \approx 2\omega\Delta\omega \quad (3.45)$$

$$Z_{res} \approx R + j2L\Delta\omega \approx R + j\frac{2RQ_i\Delta\omega}{\omega_0} \quad (3.46)$$

It is convenient to define a parameter, called coupling coefficient;

$$g = \frac{\omega_0^2 M^2}{2Z_0 R} = \frac{\omega_0 M^2}{2Z_0 L} Q_i \quad (3.47)$$

to redefine the quality factor in terms of  $g$ :

$$\frac{1}{Q} = \frac{1}{Q_S} + \frac{1}{Q_i} = \frac{1}{Q_i} + \frac{\omega_0 M^2}{LZ_0} = \frac{1}{Q_i} + \frac{g}{2Q_i} = \frac{g+2}{2Q_i} \quad (3.48)$$

With this new information we can finally rewrite  $S_{21}$  (and defining  $\Delta x = \frac{\Delta\omega}{\omega_0}$ )

$$S_{21} = \frac{2(g+2) + 16Q_i^2\Delta x^2}{(g+2)^2 + 16Q_i^2\Delta x^2} + j(4Q_i\Delta x) \frac{g+2}{(g+2)^2 + 16Q_i^2\Delta x^2} \quad (3.49)$$

Finally getting the real part and the imaginary part of  $S_{21}$

Far from the resonance frequency,  $\Delta x$  assumes high values and therefore it follows from the equation 3.49 that  $S_{21} \approx 1$ , i.e. that far from the resonance frequency the transmission is made up of only real part and has unit value. All the signal is transmitted without undergoing phase or amplitude variations because the KID does not absorb frequencies far from its resonant own.

The minimum at the resonance peak is obtained  $\Delta x = 0$  with:

$$S_{21min} = \frac{2}{g+2} \quad (3.50)$$

completely real again. Around the resonant frequency there are rotations on the complex plane, which draw a circumference of fixed amplitude centered in  $(\frac{1}{2}(1 + S_{21min}); 0)$ .  $S_{21min}$  measures the distance from the point (0,0), the ideal condition of a resonant circuit. It depends on the magnitude of  $g$ , which in turn depends inversely on the resistance. When photons deposit energy on the LEKID, the resistance value increases, the  $g$  factor decreases and  $S_{21min}$  increases accordingly. This leads to a change in the center of rotation, which moves to the right.

Ignoring the terms in  $\Delta x^2$  we can compute modulus and phase, obtaining:

$$|S_{21}| = \frac{1}{g+2} \sqrt{4 + (4Q_i\Delta x)^2} \quad (3.51)$$

$$\angle S_{21} = \frac{Q}{2S_{21min}} \frac{\Delta\omega}{\omega_0}$$

thus linking the variation of amplitude and phase to the variation of the resonant frequency.

Calling  $\Theta$  the angle of variation, for infinitesimal variations we obtain:

$$\frac{d\Theta}{d\omega_0} = -\frac{Q}{2S_{21min}} \frac{1}{\omega_0} \quad (3.52)$$

The minus comes from the fact that the resonant frequency shift will be at lower frequencies, and the phase angle will increase.

### 3.2.4 Increase sensitivity

Since we have a very convenient relationship to link the phase with the frequency variation, we want to link the phase variation with the variation of the quasiparticle population:

$$\frac{\partial \Theta}{\partial n_{qp}} = \frac{\partial \Theta}{\partial \omega_0} \frac{\partial \omega_0}{\partial L_{tot}} \frac{\partial L_{tot}}{\partial \sigma_2} \frac{\partial \sigma_2}{\partial T} \frac{\partial T}{\partial n_{qp}} \quad (3.53)$$

that for a small variation of the population of quasiparticles the phase undergoes the greatest possible variation, each of the single terms of the previous equation will have to be maximized.

The term  $\frac{\partial \Theta}{\partial \omega_0}$  represents the change of phase with the shift of the resonant frequency. From the equations  $\frac{d\Theta}{d\omega_0} = -\frac{Q}{2S_{21min}} \frac{1}{\omega_0}$  we can obtain that it is proportional to  $\frac{1}{M^2}$ , therefore to maximize this value we must move the LEKID away from the supply line, reducing the term  $M^2$ .

The term  $\frac{\partial \omega_0}{\partial L_{tot}}$  represents the change of the resonant frequency with the change of inductance.

$$\frac{\partial \omega_0}{\partial L_{tot}} = \frac{\omega_0 \alpha}{L_k} \quad (3.54)$$

$$\alpha = \frac{L_k}{L_{tot}}$$

we must therefore use materials with a strong kinetic inductance component and with very thin superconducting films.

The last three ratios are calculated from the theory of Mattis-Bardeen[41], who have applied corrections to the electromagnetism of superconductors.  $\frac{\partial L_{tot}}{\partial \sigma_2}$  is the variation of inductance as the complex conductivity of the superconductor varies. Since it depends on the thickness  $t$  of the material, thin films must be used. Using  $\gamma = \sigma_2 \omega_0 \mu_0$  it can be shown that:

$$\frac{\partial L_{tot}}{\partial \sigma_2} = \frac{-\mu_0}{8} \sqrt{2} \left[ \frac{2\sqrt{\gamma} \coth\left(\frac{t}{2}\sqrt{\gamma}\right) - t\gamma + \gamma \coth\left(\frac{t}{2}\sqrt{\gamma}\right)^2}{\sqrt{\frac{-\mu_0}{\sigma_2 \omega} \sigma_2 \omega \gamma}} \right] \quad (3.55)$$

The term  $\frac{\partial \sigma_2}{\partial T}$  represents the variation of conductivity with temperature. Writing  $\beta = \frac{\hbar \omega}{2k_b T}$  we get:

$$\frac{\partial \sigma_2}{\partial T} = \frac{-\pi \Delta(T) \sigma_m}{\hbar \omega_0 k_b T^2} e^{\frac{2\Delta(0) + \hbar \omega_0}{-2k_b T}} [2\Delta(0) I(\beta)] \quad (3.56)$$

The term  $\frac{\partial T}{\partial n_{qp}}$  finally links the temperature with the population density of quasiparticles. One must therefore work at very low temperatures ( $T \ll T_c$ ) and with small volumes of superconductors

$$n_{qp} = 2N(0) \sqrt{2\pi k_b \Delta(0)} e^{\frac{-\Delta(0)}{k_b T}} \quad (3.57)$$

The final equation is very complicated, but the terms of our interest and which we can act on (and which do not strictly depend on the material) can be simplified:

$$\frac{\partial \Theta}{\partial n_{qp}} \approx \frac{\alpha}{L_k V} \frac{8Q_i}{g} \quad (3.58)$$

In summary, to obtain the highest sensitivity of the detector you must have:

- High  $Q$  factor, to increase phase response
- Small volumes and low temperatures, to obtain a high value of  $\frac{\partial T}{\partial n_{qp}}$
- Thin films, to have a  $\alpha$  factor lift

All these requests agree with the functioning of the MKIDs, which already operate at low temperatures and with high  $Q$  factors. To further increase  $Q$  we can play on the inductance of the  $M$  line, remembering that the two values are inversely proportional:

$$\frac{1}{Q} = \frac{1}{Q_i} + \frac{\omega_0 M^2}{LZ_0} \quad (3.59)$$

As  $M$  decreases, the value of  $Q$  increases. But decreasing  $M$  also increases the value of  $S_{21min}$  which depends on  $M$  through  $g$ , as  $S_{21min} = \frac{2}{g+2}$ .

We must therefore ensure that  $Q_i$  contributes the most to the value of  $Q$ , and not  $Q_s$   $\left(\frac{LZ_0}{\omega_0 M^2}\right)$ .

## 4. Electronic Readout

Once the detectors to be used in the experiment have been chosen, the readout must satisfy a set of requirements like the number of pixels, their sampling rate, the overall energy resolution. Although the parameter that contains the most important information in the case of KIDs is the variation of the resonance frequency of the detectors, if we think to continuously scan the band looking for frequency shift, this approach conflicts with the most important specifications: the sampling rate of the detectors. To give an example we can make a simple consideration: let's imagine running a scan to find the resonance frequencies and use a simple and fast algorithm to find where they are. For a band spanning 100 MHz, even sending a signal of 1000 samples and requiring 100 KHz of  $\Delta\nu$ , neglecting any delay in transmission and reception and no slowdown for the computation of the algorithms necessary for the search and the analysis of the signal, this results in a sampling rate of 100 Hz, definitely below the desired COSMO specifications (tens of KHz).

For this reason, we developed a state machine. The idea is, instead of directly measuring the variation of the resonant frequency, to measure the amplitude and phase of the signals probing the detectors, tracking any possible variation induced by photon interaction. These variations, which we can see in figure 3.6, cause a variation of amplitude and phase of the signal, linked to the number of quasiparticles generated by the photon from the formula  $N_{qp} \approx \eta h\nu/\Delta$

The disadvantage of this technique is that it does not have a direct measurement of the variation of the resonant frequency, but the big advantage is to be able to reach a much faster sampling rate, eliminating a factor of 1000 from the previous calculation, and requesting a single LookUp Table of 1000 values containing the parameters needed to create the comb signal probing the detectors. The different states implement different phases of the detection process: from the search for the resonance frequencies, to the comb coefficient calculation to the free run data acquisition.

## 4.1 Operation of the state machine

A finite state machine is an abstract machine that can be in one and only one of a finite number of state at any given time, and can change from one state to another in response to some inputs or outputs. This change is called transition. A list of states and the inputs that trigger a transition are defined. In our case, we have a 3 state machine (see fig. 4.1). The first state have to transmit a signal along the detector transmission line to scan the entire band in order to find all the resonant frequencies of the detectors. The second state deals with the generation of the signal, a combination of tones, to be transmitted along the detectors. The third state finally transmits, receives and analyzes the signal in free run, till some major change triggers the repetition of the first one.

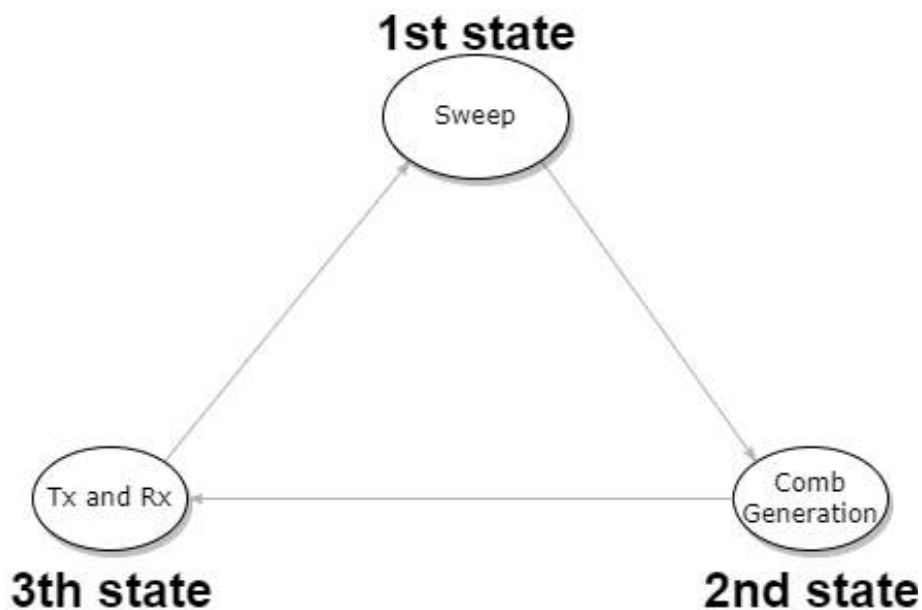


Figure 4.1: The logic of the finite state machine.

### 4.1.1 First State

In the first state we want to find all the resonant frequencies of our detectors. For this reason a chirp is used (fig. 4.2, a signal with frequency that varies over time, according to

the formula:

$$\begin{aligned} f(t) &= f_0 + kt \\ k &= \frac{f_1 - f_0}{T} \end{aligned} \tag{4.1}$$

$f_0$  is the initial frequency,  $f_1$  is the final frequency and  $T$  is the time it takes to go from the initial frequency to the final frequency. This allows us to scan our entire band, obtaining the spectrum in figure 4.3. An algorithm recognizes the resonances and saves their frequencies in an array.

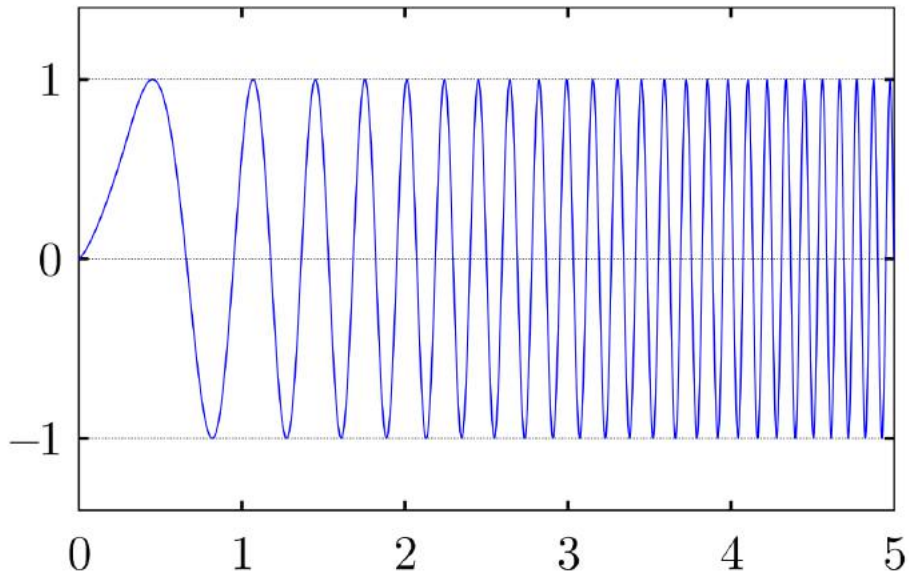


Figure 4.2: Example of a chirp signal

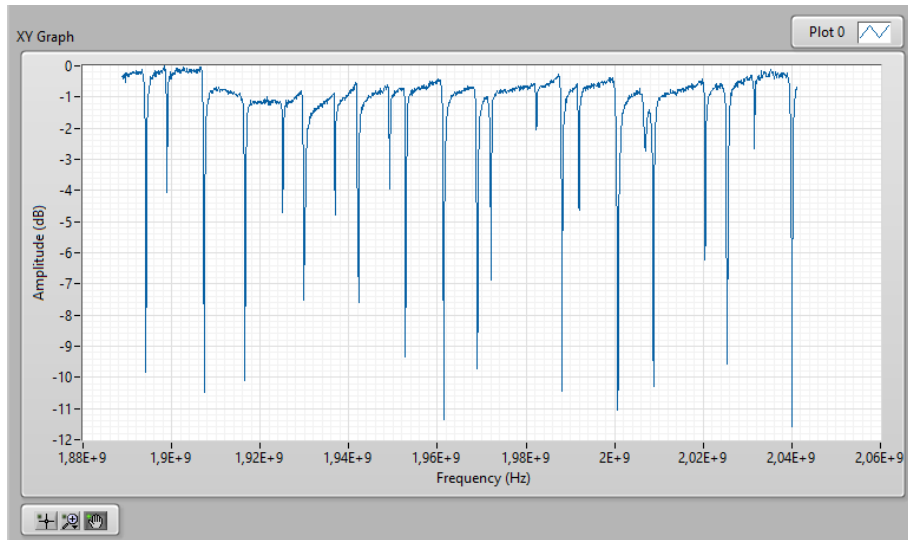


Figure 4.3: The result of the chirp through the KIDs. We can see all the resonances of our array of KIDs

#### 4.1.2 Second State

The second state deals with tones generation. These are created using a CORDIC algorithm[42]: using only additions, subtractions and a LookUp Table of the arctangents and one for a scaling factor, the desired frequency signals can be generated with a resolution of  $\frac{1}{2^{n-1}}$  with N number of addition and subtraction stages. The greater the value of N, the better the accuracy of the tones will be (see fig. 4.4: however, the computational cost and the execution time of the state will also be greater. It is therefore necessary to find a good trade off between resolution and execution time. However, this is not a particularly limiting problem, as this operation must be performed only once at the start of the data acquisition.

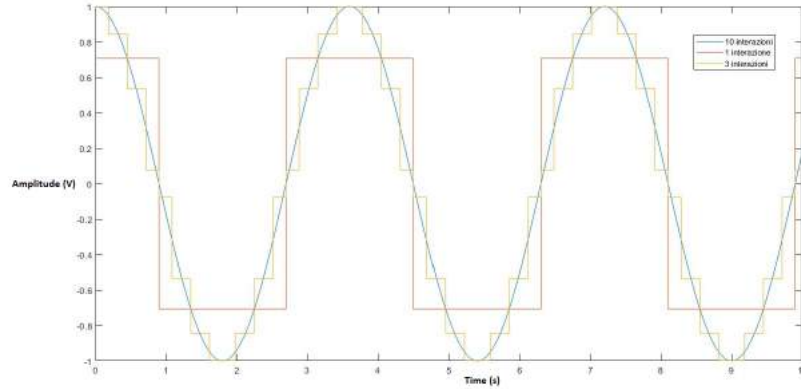


Figure 4.4: Comparison of the result of a generated signal with a different number of iteration.

### 4.1.3 Third State

In the third state of the machine the tones generated on the basis of the look-up table compiled by the second state are transmitted through the detectors and the modified signal is acquired. There are two solutions to read each single tone: the first is to analyze the acquired signal using the Fast Fourier Transform FFT: in this case the frequency comb, made up of the sum of transmitted sinusoids, is analyzed using an FFT algorithm in a process called Channelization[43] (fig. 4.5). The idea is to separate the frequency band into regular intervals and then create much finer intervals that contain a single tone. By filtering the signal using band-pass filter of the frequencies found, the generated tones are separated and can be analyzed one by one.

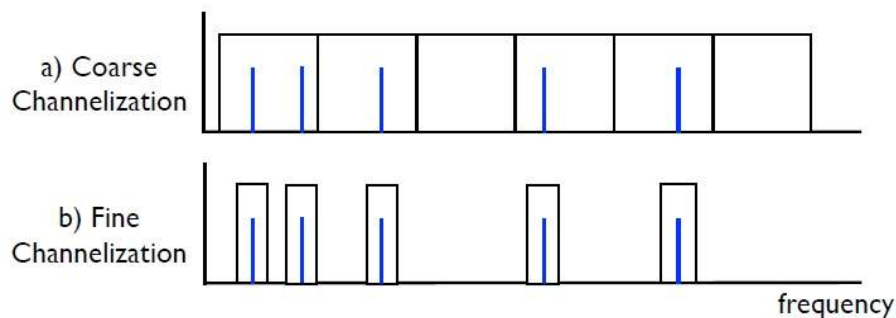


Figure 4.5: Logic of the Channelization process.

The disadvantage of this technique resides in the number of points used. The signal-to-noise ratio (SNR) depends on the length of the FFT[44], because the noise power is distributed across all bins of the FFT. The second solution is called Direct Down Conversion (DDC)[45]. A DDC consists of three subcomponents: a Direct Digital Synthesizer (DDS), a Low Pass Filter (LPF) and a SubSampler (fig. 4.6). It is usually used to bring a signal from the intermediate frequency (IF) to the base band (Base Band). DDS generates a complex sine wave that is mixed with the incoming signal. This generates a baseband signal (plus a high frequency signal) which is filtered through the LPF to eliminate the high frequency signals. Using a number of DDCs equal to the number of tones generated, and using the tones previously transmitted in the LEKIDs as DDS, we can baseband and filter every single signal, without having to use the FFT. This allows to analyze a number  $N$  of tones as if they were  $N$  digital signals continuous in time. When a photon affects a specific pixel, the signal that will be modified will be that of the corresponding mKIDs.

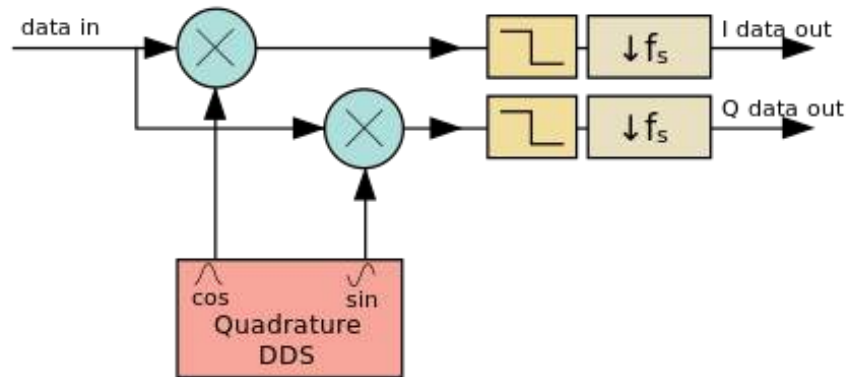


Figure 4.6: Logic block of the Direct Down Conversion

## 4.2 Hardware

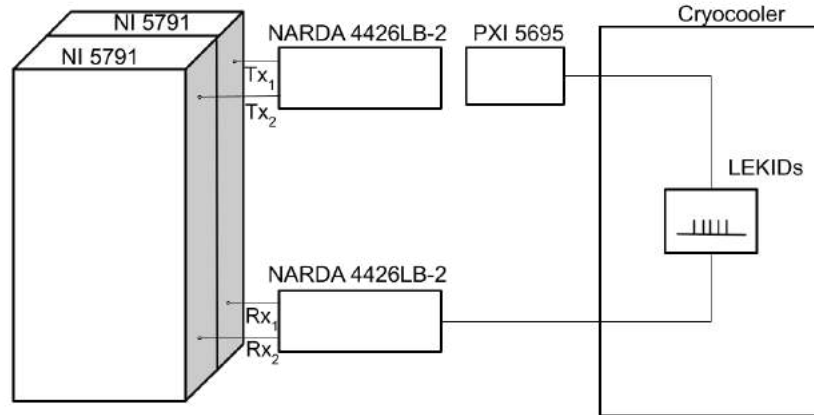


Figure 4.7: Block Diagram of the readout electronic. To cover a wider band, the signal is generated by 2 transceiver, added together by a Wilkinsons power splitter and attenuated by an attenuator before entering the cryocooler. Before being received by the transeiver the signal is split by an identical Wilkinsons.

Having a clear idea of the software to be developed and the specifications to obtain, we opted for COTS components from National Instruments, which are easily implementable and customizable for our needs. In fig. 4.7 is represented in the block diagram our experimental configuration. We used two NI 5791 transceivers (table 4.1) equipped with 2 NI PXIe-7966 fpga (table 4.2). The transceivers are expansion modules directly attached to the FPGA modules. They are tunable up to 4.4 GHz and they are equipped with IQ mixers so being able to generate and acquire both amplitude and phase.



Figure 4.8: The insulated rack with all the warm electronic components.

The full system (FPGA + transceiver) is doubled to cover a band wider than the one of a single transceiver (100 MHz), to cover the band of the KIDs we have in laboratory (as we will see in the next chapter). The two combs are added together by a Wilkinsons power-splitter used as a combiner. The sum of the two signals pass through a PXI Programmable attenuator (PXI-5696, see table 4.3) to reduce the power to avoid KIDs' transition due to the exceeding power and then enter the cryostat through a single cable. The signal emerging from the cryostat is split by an identical Wilkinson and fed into the two transceivers

| <b>NI 5791 R</b>        | <b>RF Transceiver Adapter Module</b>                              |
|-------------------------|---|
| ADC                     | 2-channel, 130 MS/s 14-bit accuracy                               |
| DAC                     | 2-channel, 130MS/s (520 MS/s after interpolation) 16-bit accuracy |
| RF frequency range      | 200 MHz to 4.4 GHz  |
| Instantaneous bandwidth | 100 MHz   |
| EVM                     | <1.5% (RMS)   |

Table 4.1: NI 5791 RF Transceiver main specifications

| <b>PXIe - 7966 R</b> | <b>FPGA Module for Flex-RIO</b> |
|----------------------|---------------------------------|
| FPGA                 | Virtex-5 SX95T                  |
| LUT                  | 58880                           |
| DRAM                 | 512 MB                          |

Table 4.2: PXI-e 7966 FPGA Module main specifications

inputs to be demodulated and acquired. All PXI components are inserted in an 8-slot PXIe - 1082 chassis attached to a Dell Precision 3930 Rack, all placed inside an insulated rack (fig. 4.8).

| <b>PXI - 5695</b>             | <b>RF PXI Attenuator</b>   |
|-------------------------------|--|
| Frequency Range               | 50 MHz to 8 GHz  |
| Attenuation Resolution        | +0.5 dB, typical   |
| Level Calibration Accuracy    | ±0.7dB   |
| Maximum Attenuation           | -44 dB   |
| Gain Variation by Temperature | $-(2.69 * 10^{-4}) * \text{Frequency in GHz) dB/}^{\circ}\text{C}$ |

Table 4.3: PXI 5695 RF Attenuator main specifications

### 4.2.1 Cryostat

The cryostat is the apparatus that allows us to bring our device into the superconductive regime, reaching a temperature of 4 K on the plate where the KIDs are thermally anchored. The cooling system consists of a Gifford - Mc Mahon cryocooler (SHI-RDK 408) capable of reaching 3.3 K with an input power of 0 W and 4 K with an input power of 750 mW. Since the cooling power of our cryostat is very low, we must take care to limit as much as possible the heat load into the apparatus in all its modes of propagation: conduction, convection, and radiation. In order to limit the entry of heat by conduction, we connected the KIDs to the warm electronics with stainless steel coaxial cables (see fig. 4.9). The specific cables are cryogenic coaxial cable by RF-coax 100 mm long. The external jacket made by stainless Steel has a diameter of 0.086" and the center conductor is made of Berillium-Copper. The thermal conductivity is  $0.15 W cm^{-1} K^{-1}$ . Going towards the ports of the KID array, two flexible copper cables connect the steel cables with Niobium cables anchored to the copper plate of the cryostat, in order to limit heat conduction, since at 5 K these cables are in the superconducting state making them poor heat conductors.



Figure 4.9: Inside of the cryostat, with all the cold component of the set-up.

To limit the heat input by convection, a pumping system was used to create a sufficiently high vacuum inside the cryostat. To do this, a dry rotary pump is used up to a pressure of 1 mbar after which a turbomolecular pump is coupled so as to reach pressures around  $10^{-9}$  mbar, amply sufficient to neglect the heat input for convection. Finally, to shield the heat radiated from the external walls of the cryostat, we adopt an electromagnetic shield along the internal walls and above the copper plate, made up of layers of "super-insulating" material consisting of a multilayer of aluminized Mylar sheets inter-

spersed with tulle nets to avoid a direct contact of the Mylar layers avoiding heat conduction from the outer walls to the inside. The rule of thumb is that  $n$  layers of Mylaraluminate reduce to  $1/n$  the heat radiated on the part exposed to the surfaces at the highest temperature which, in our case, are those of the internal screen anchored to the first stage of the cooler which reach about 60 K.

## 4.3 Software

The code of the state machine was done entirely using LabView, a graphical programming software that proved to be a very powerful tool for writing software for electronic automation. With this it was possible to develop at every level necessary, from the FPGA programming, to the development of the Graphical User Interface (GUI) used to verify the received and transmitted signals in real time. Let's see the various steps in detail.

### 4.3.1 FPGA

The FPGA is programmed to take care of the transmission and reception of the signals. There are three main components: one write the look-up table, one read that and the third one generates the outgoing signal and the receive the incoming signal.

The Look-up Table is written only when the program raises the FPGA SAVE flag: every single Unsigned 32 (U32) is saved one by one in the Look-up table, as we can see in the figure 4.10. We are using 1024 element of U32, that contain the I and Q signal (I is in the 16 lower bits, Q is in the 16 higher bits) to be given to the Digital-Analog Converter (DAC) of the transceiver.

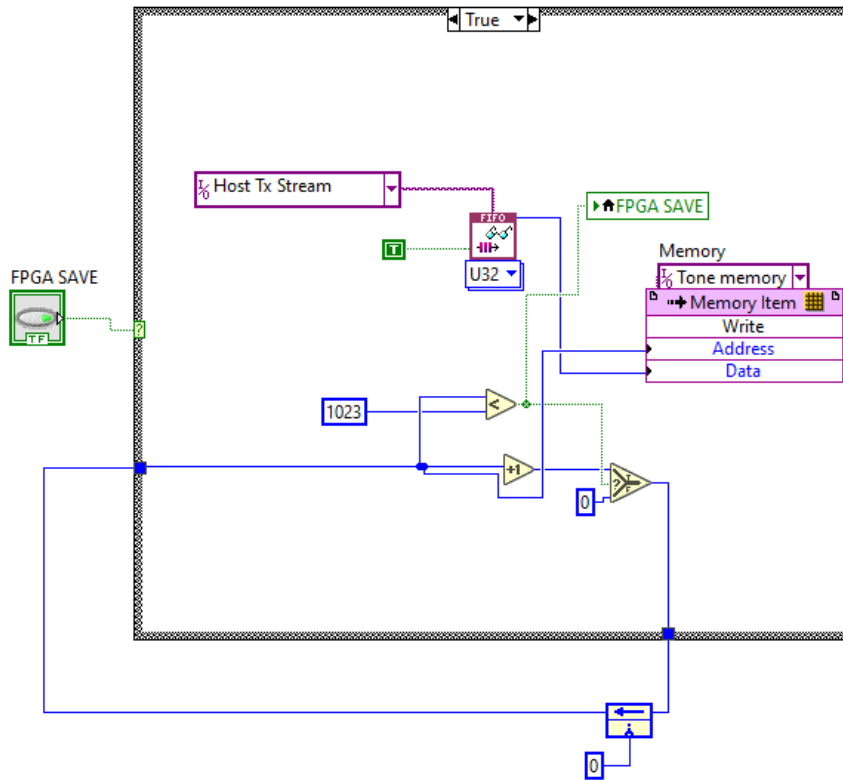


Figure 4.10: Block diagram for the writing of the Look-up table on the FPGA. The data are stored in memory as an array of U32 elements, with the top 16 bit representing the I signal and the bottom 16 bit representing the Q signal.

When the FPGA has to transmit the signal to the DAC, the transmission component comes into operation: each element of the Look-up Table is read one by one, the signal is corrected using Digital Signal Processing (DSP) to calculate the systematic variations due to the DAC used, and finally it is sent to the DAC itself in the I and Q components (see fig. 4.11).

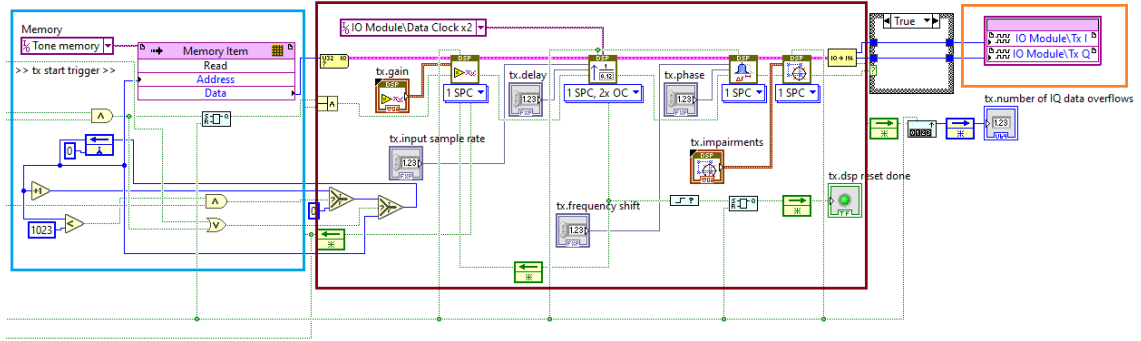


Figure 4.11: Block diagram for the transmission of the signals. Cyan rectangle: the reading of the Look-up table. Red rectangle: DSP of every element I and Q. Orange rectangle: transmission of the I and Q element to the DAC

The third section simply takes care of receiving the signal from the analog-digital converter (ADC) of the transceiver, performing the correction via DSP and sending the received signals to the host (see fig. 4.12).

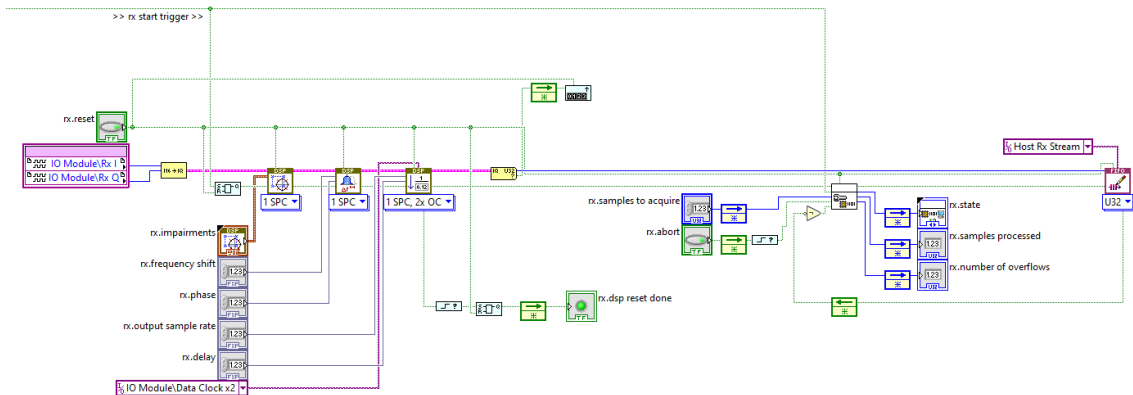


Figure 4.12: Block diagram to receive the signals. The signal pass through a DSP before being sent to the host as an U32 element.

### 4.3.2 Host Computer

The host computer manages the state machine and the construction of the signal. A Graphical User Interface (GUI) that can be seen in figure 4.13 has been developed allowing the user to use the entire hardware to run laboratory tests on KIDs, to have a real-time graph-

ical display of transmitted and received tones and to send the chirp signal or the comb signal. The comb can be generated manually or automatically, with the tones found during the sweep.

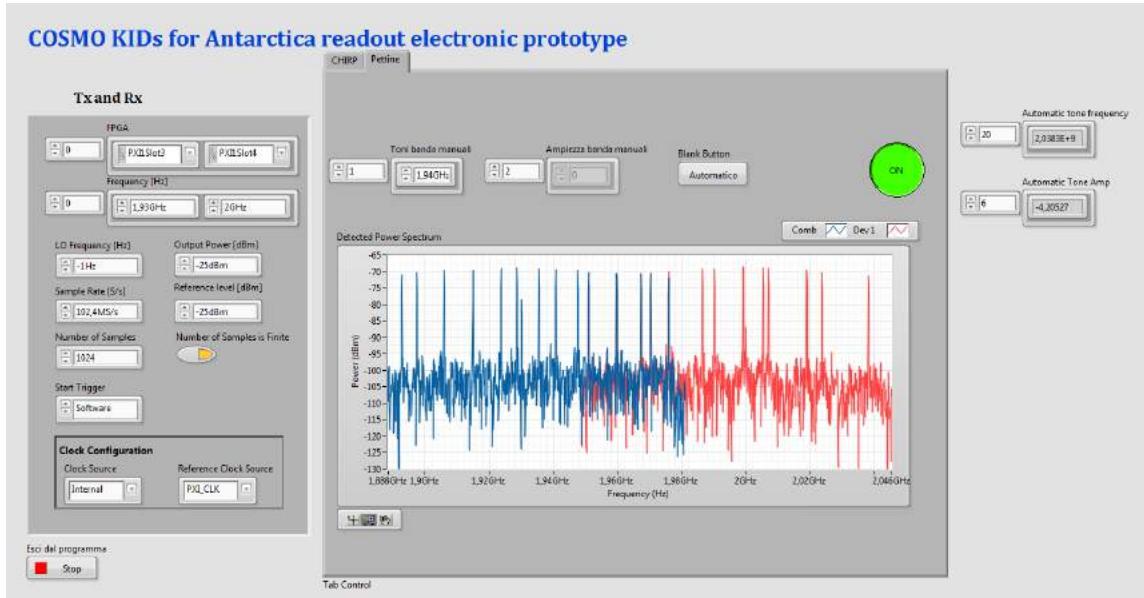


Figure 4.13: GUI for the host. The graph show the comb received from the ADC of the NI 5791

The main blocks are for the transmission and reception of IQ data from the FPGA to the host. The host can be used to analyze the data and save on external media. We save the data in Hierarchical Data Format (hdf5), which allows us to write and read faster than traditional methods. The algorithms that control the 3 states of the machine have been implemented. In the first state the chirp is built using two linear ramps of the length of the number of samples (fig. 4.14). The first starts from the initial frequency and ends at the final frequency and is transformed into an angle in radians, the second from  $t_0$  to  $t_n$ . By multiplying the values together and using them as an angle for  $z = A * e^{i\theta}$  the signal is obtained.

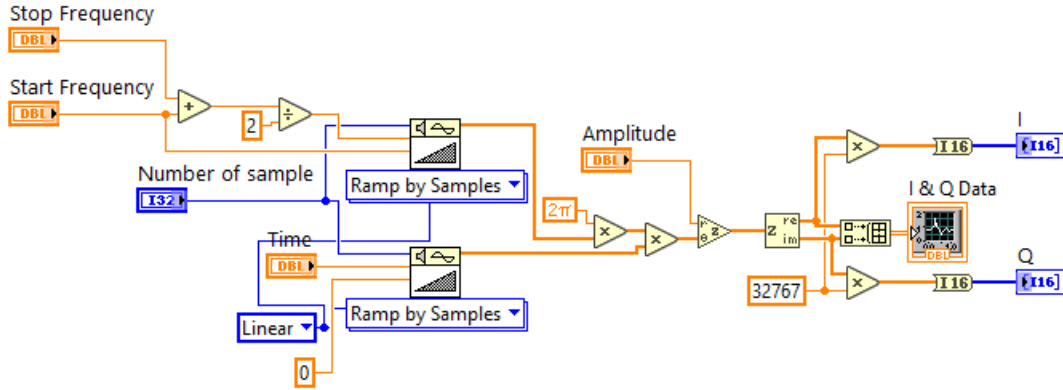


Figure 4.14: Generation of the Chirp signal

The resonances are found with an algorithm that searches for relative minimum and saving the frequencies obtained in an array.

The second state use the rotation mode of the CORDIC algorithm. The value of I and Q calculated for each point (corresponding with the angular frequency of  $\beta = f * 2\pi$ ) using the equation:

$$\begin{bmatrix} x_{i+1} \\ y_{i+1} \end{bmatrix} = K_i \begin{bmatrix} 1 & -\sigma_i 2^{-1} \\ \sigma_i 2^{-1} & 1 \end{bmatrix} \begin{bmatrix} x_i \\ y_i \end{bmatrix} \quad (4.2)$$

$$\beta_{i+1} = \beta_i - \sigma_i \arctan(2^{-1}) \quad (4.3)$$

where  $x_i = \cos(\beta_i) = I$ ,  $y_i = \sin(\beta_i) = Q$ ,  $K_i = \frac{1}{\sqrt{1+2^{-2i}}}$  and  $\sigma_i$  is used to determine the direction of the rotation: +1 if counterclockwise, -1 if clockwise.

In the third state, the main part of the software is given by the DDC. To write it digitally, the received signal is multiplied with the sinusoidal signals of the resonant frequencies, then passed through digital filters and finally the undersampling takes place (see fig. 4.15).

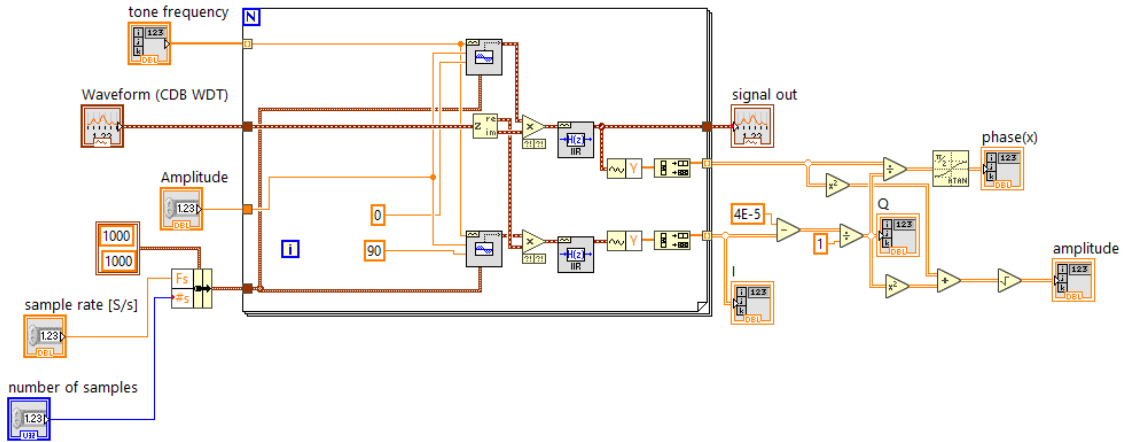


Figure 4.15: DDC block logic. The signal received as a Waveform pass through a DDS (Direct Digital Synthesis), a low passfilter and a downsampler, then for each element the phase and the amplitude of the signal is calculated.

All the array are then saved on the host in HDF5 file.

## 5. Laboratory measurement

In our laboratory we use for testing an array of 25 KIDs in Niobium distributed on a 200 MHz band around 2 GHz, designed at the AstroParticule et Cosmologie lab in Paris and manufactured at Paris Observatory (fig. 5.1). The transition temperature of these KIDs is around 9 K and their measured quality factor resonances,  $Q$ , is higher than 5000 already at 5 K, the equilibrium temperature of our cryofacility in the current set-up. The  $Q$  factor value is enough for our purpose, since we need to have well defined resonances with a frequency spacing around 5-10 MHz.

Using a Vector Network Analyzer (Keysight N5245A) we founded the resonances reported on table 5.1 and fig. 5.2

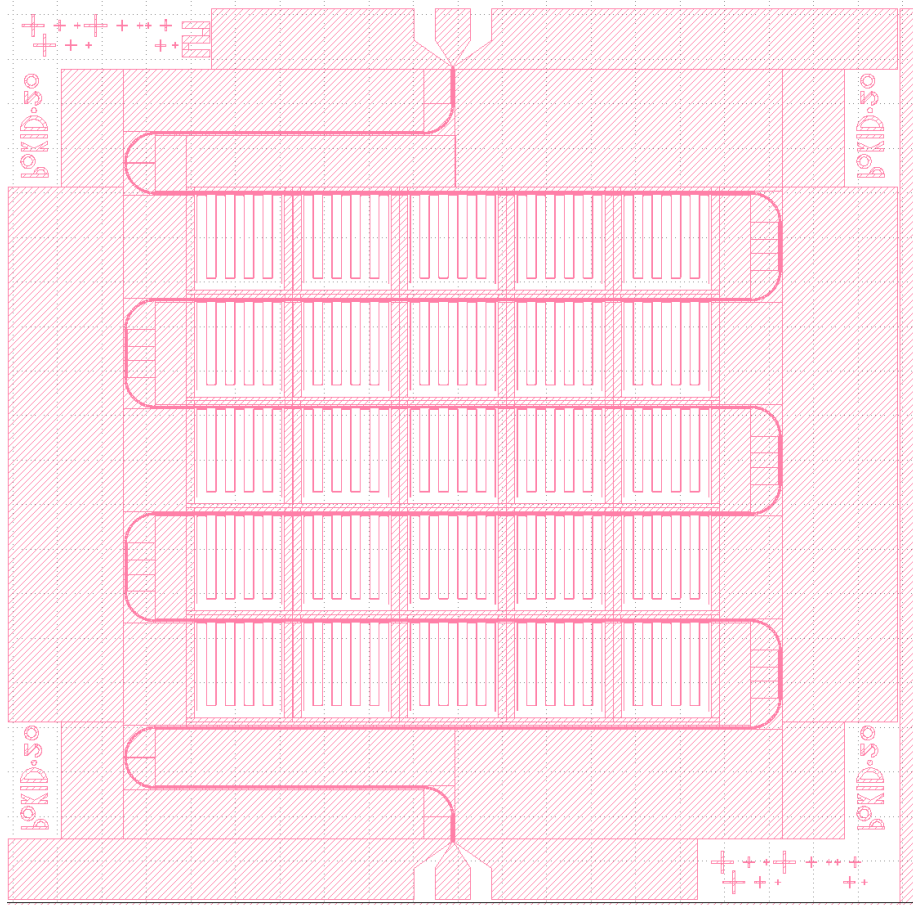


Figure 5.1: Design of the array of 25 Niobium KIDs, from Astroparticule et Cosmologie lab in Paris.

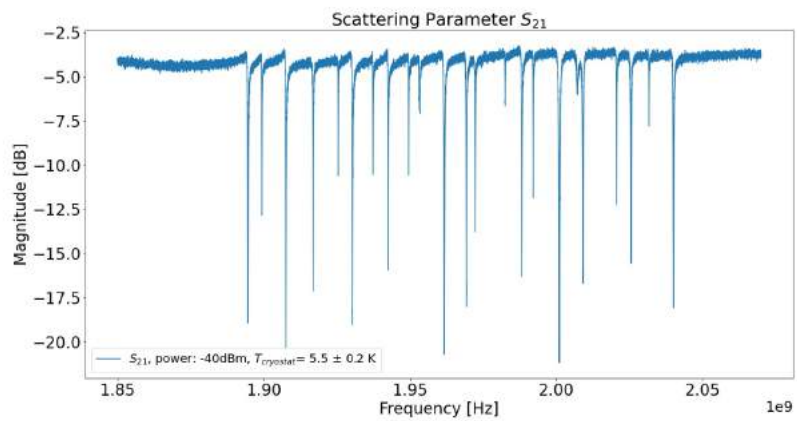


Figure 5.2: The sweep response of the 25 Niobium Kids. 23 resonance are visible in the figure.

| <b>Frequency [GHz]</b> | <b>dB</b>     |
|------------------------|---------------|
| 1.894594 ± 0.000001    | -18.92 ± 0.01 |
| 1.899302 ± 0.000001    | -12.83 ± 0.01 |
| 1.907618 ± 0.000001    | -20.37 ± 0.01 |
| 1.916902 ± 0.000001    | -17.12 ± 0.01 |
| 1.925482 ± 0.000001    | -10.60 ± 0.01 |
| 1.930355 ± 0.000001    | -19.02 ± 0.01 |
| 1.937384 ± 0.000001    | -10.53 ± 0.01 |
| 1.942543 ± 0.000001    | -15.94 ± 0.01 |
| 1.949561 ± 0.000001    | -10.56 ± 0.01 |
| 1.953378 ± 0.000001    | -7.06 ± 0.01  |
| 1.961760 ± 0.000001    | -20.70 ± 0.01 |
| 1.969317 ± 0.000001    | -18.00 ± 0.01 |
| 1.972364 ± 0.000001    | -13.77 ± 0.01 |
| 1.982594 ± 0.000001    | -6.63 ± 0.01  |
| 1.988281 ± 0.000001    | -16.30 ± 0.01 |
| 1.992164 ± 0.000001    | -11.85 ± 0.01 |
| 2.001063 ± 0.000001    | -21.17 ± 0.01 |
| 2.0074 ± 0.000001      | -2.93 ± 0.01  |
| 2.009214 ± 0.000001    | -16.69 ± 0.01 |
| 2.020654 ± 0.000001    | -12.22 ± 0.01 |
| 2.025626 ± 0.000001    | -15.54 ± 0.01 |
| 2.031764 ± 0.000001    | -7.80 ± 0.01  |
| 2.040157 ± 0.000001    | -18.06 ± 0.01 |

Table 5.1: List of the resonance frequencies and the related attenuation of our Niobium KIDs founded with a VNA

As shown in Fig. 5.2 and in the table 5.2, to cover a bandwidth of 200 MHz, we work with two parallel transceiver, which bands are partially overlap. We decided to add a test tone for each FPGA, respectively at 1.9030GHz for the first, and 1.9760GHz for the second one. Thus, at the end we can receive and transmit a total of 25 tones. We chose those frequency values for the test tone because there the signal is not attenuated by any other close resonance. The presence of the test tones allows us to check the behaviour of the resonant tones with the fluctuation of temperature.

To date, we can reach a sampling rate of around 12 kHz on the 25 frequencies (23 effective resonances plus 2 test tones) saving the data in HDF5 format. However, we are still a factor of 5 far from the COSMO requirements (sampling rate at about 60 kHz). Currently we are improving the data saving in order to increase the sampling rate and we are exploring all the possibilities given by the HDF5 format. We also plan to improve the data rate synthesizing the calculus of the amplitude and phase shift of each tone on the FPGA instead on the host computer.

During the data taking we also collect the temperatures inside the cryostat. The temperature have oscillations of  $\sim 20$  mK around the mean value, with a frequency  $\sim 1$  Hz, typical of the cooler cold head cycle. The temperature oscillations make the initial search for resonators difficult because the frequencies of the resonances are not stable and for this reason we need to repeat the sweep multiple times. The aim of this process is to map the oscillations of the resonances and find the minimum transmission. The state of minimum transmission corresponds to the minimum temperature achieved by the cryocooler with the installed set-up and consequentially gives the information about the tone of each resonance. However, these annoying oscillations reveal to be useful to test some key parameters of the readout system:

- they are used to verify that the system can track the tones during testing phase;
- their presence is a prominent feature that should be clearly visible in the phase time stream plot and in the rolling mean amplitude time stream plot

| <b>Frequency [GHz]</b> | <b>dB</b>         |
|------------------------|-------------------|
| $1.8945 \pm 0.0001$    | $-8.58 \pm 0.01$  |
| $1.8992 \pm 0.0001$    | $-4.18 \pm 0.01$  |
| $1.9075 \pm 0.0001$    | $-10.54 \pm 0.01$ |
| $1.9168 \pm 0.0001$    | $-8.80 \pm 0.01$  |
| $1.9254 \pm 0.0001$    | $-4.39 \pm 0.01$  |
| $1.9303 \pm 0.0001$    | $-8.35 \pm 0.01$  |
| $1.9374 \pm 0.0001$    | $-3.01 \pm 0.01$  |
| $1.9426 \pm 0.0001$    | $-6.84 \pm 0.01$  |
| $1.9496 \pm 0.0001$    | $-3.24 \pm 0.01$  |
| $1.9532 \pm 0.0001$    | $-6.49 \pm 0.01$  |
| $1.9617 \pm 0.0001$    | $-11.83 \pm 0.01$ |
| $1.9693 \pm 0.0001$    | $-9.70 \pm 0.01$  |
| $1.9723 \pm 0.0001$    | $-7.62 \pm 0.01$  |
| $1.9826 \pm 0.0001$    | $-2.02 \pm 0.01$  |
| $1.9884 \pm 0.0001$    | $-9.16 \pm 0.01$  |
| $1.9922 \pm 0.0001$    | $-4.38 \pm 0.01$  |
| $2.0011 \pm 0.0001$    | $-11.42 \pm 0.01$ |
| $2.0074 \pm 0.0001$    | $-2.93 \pm 0.01$  |
| $2.0093 \pm 0.0001$    | $-11.26 \pm 0.01$ |
| $2.0208 \pm 0.0001$    | $-6.28 \pm 0.01$  |
| $2.0258 \pm 0.0001$    | $-9.53 \pm 0.01$  |
| $2.0318 \pm 0.0001$    | $-3.01 \pm 0.01$  |
| $2.0402 \pm 0.0001$    | $-11.85 \pm 0.01$ |

Table 5.2: List of the resonance frequency and the relative attenuation of our Niobium KIDs computed at the minimum temperature of  $T = 4.85$  K

## 5.1 Measurements with KIDs

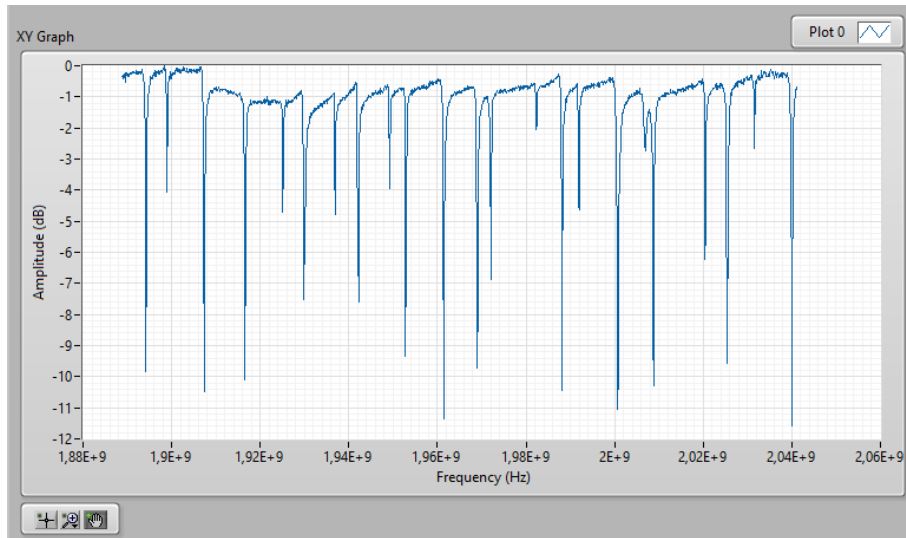


Figure 5.3: The result of the chirp through the KIDs. We can see all the resonances of our array of KIDs

A typical test of our readout lasts for one hour, collecting data for all the 25 frequencies transmitted using the comb technique, and founded with the chirp as we can see from the fig. 5.3. We check for the presence of temperature oscillations and compare them with phase oscillations. In figure 5.4 we can see how the oscillations of phase and temperature agree with the same period, while the tone placed where there are no resonant frequencies does not show clear oscillations.

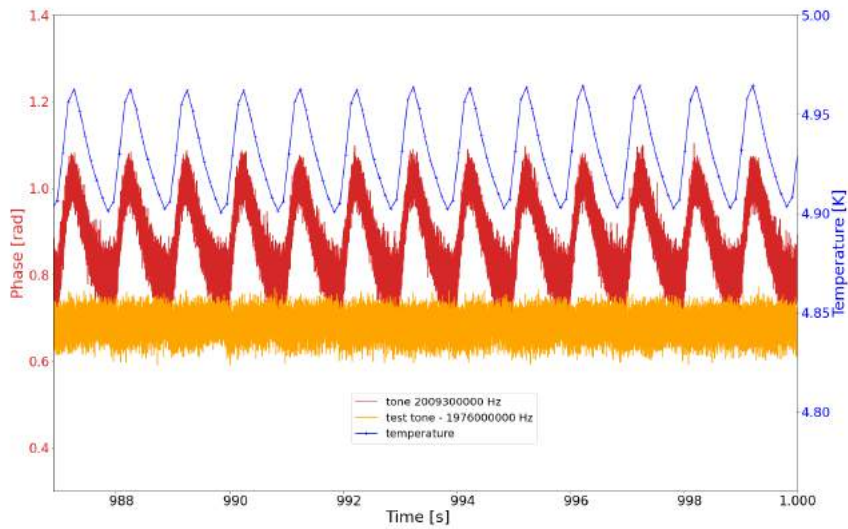


Figure 5.4: Blue: temperature oscillation. Red: phase oscillation of the tone at 2.0093 GHz. Yellow: phase oscillation of the test tone at 1.9760 GHz.

If we evaluate the IQ plane, we can see how the temperature oscillations show a trend in agreement with the theory, with modifications of the I and Q values due to the variation of the value of the resonant frequency with the variation of the temperature, with consequent variation of the amplitude and phase of the transmitted and received tone. While this happens on the tone at 2.0093 GHz, as we can see on fig. 5.5, this doesn't happen on the tone at 1.9876 GHz, as we can see on fig. 5.6.

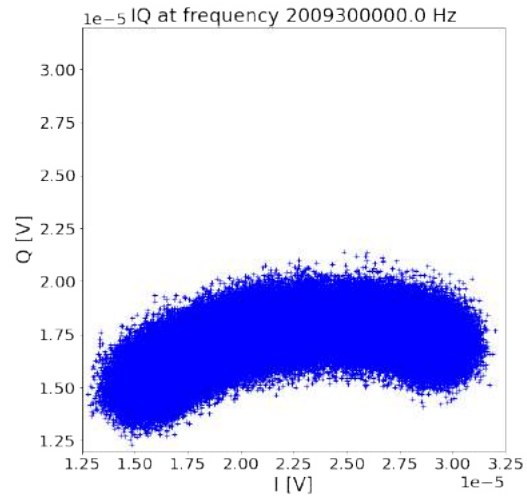


Figure 5.5: IQ for the tone at frequency 2.0093 GHz

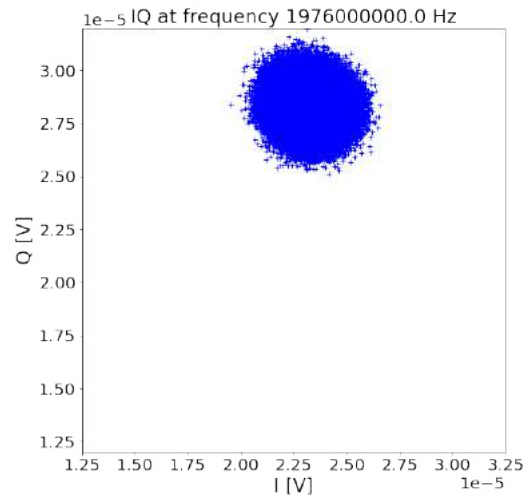


Figure 5.6: IQ for the test tone at frequency 1.9760 GHz

In order to characterize the Phase Noise of both the electronics and eventually disentangle it from that of the detectors we acquired, we performed a Power Spectrum Density to highlight the signal corresponding to the various frequencies of our interest, especially the 1 Hz temperature oscillations. This showed a peak at 1 Hz due to temperature oscillations for the 2.0093 GHz tone, as we can see in the fig5.7, but also showed a peak for the test tone, as we can see in the fig5.8.

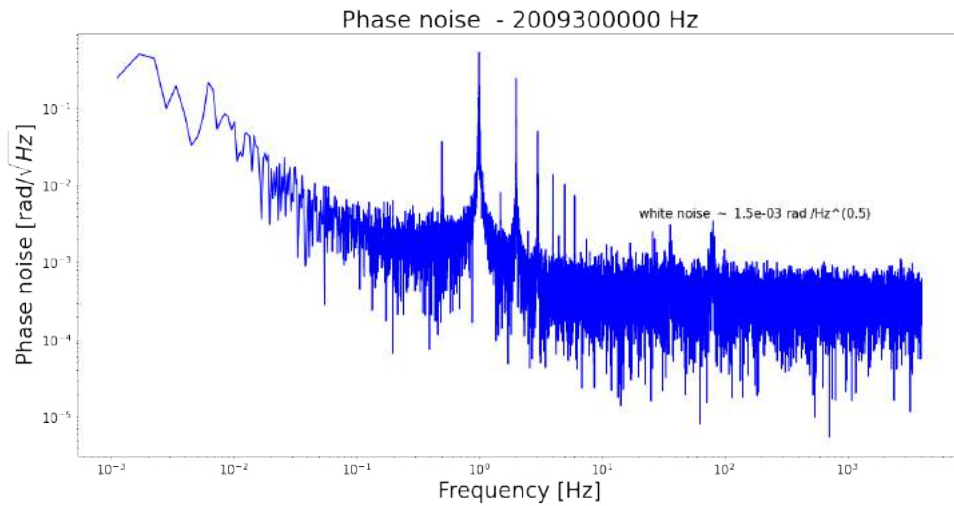


Figure 5.7: Phase Noise for the tone at frequency 2.0093 GHz.

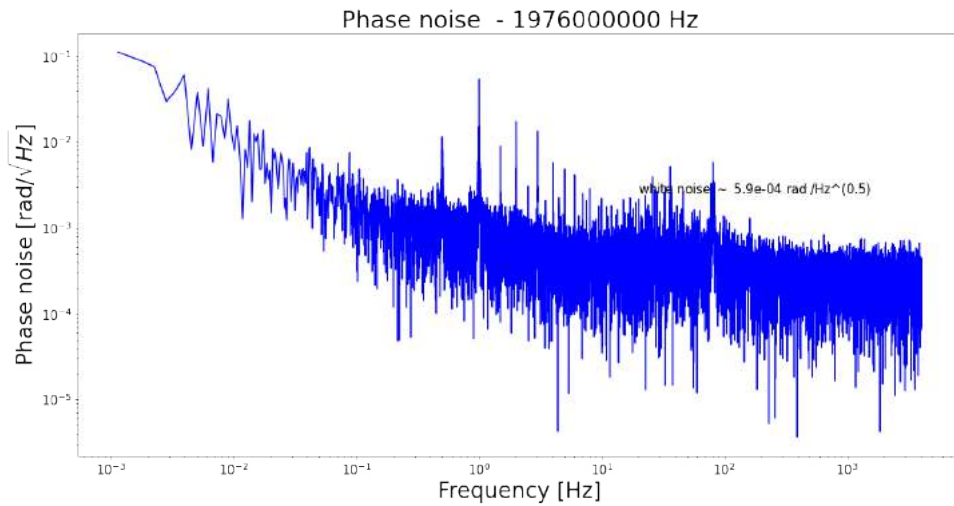


Figure 5.8: Phase Noise for the test tone at frequency 1.9760 GHz.

## 5.2 Measurement of Warm and Cold Loop

To estimate the noise due to the electronics alone, auxiliary measurements are needed, in which the signal does not pass through the detector. To carry out these measurements we

| <b>Frequency [GHz]</b> | <b>rad/<math>\sqrt{Hz}</math></b> |
|------------------------|-----------------------------------|
| 1.8945                 | $1.3 \cdot 10^{-3}$               |
| 1.8992                 | $9.0 \cdot 10^{-4}$               |
| 1.9030                 | $5.0 \cdot 10^{-4}$               |
| 1.9075                 | $1.4 \cdot 10^{-3}$               |
| 1.9168                 | $1.2 \cdot 10^{-3}$               |
| 1.9254                 | $8.4 \cdot 10^{-4}$               |
| 1.9303                 | $1.1 \cdot 10^{-3}$               |
| 1.9374                 | $6.1 \cdot 10^{-4}$               |
| 1.9426                 | $7.3 \cdot 10^{-4}$               |
| 1.9496                 | $5.7 \cdot 10^{-4}$               |
| 1.9532                 | $1.0 \cdot 10^{-3}$               |
| 1.9617                 | $2.0 \cdot 10^{-3}$               |
| 1.9693                 | $9.5 \cdot 10^{-4}$               |
| 1.9723                 | $1.3 \cdot 10^{-3}$               |
| 1.9760                 | $7.4 \cdot 10^{-4}$               |
| 1.9826                 | $8.6 \cdot 10^{-4}$               |
| 1.9884                 | $8.5 \cdot 10^{-4}$               |
| 1.9922                 | $9.0 \cdot 10^{-4}$               |
| 2.0011                 | $1.4 \cdot 10^{-3}$               |
| 2.0074                 | $1.1 \cdot 10^{-3}$               |
| 2.0093                 | $1.1 \cdot 10^{-3}$               |
| 2.0208                 | $1.5 \cdot 10^{-3}$               |
| 2.0258                 | $1.9 \cdot 10^{-3}$               |
| 2.0318                 | $1.4 \cdot 10^{-3}$               |
| 2.0402                 | $1.3 \cdot 10^{-3}$               |

Table 5.3: List of the resonance frequency and their computed white noise

have considered two configurations: one called Warm Loop, where the output signal from the transceiver passes through all the room temperature devices, connecting the input and output cables from the cryostat to each other via an I. The signals generated from the doubled system (FPGA + transceiver) is added together by a Wilkinsons powersplitter, used as a combiner. The sum of the two signals pass through the PXI Programmable attenuator, pass through the cable that bring the signal to the cryostat. Here it is connected to the cable which carries the signal out of the cryostat to the second Wilkinsons powersplitter and fed to the two transceiver inputs to be demodulated and acquired. The signal sent is composed by the 25 tones, corresponding to the resonance frequencies of the KIDs in use. The second configuration includes also the connections placed at cryogenic temperature, passing through all the cables present inside the cryostat but the KIDs. This second connection is therefore a female-female adapter placed inside the cryostat and anchored to the copper plate. In the table 5.5 and 5.4 we can see the value of the white noise calculated.

### **5.2.1 Warm Loop**

We collected data for 1 hour with a sampling rate of 12 KHz, saving the I and Q data and the time in HDF5 format. As a representative example, we report the tones at 2.0093 GHz and 1.9760 GHz: the first corresponds to the resonance frequency of one of the KIDs, chosen because it is one of the deepest and most isolated from other frequencies; the second corresponds to a section free from resonant frequencies, it is a test tone to observe the signal that is transmitted outside all resonant frequencies and for which we expect no alteration. In these loops we will not have big differences in the detected signal, but they will be relevant during the measurements with the KIDs.

As before, we look at the phase of the 2 signal, and we can see in figure 5.9 and 5.10 that there is no oscillation, because there is no variation of temperature, since this loop doesn't pass through the cryostat.

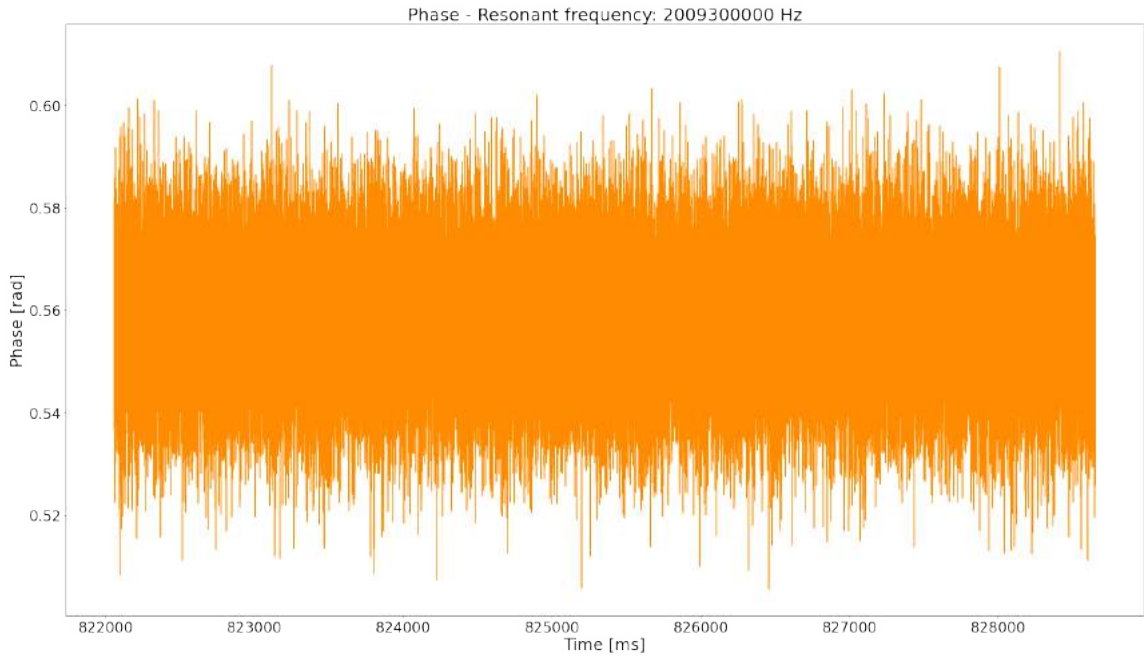


Figure 5.9: Sample of detected Phase for the tone at frequency 2.0093 GHz.

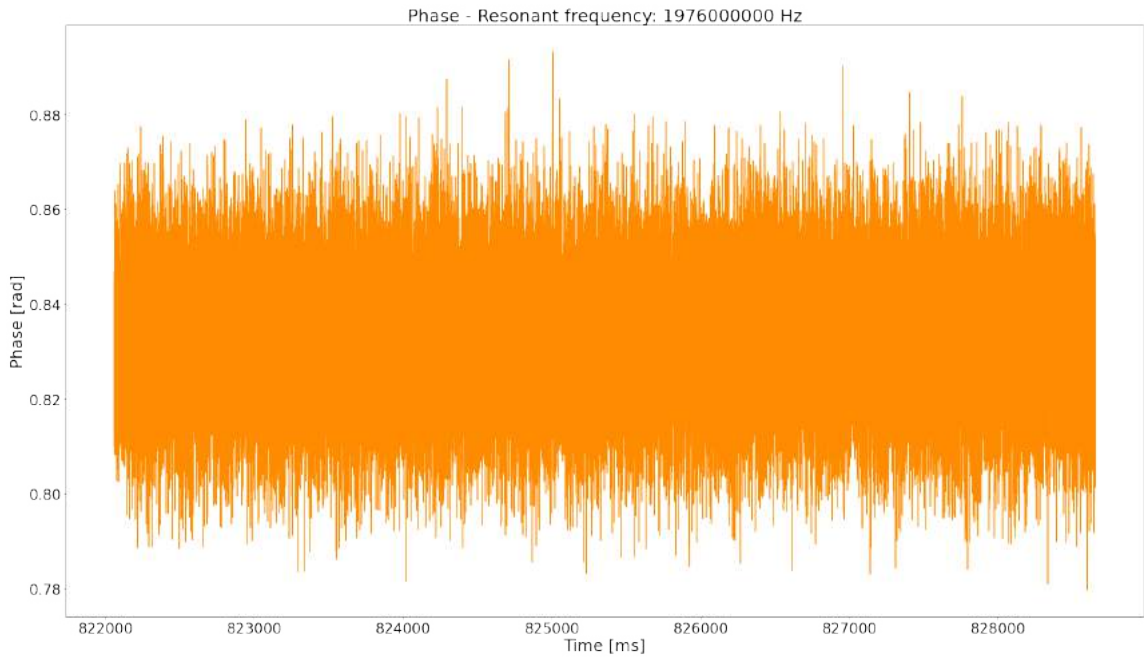


Figure 5.10: Sample of detected Phase for the test tone at frequency 1.9760 GHz.

Even the IQ graph doesn't show difference.

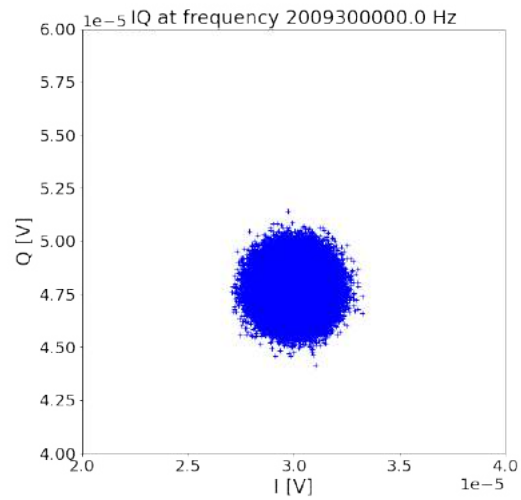


Figure 5.11: IQ for the tone at frequency 2.0093 GHz.

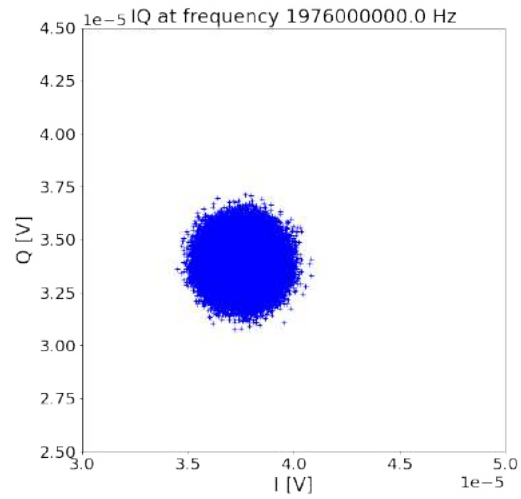


Figure 5.12: IQ for the test tone at frequency 1.9760 GHz.

The phase noise is a figure of merit to see the white noise of the warm readout. We evaluated a white noise of  $\sim 1.8 \cdot 10^{-4} \text{rad}/\sqrt{\text{Hz}}$  for the tone at 2.0093 GHz, and  $\sim 1.9 \cdot 10^{-4} \text{rad}/\sqrt{\text{Hz}}$  for the tone at 1.976 GHz.

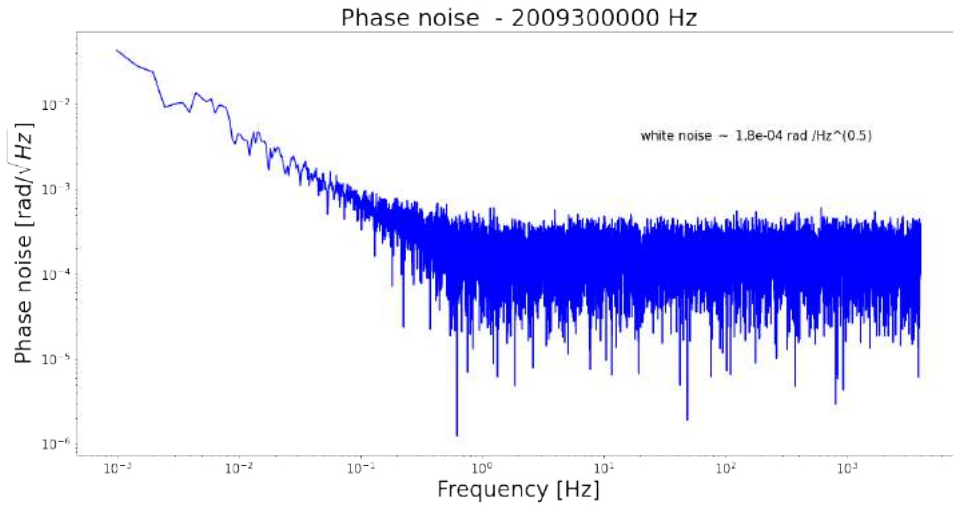


Figure 5.13: Phase Noise for the tone at frequency 2.0093 GHz.

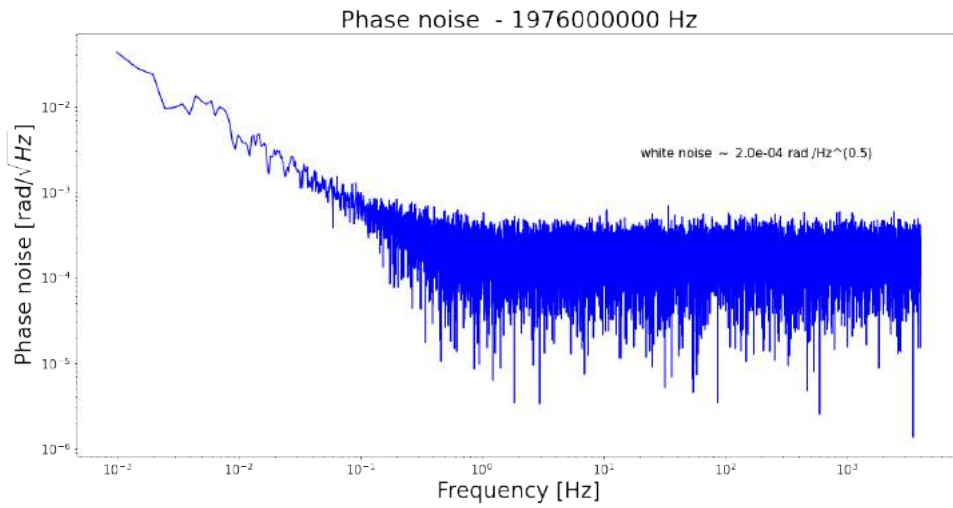


Figure 5.14: Phase Noise for the test tone at frequency 1.9760 GHz.

## 5.2.2 Cold Loop

The last measurement we performed is the cold loop: the signal passing through the warm cables and inside the cryostat, while not going through the KIDs. The phase of the two tones, if plotted, doesn't seem to respond to the variation of temperatures inside the Cryo-

| <b>Frequency [GHz]</b> | <b>rad/<math>\sqrt{Hz}</math></b> |
|------------------------|-----------------------------------|
| 1.8945                 | $2.0 \cdot 10^{-4}$               |
| 1.8992                 | $1.9 \cdot 10^{-4}$               |
| 1.9030                 | $1.9 \cdot 10^{-4}$               |
| 1.9075                 | $1.8 \cdot 10^{-4}$               |
| 1.9168                 | $1.7 \cdot 10^{-4}$               |
| 1.9254                 | $1.6 \cdot 10^{-4}$               |
| 1.9303                 | $2.0 \cdot 10^{-4}$               |
| 1.9374                 | $1.7 \cdot 10^{-4}$               |
| 1.9426                 | $1.8 \cdot 10^{-4}$               |
| 1.9496                 | $1.8 \cdot 10^{-4}$               |
| 1.9532                 | $1.8 \cdot 10^{-4}$               |
| 1.9617                 | $2.0 \cdot 10^{-4}$               |
| 1.9693                 | $2.0 \cdot 10^{-4}$               |
| 1.9723                 | $2.0 \cdot 10^{-4}$               |
| 1.9760                 | $1.9 \cdot 10^{-4}$               |
| 1.9826                 | $1.9 \cdot 10^{-4}$               |
| 1.9884                 | $1.9 \cdot 10^{-4}$               |
| 1.9922                 | $1.9 \cdot 10^{-4}$               |
| 2.0011                 | $3.0 \cdot 10^{-4}$               |
| 2.0074                 | $1.8 \cdot 10^{-4}$               |
| 2.0093                 | $1.7 \cdot 10^{-4}$               |
| 2.0208                 | $1.9 \cdot 10^{-4}$               |
| 2.0258                 | $2.1 \cdot 10^{-4}$               |
| 2.0318                 | $2.0 \cdot 10^{-4}$               |
| 2.0402                 | $2.1 \cdot 10^{-4}$               |

Table 5.4: List of the resonance frequency and the white noise calculated for the warm loop.

stat, as we can see in figures 5.15 and 5.16.

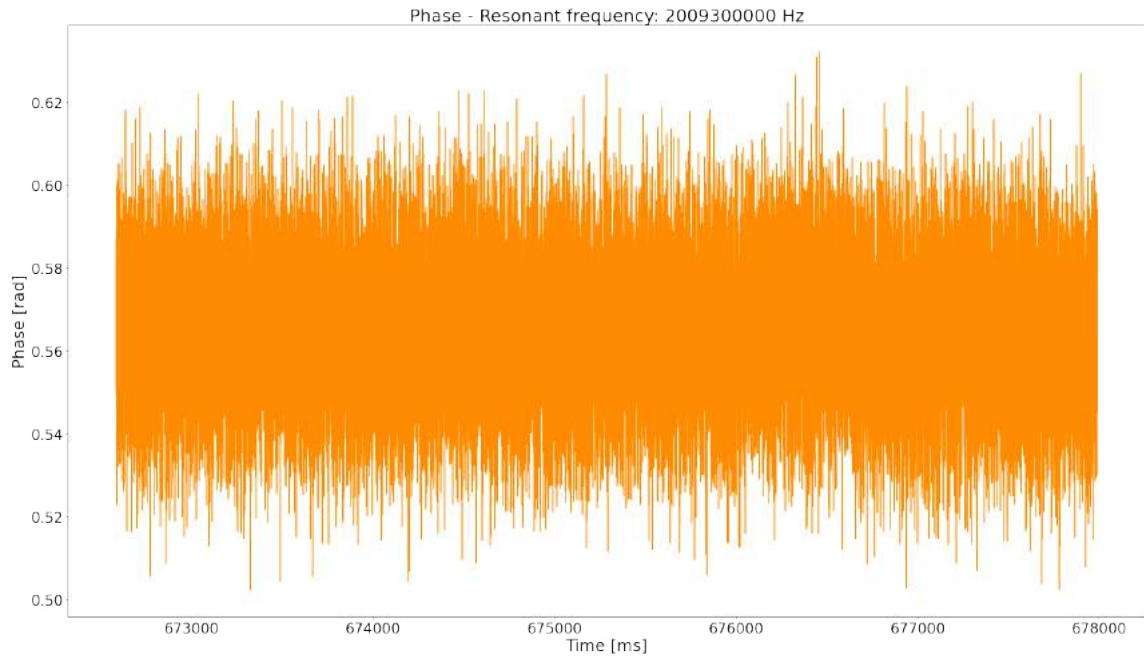


Figure 5.15: Phase for the tone at frequency 2.0093 GHz.

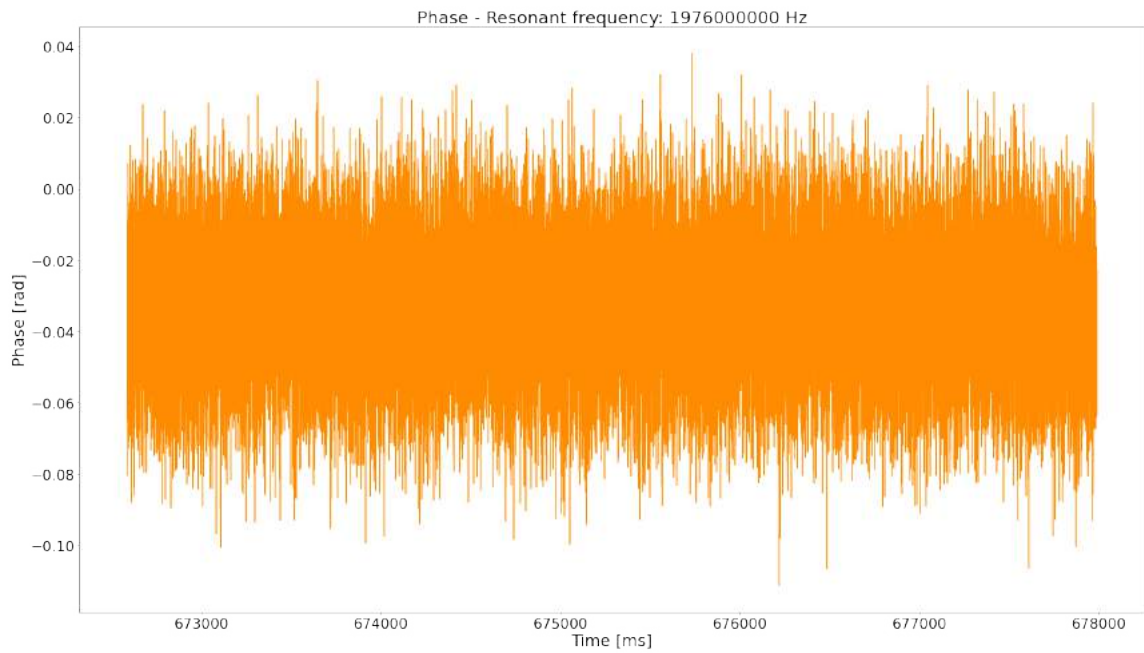


Figure 5.16: Phase for the test tone at frequency 1.9760 GHz.

Even the IQ graph doesn't show difference.

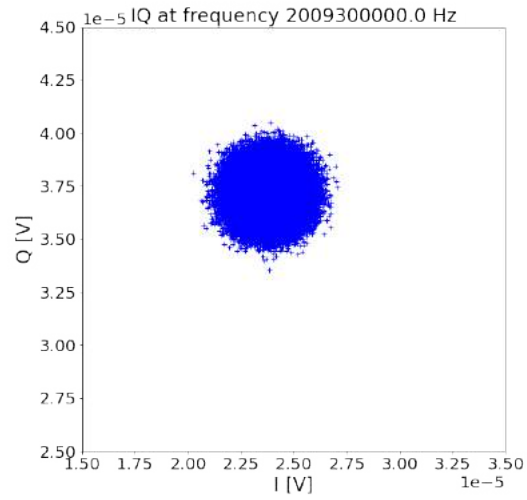


Figure 5.17: IQ for the tone at frequency 2.0093 GHz.

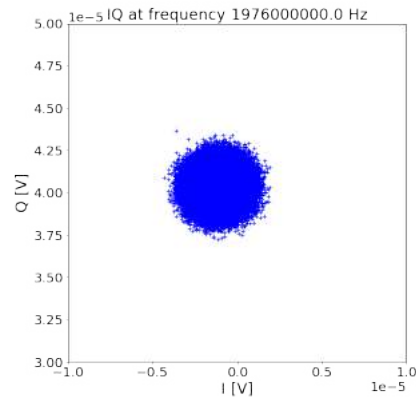


Figure 5.18: IQ for the test tone at frequency 1.9760 GHz.

The phase noise give us a valuable asset: we can see a peak at 1 Hz, in both tones, even if the signal doesn't pass through the KIDs. We estimated that this is due to the Niobium cables inside the cryostat, as they change their attenuation properties as the temperature change.

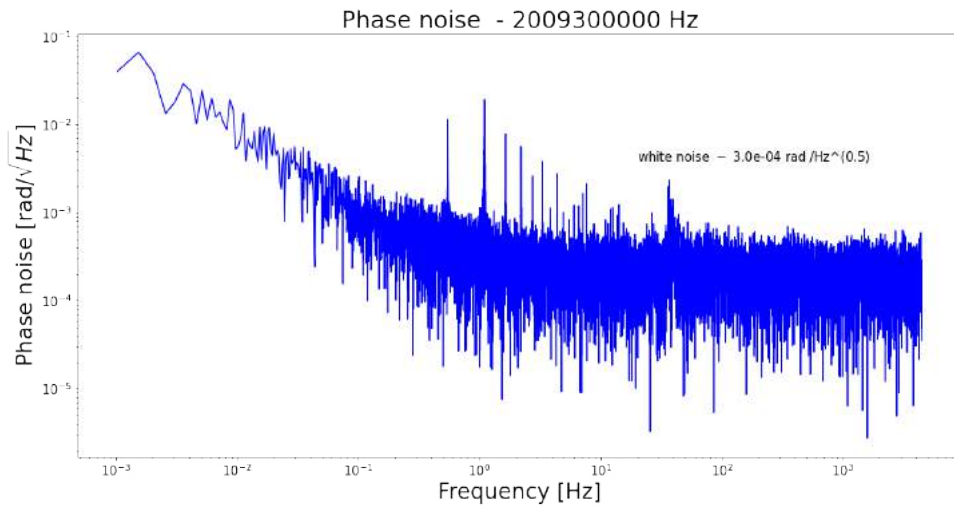


Figure 5.19: Phase Noise for the tone at frequency 2.0093 GHz.

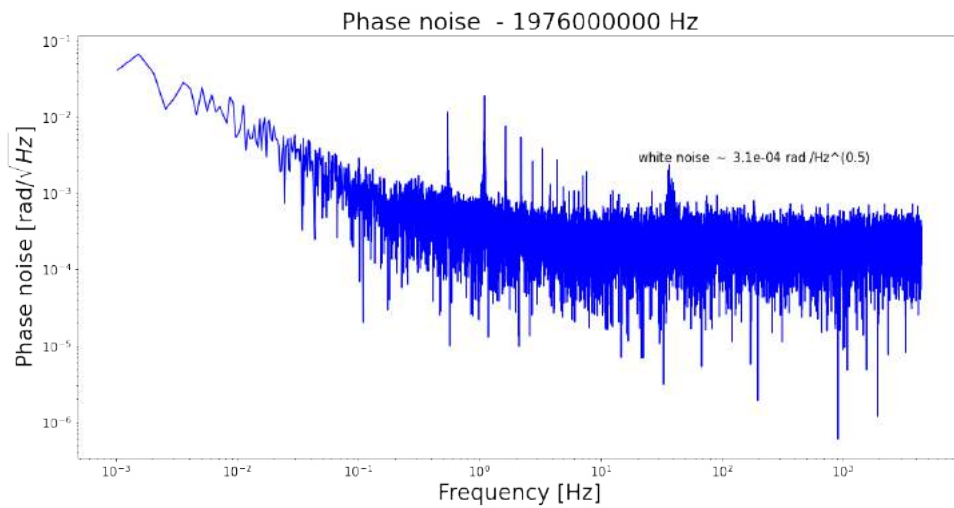


Figure 5.20: Phase Noise for the test tone at frequency 1.9760 GHz.

### 5.3 New measurement

We refined the set-up the inside of the cryostat to lower the base temperature as much as possible. This shifted all the resonance Frequency, as reported in table 5.6.

| <b>Frequency [GHz]</b> | <b>rad/<math>\sqrt{\text{Hz}}</math></b> |
|------------------------|--|
| 1.8945                 | $4.5 \cdot 10^{-4}$                      |
| 1.8992                 | $4.5 \cdot 10^{-4}$                      |
| 1.9030                 | $4.4 \cdot 10^{-4}$                      |
| 1.9075                 | $4.4 \cdot 10^{-4}$                      |
| 1.9168                 | $4.4 \cdot 10^{-4}$                      |
| 1.9254                 | $4.4 \cdot 10^{-4}$                      |
| 1.9303                 | $4.8 \cdot 10^{-4}$                      |
| 1.9374                 | $4.5 \cdot 10^{-4}$                      |
| 1.9426                 | $4.6 \cdot 10^{-4}$                      |
| 1.9496                 | $4.5 \cdot 10^{-4}$                      |
| 1.9532                 | $4.6 \cdot 10^{-4}$                      |
| 1.9617                 | $4.7 \cdot 10^{-4}$                      |
| 1.9693                 | $4.4 \cdot 10^{-4}$                      |
| 1.9723                 | $4.4 \cdot 10^{-4}$                      |
| 1.9760                 | $4.4 \cdot 10^{-4}$                      |
| 1.9826                 | $4.4 \cdot 10^{-4}$                      |
| 1.9884                 | $4.4 \cdot 10^{-4}$                      |
| 1.9922                 | $4.4 \cdot 10^{-4}$                      |
| 2.0011                 | $5.6 \cdot 10^{-4}$                      |
| 2.0074                 | $4.2 \cdot 10^{-4}$                      |
| 2.0093                 | $4.3 \cdot 10^{-4}$                      |
| 2.0208                 | $4.6 \cdot 10^{-4}$                      |
| 2.0258                 | $4.9 \cdot 10^{-4}$                      |
| 2.0318                 | $5.1 \cdot 10^{-4}$                      |
| 2.0402                 | $5.4 \cdot 10^{-4}$                      |

Table 5.5: List of the resonance frequency and the white noise calculated for the cold loop.

| <b>Frequency [GHz]</b> | <b>New Frequency [GHz]</b> | <b>dB</b> |
|------------------------|----------------------------|-----------|
| 1.8945                 | 1.8946                     | -8.48     |
| 1.8992                 | 1.8993                     | -4.41     |
| 1.9075                 | 1.9077                     | -10.02    |
| 1.9168                 | 1.9169                     | -8.90     |
| 1.9254                 | 1.9255                     | -4.30     |
| 1.9303                 | 1.9304                     | -8.74     |
| 1.9374                 | 1.9375                     | -3.38     |
| 1.9426                 | 1.9427                     | -8.46     |
| 1.9496                 | 1.9497                     | -4.28     |
| 1.9532                 | 1.9533                     | -9.34     |
| 1.9617                 | 1.9618                     | -11.53    |
| 1.9693                 | 1.9694                     | -12.17    |
| 1.9723                 | 1.9724                     | -7.21     |
| 1.9826                 | 1.9827                     | -2.31     |
| 1.9884                 | 1.9884                     | -10.98    |
| 1.9922                 | 1.9923                     | -5.84     |
| 2.0011                 | 2.0012                     | -11.26    |
| 2.0074                 | 2.0075                     | -2.85     |
| 2.0093                 | 2.0094                     | -10.81    |
| 2.0208                 | 2.0208                     | -7.61     |
| 2.0258                 | 2.0258                     | -9.75     |
| 2.0318                 | 2.0319                     | -2.75     |
| 2.0402                 | 2.0404                     | -10.51    |

Table 5.6: List of the new resonance frequencies and depths of our Niobium KIDs.

We present a chunk of the phase time stream in fig. 5.21. We decided to show only the tone at resonant frequency 2.00940GHz because it is one of the deepest (-10.81 dB), but we have obtained similar wave-forms for all the other frequency tones. In the same plot we report the temperature oscillations and we can notice a sync between this signal and the phase time stream. This evidence confirms that the KID responds correctly with respect to the variation of the quasi-particles density. At the same time, we can also see the behaviour of the test tone (frequency 1.976GHz), which is not affected by the change of temperature, as expected.

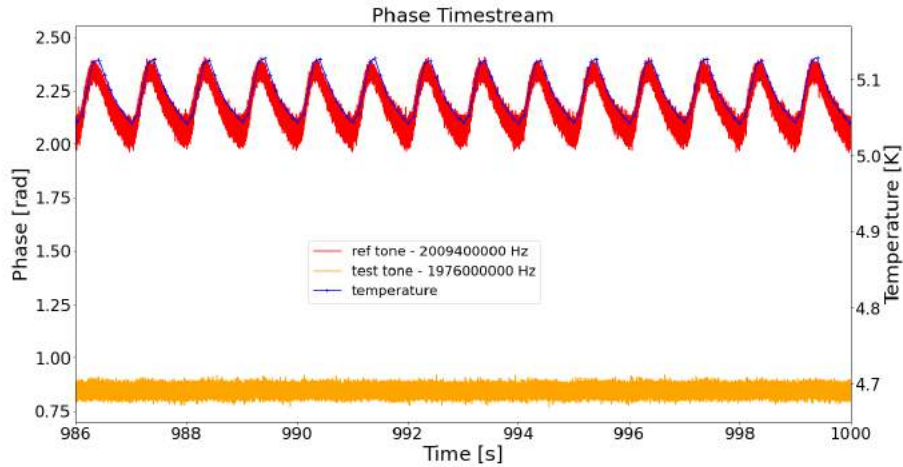


Figure 5.21: Chunk of the phase time stream. The test tone (frequency 1.976 GHz) is plotted in orange, the resonant tone (2.00940 GHz) is in red and the temperature oscillations are in blue.

We present the amplitude time stream of the resonant tone at frequency 2.00940 GHz together with the temperature oscillations. As above, we have obtained similar wave-forms for all the other frequency tones. We performed a moving average on both the amplitude and the temperature data so that we can see the long time fluctuations of the cooler and not the oscillations, that are averaged away. The period of each window is the sampling rate ( $\sim 12000$  Hz) for the amplitude data, while for the temperature data it is 10 Hz, which is the fastest sampling rate of our CTC100 Cryogenic Temperature Controller <sup>2</sup>. As we can

<sup>2</sup><https://www.thinksrs.com/products/ctc100.html>

see in Fig. 5.22 the variation of the moving average of the tone amplitude and the temperature are synchronous, as expected.

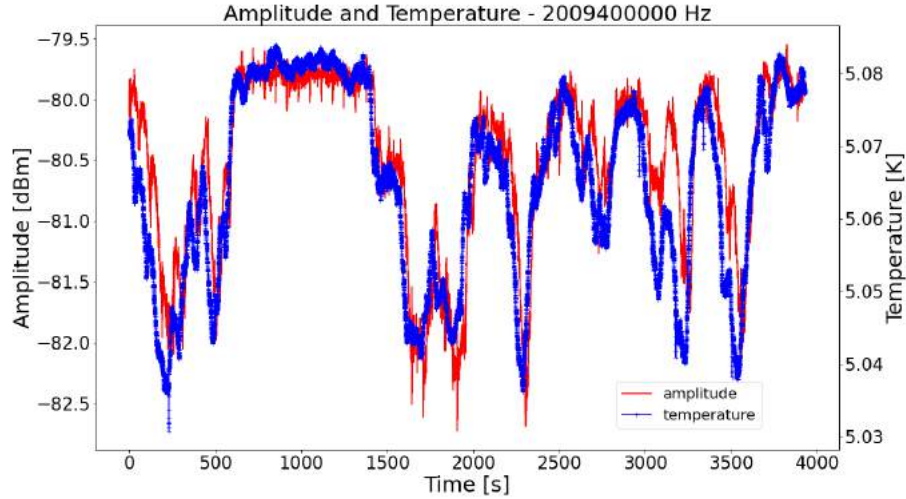


Figure 5.22: Amplitude and temperature time stream. The resonant tone (2.00940 GHz) is in red and the temperature is in blue.

We performed the noise analysis by comparing the phase noise in three different conditions: when the signal passes through the KIDs, when there are no KIDs (cold loop back), and when the signal does not enter in the cryostat (warm loop back). We report the result for the 2.00940 GHz resonant tone in Fig. 5.23 regarding the phase noise, in Fig. 5.24 we did the same analysis but using the test tone (1.976 GHz).

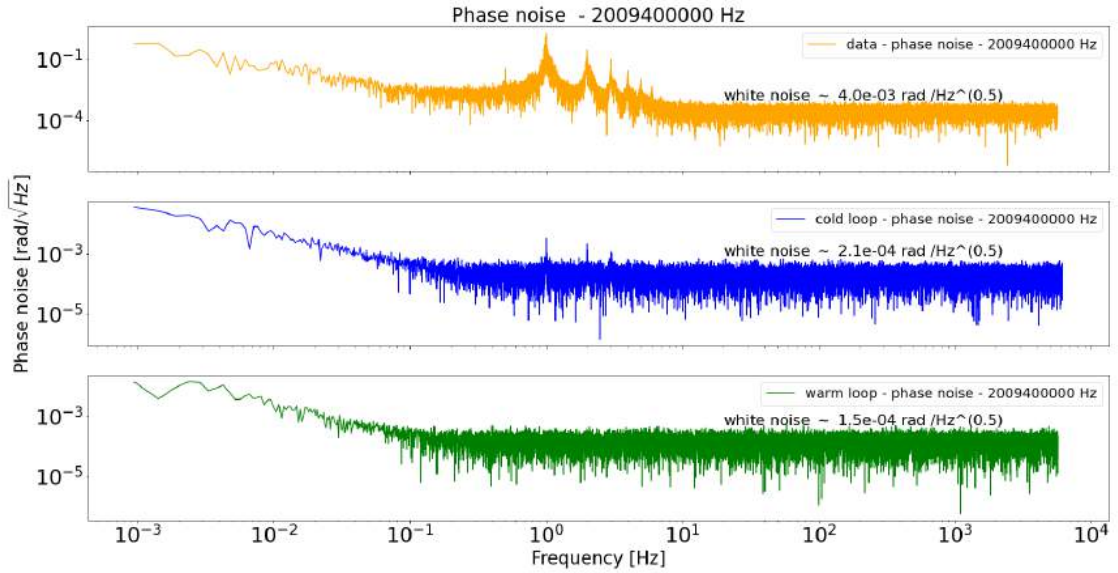


Figure 5.23: Phase noise of the reference tone (2.00940 GHz) in three different conditions. Up: when the signal passes through the KIDs. Middle: when there are no KIDs. Down: when the signal does not enter in the cryostat.

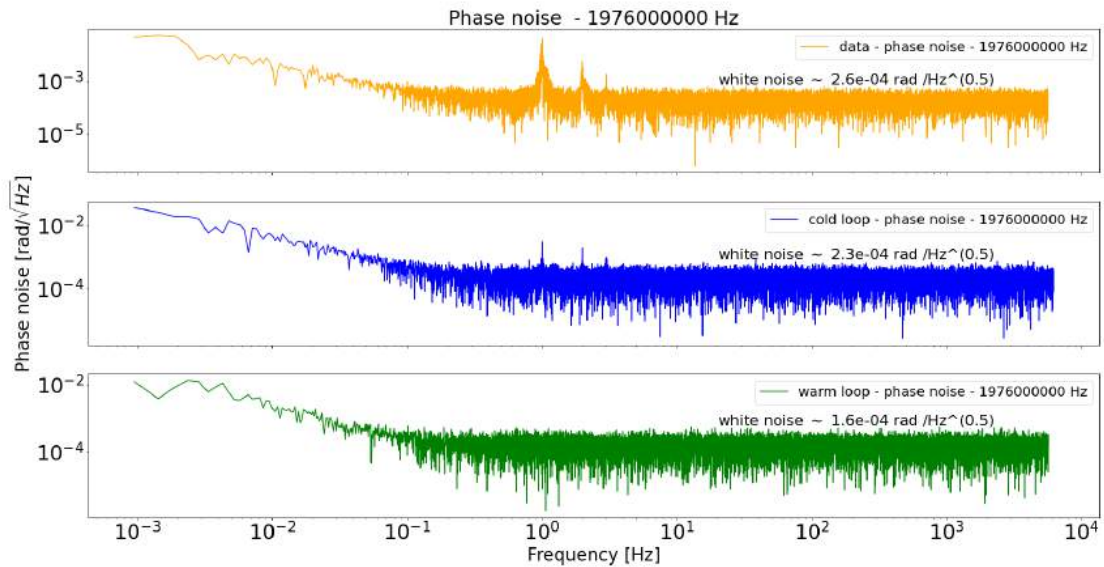


Figure 5.24: Phase noise of the test tone (1.976 GHz) in three different conditions. Up: when the signal passes through the KIDs. Middle: when there are no KIDs. Down: when the signal does not enter in the cryostat.

## 5.4 Comparison with other experiments

We compared the results obtained on noise levels with the results obtained in the literature from other experiments and studies that used KIDS. One of the first comparisons we made is with the OLIMPO experiment[46]. The OLIMPO experiment used an array of 120 KIDS, with a readout electronics based on the Re-configurable Open Access Computer Hardware (ROACH) board. They reported noise on the order of  $10^{-4} \text{rad}/\sqrt{\text{Hz}}$  as we can see in fig.5.25, proportional to the white noise we calculated.

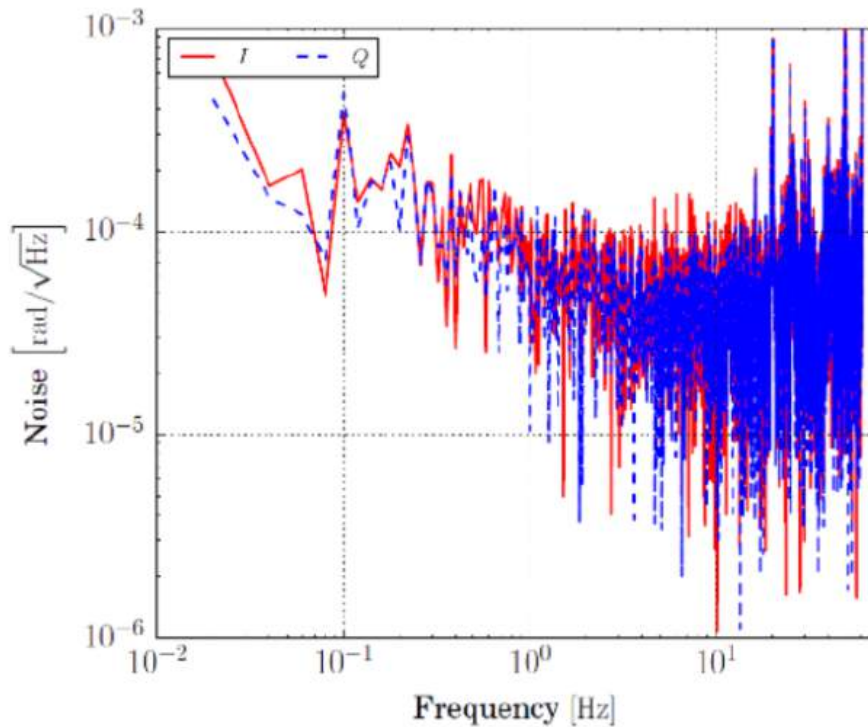


Figure 5.25: Noise calculated by the experiment OLIMPO

Other experiments used different methods to represent noise. In our case, we calculated an average white noise of  $10^{-20} \text{W}/\sqrt{\text{Hz}}$ . The Origins Space Telescope (origins) [47] will use a large array (about 10000 pixels) of KIDs, on which they have estimated a NEP of  $3 * 10^{-19} \text{W}/\sqrt{\text{Hz}}$  in the laboratory, as we can see in fig.5.26. We therefore have an order of magnitude lower, but given by the advantage of using a limited number of detectors.

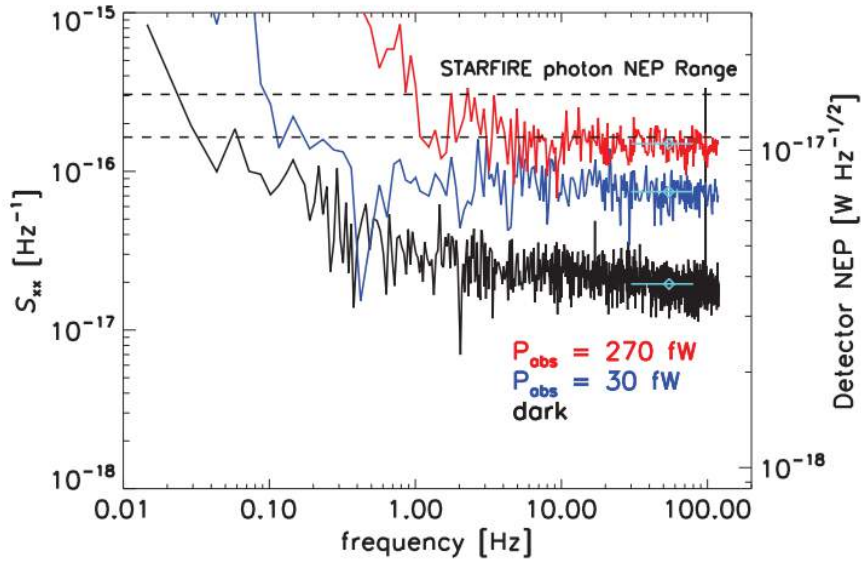


Figure 5.26: Noise calculated by the experiment Origins Space Telescope

Another study[48], aimed at testing the prototype of a 4x4 pixels camera using a demonstration instrument (“DemoCam”) showed white noise levels close to  $6 \times 10^{-16} W / \sqrt{Hz}$  as we can see in fig.5.27.

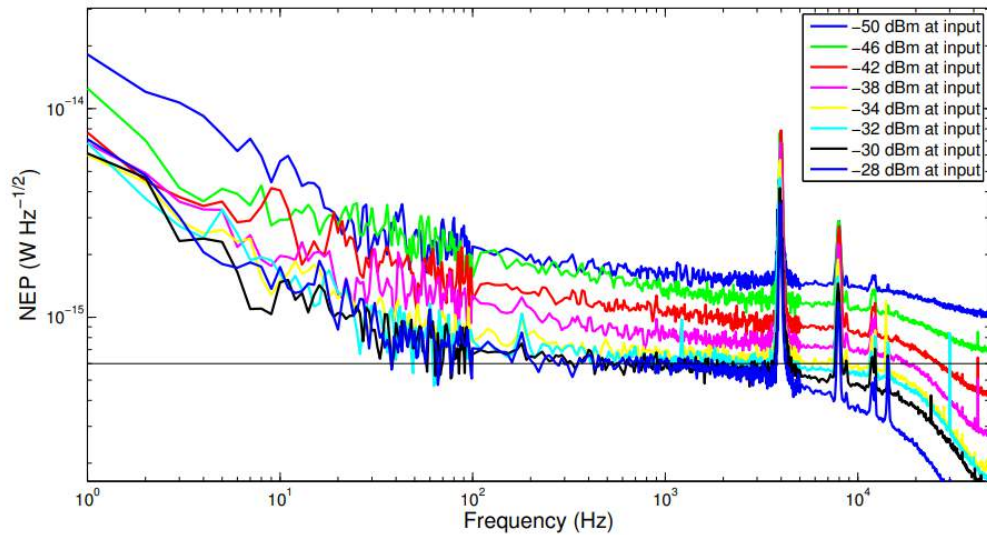


Figure 5.27: Noise calculated by the Demonstration Instrument “DemoCam” as a function of power, under 77 K load. The horizontal black line is drawn at  $6 \times 10^{-16} W / \sqrt{Hz}$  for a scale relationship.

## Conclusions

With this contribution we demonstrated that we can develop a working readout electronics for KIDs with a modular architecture based on commercial devices which are capable of a bandwidth of 100 MHz per module and a sampling rate (still not optimized) of about more than 12 kHz for 23 effective resonators plus 2 test tones. The main advantage of our readout electronics is the access to hardware and software solutions which greatly reduce the time required to realize a working readout chain and to develop a Graphical User Interface. The achieved sampling rate of  $\sim 12\text{kHz}$  is enough for COSMO to remove the atmospheric disturbances using the rotating mirror. The measurements made on the phase noise ensure consistency with the measurements made in the literature, allowing us to focus our attention on the software components of the project.

As the next step, we are planning to use a single FPGA with a transceiver with a RF bandwidth wider than the sum of the two implemented in this Set-Up. We think that using two FPGAs slowed down the performance, as they have to share a single data bus, and we can speed up the sampling rate just using a single FPGA. Finally, a complete NEP investigation will be performed on the COSMO KIDs. A second configuration as been developed and is under test to work with the multimode aluminium detector of COSMO. In fig.5.28 we can see the new scheme designed: the signal is generated by the FPGA to the transceiver NI-5782, a model with two analog output and input used to generate and receive the signal divided in the IQ components.

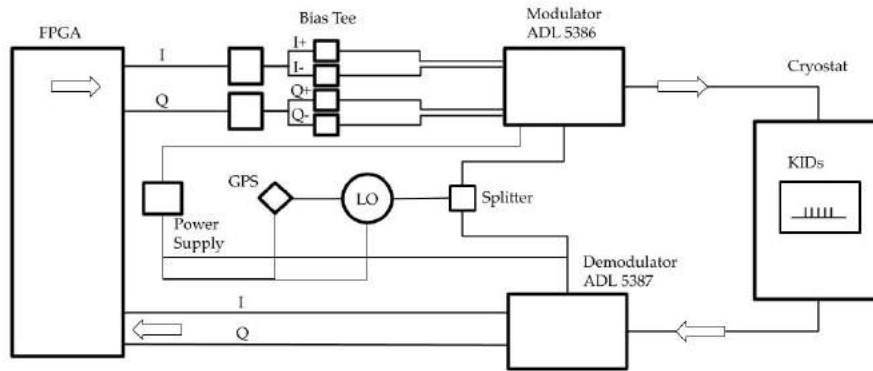


Figure 5.28: The configuration for the new electronic readout of COSMO

The I and Q signals generated by the FPGA are modulated by a modulator ADL5386<sup>1</sup> and up-converted with an external oscillator, a VALON 5009<sup>2</sup>. Similarly the demodulator ADL5387<sup>3</sup> splits the signal from the detectors into the two signals I and Q down-converted using the same local oscillator before being converted back into digital signals by the transceiver. The external oscillator, is connected to an external reference, the GPS Microchip GPS-2700<sup>4</sup>, to obtain even greater stability of the signal. Since the signals propagating through the modulator are balanced (I+ I-, Q+ Q-) two baluns (MINICIRCUITS ZFSCJ-2-1<sup>5</sup>) have been used to adapt the unbalanced propagation present at the transceiver's IO ports, phase-shifting the signal by 180°. The signal, before entering the modulator, is reduced in power by four appropriate bias tees (ZFBT-4R2GW-FT+<sup>6</sup>). This configuration of the readout electronics will be placed in an insulated rack, over a plate as seen in fig.5.29 to be able to be handled comfortably and protected from the extreme climatic conditions of the Concordia base in Antarctica.

<sup>1</sup><https://www.analog.com/media/en/technical-documentation/data-sheets/ADL5386.pdf>

<sup>2</sup>[https://valontechnology.com/5009users/Valon5009\\_opman.pdf](https://valontechnology.com/5009users/Valon5009_opman.pdf)

<sup>3</sup><https://www.analog.com/media/en/technical-documentation/data-sheets/ADL5387.pdf>

<sup>4</sup>[https://www.microsemi.com/document-portal/doc\\_download/133459-gps-2700-user-guide](https://www.microsemi.com/document-portal/doc_download/133459-gps-2700-user-guide)

<sup>5</sup><https://www.minicircuits.com/pdfs/ZFSCJ-2-1.pdf>

<sup>6</sup><https://www.minicircuits.com/pdfs/ZFBT-4R2GW-FT+.pdf>

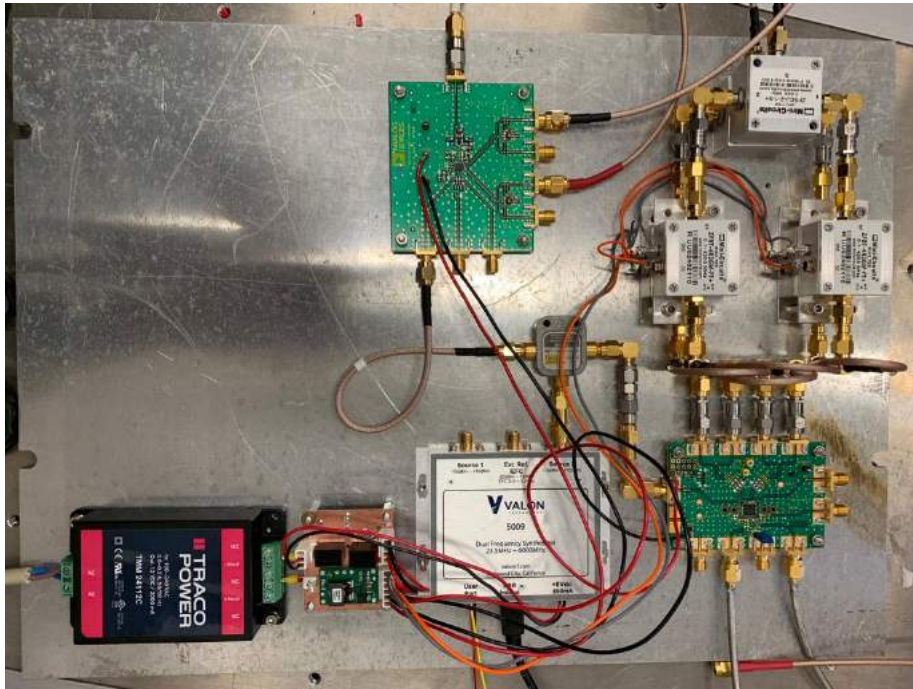


Figure 5.29: The new electronics placed on the plate for the insulated rack.

# Bibliography

- [1] Marc Lachièze-Rey and Jean-Pierre Luminet. “Cosmic topology”. In: *Physics Reports* 254.3 (1995), pp. 135–214. ISSN: 0370-1573. DOI: [https://doi.org/10.1016/0370-1573\(94\)00085-H](https://doi.org/10.1016/0370-1573(94)00085-H).
- [2] P. S. Wesson. “Olbers’ paradox in astronomy: history, nature and resolution”. In: *Science Progress (1933- )* 73.2 (290) (1989), pp. 133–146. ISSN: 00368504, 20477163.
- [3] Øyvind Grøn. “The Discovery of the Expansion of the Universe”. In: *Galaxies* 6.4 (Dec. 2018), p. 132. ISSN: 2075-4434. DOI: 10.3390/galaxies6040132.
- [4] Edwin Hubble. “A relation between distance and radial velocity among extra-galactic nebulae”. In: *Proceedings of the National Academy of Sciences* 15.3 (1929), pp. 168–173. DOI: 10.1073/pnas.15.3.168.
- [5] and N. Aghanim et al. “iPlanck/i2018 results”. In: *Astronomy & Astrophysics* 641 (Sept. 2020), A6. DOI: 10.1051/0004-6361/201833910.
- [6] A. A. Penzias and R. W. Wilson. *A Measurement of Excess Antenna Temperature at 4080 Mc/s*. Vol. 142. July 1965, pp. 419–421. DOI: 10.1086/148307.
- [7] R. H. Dicke et al. “Cosmic Black-Body Radiation.” In: *apj* 142 (July 1965), pp. 414–419. DOI: 10.1086/148306.
- [8] D. J. Fixsen. *THE TEMPERATURE OF THE COSMIC MICROWAVE BACKGROUND*. Vol. 707. 2009. DOI: 10.1088/0004-637X/707/2/916.
- [9] S. Masi et al. “The BOOMERanG experiment and the curvature of the universe”. In: *Progress in Particle and Nuclear Physics* 48.1 (Jan. 2002), pp. 243–261. DOI: 10.1016/s0146-6410(02)00131-x.
- [10] Eiichiro Komatsu et al. “Results from the Wilkinson Microwave Anisotropy Probe”. In: *Progress of Theoretical and Experimental Physics* 2014.6 (June 2014). ISSN: 2050-3911. DOI: 10.1093/ptep/ptu083.

- [11] Planck Collaboration et al. “Planck 2018 results - I. Overview and the cosmological legacy of Planck”. In: *A&A* 641 (2020), A1. DOI: 10.1051/0004-6361/201833880.
- [12] Erik M. Leitch et al. “Measuring polarization with DASI”. In: *Nature* 420 (2002), pp. 763–771. DOI: 10.1038/nature01271.
- [13] F. Acernese et al. “Virgo Detector Characterization and Data Quality: results from the O3 run”. In: (2022). DOI: 10.48550/ARXIV.2210.15633.
- [14] S. Dodelson et al. *The Origin of the Universe as Revealed Through the Polarization of the Cosmic Microwave Background*. 2009. DOI: 10.48550/ARXIV.0902.3796.
- [15] Jens Chluba. “Science with CMB spectral distortions”. In: *arXiv e-prints*, arXiv:1405.6938 (May 2014), arXiv:1405.6938.
- [16] Hiroyuki Tashiro. “CMB spectral distortions and energy release in the early universe”. In: *Progress of Theoretical and Experimental Physics* 2014.6 (June 2014). ISSN: 2050-3911. DOI: 10.1093/ptep/ptu066.
- [17] M. Gervasi et al. “TRIS. II. Search for CMB Spectral Distortions at 0.60, 0.82, and 2.5 GHz”. In: *The Astrophysical Journal* 688.1 (Nov. 2008), pp. 24–31. DOI: 10.1086/592134.
- [18] D. J. Fixsen et al. “The Cosmic Microwave Background Spectrum from the Full COBE FIRAS Data Set”. In: *apj* 473 (Dec. 1996), p. 576. DOI: 10.1086/178173.
- [19] J. Chluba et al. “New horizons in cosmology with spectral distortions of the cosmic microwave background”. In: *Experimental Astronomy* 51.3 (May 2021), pp. 1515–1554. DOI: 10.1007/s10686-021-09729-5.
- [20] Wayne Hu, Douglas Scott, and Joseph Silk. “Power spectrum constraints from spectral distortions in the cosmic microwave background”. In: *The Astrophysical Journal* 430 (July 1994), p. L5. DOI: 10.1086/187424.

- [21] R. A. Sunyaev and Ya. B. Zeldovich. “Small-scale fluctuations of relic radiation”. In: *Astrophysics and Space Science* 7.1 (Apr. 1, 1970), pp. 3–19. ISSN: 1572-946X. DOI: 10.1007/BF00653471.
- [22] Ya. B. Zeldovich and R. A. Sunyaev. “The Interaction of Matter and Radiation in a Hot-Model Universe”. In: *apss* 4.3 (July 1969), pp. 301–316. DOI: 10.1007/BF00661821.
- [23] Tetsu Kitayama. “Cosmological and astrophysical implications of the Sunyaev–Zel’dovich effect”. In: *Progress of Theoretical and Experimental Physics* 2014.6 (June 2014). ISSN: 2050-3911. DOI: 10.1093/ptep/ptu055.
- [24] S. Doyle et al. “Lumped Element Kinetic Inductance Detectors”. In: *Proceedings of the Eighteenth International Symposium on Space Terahertz Technology 2007, ISSTT 2007* 151 (Apr. 2008), pp. 530–536. DOI: 10.1007/s10909-007-9685-2.
- [25] S. Masi et al. *The COSmic Monopole Observer (COSMO)*. 2021. DOI: 10.48550/ARXIV.2110.12254.
- [26] D.H. Martin and E. Puplett. “Polarised interferometric spectrometry for the millimetre and submillimetre spectrum”. In: *Infrared Physics* 10.2 (1970), pp. 105–109. ISSN: 0020-0891. DOI: [https://doi.org/10.1016/0020-0891\(70\)90006-0](https://doi.org/10.1016/0020-0891(70)90006-0).
- [27] E. S. Battistelli et al. “QUBIC: The Q & U Bolometric Interferometer for Cosmology”. In: *Journal of Low Temperature Physics* 199.1-2 (Feb. 2020), pp. 482–490. DOI: 10.1007/s10909-020-02370-0.
- [28] L. Mele et al. “Measuring CMB Spectral Distortions from Antarctica with COSMO: Blackbody Calibrator Design and Performance Forecast”. In: *Journal of Low Temperature Physics* 209.5-6 (Dec. 2022), pp. 912–918. DOI: 10.1007/s10909-022-02874-x.
- [29] H. Kamerlingh Onnes. “The liquefaction of helium.” In: *Through Measurement to Knowledge: The Selected Papers of Heike Kamerlingh Onnes 1853–1926*. Ed. by

- Kostas Gavroglu and Yorgos Goudaroulis. Dordrecht: Springer Netherlands, 1991, pp. 164–187. ISBN: 978-94-009-2079-8. DOI: 10.1007/978-94-009-2079-8\_7.
- [30] Leon N. Cooper. “Bound Electron Pairs in a Degenerate Fermi Gas”. In: *Phys. Rev.* 104 (4 Nov. 1956), pp. 1189–1190. DOI: 10.1103/PhysRev.104.1189.
- [31] D. C. Mattis and J. Bardeen. “Theory of the Anomalous Skin Effect in Normal and Superconducting Metals”. In: *Phys. Rev.* 111 (2 July 1958), pp. 412–417. DOI: 10.1103/PhysRev.111.412.
- [32] J. Bardeen, L. N. Cooper, and J. R. Schrieffer. “Microscopic Theory of Superconductivity”. In: *Phys. Rev.* 106 (1 Apr. 1957), pp. 162–164. DOI: 10.1103/PhysRev.106.162.
- [33] F. London, H. London, and Frederick Alexander Lindemann. “The electromagnetic equations of the supraconductor”. In: *Proceedings of the Royal Society of London. Series A - Mathematical and Physical Sciences* 149.866 (1935), pp. 71–88. DOI: 10.1098/rspa.1935.0048.
- [34] W. Meissner and R. Ochsenfeld. “Ein neuer Effekt bei Eintritt der Supraleitfähigkeit”. In: *Naturwissenschaften* 21.44 (Nov. 1933), pp. 787–788. DOI: 10.1007/BF01504252.
- [35] Carlos Villarreal and Santiago F. Caballero-Benitez. “Casimir forces and high- $T_c$  superconductors”. In: *Phys. Rev. A* 100 (4 Oct. 2019), p. 042504. DOI: 10.1103/PhysRevA.100.042504.
- [36] D.M. Sheen et al. “Current distribution, resistance, and inductance for superconducting strip transmission lines”. In: *IEEE Transactions on Applied Superconductivity* 1.2 (1991), pp. 108–115. DOI: 10.1109/77.84617.
- [37] R. Meservey and P. M. Tedrow. “Measurements of the Kinetic Inductance of Superconducting Linear Structures”. In: *Journal of Applied Physics* 40.5 (1969), pp. 2028–2034. DOI: 10.1063/1.1657905.

- [38] S. B. Kaplan et al. “Quasiparticle and phonon lifetimes in superconductors”. In: *Phys. Rev. B* 14 (11 Dec. 1976), pp. 4854–4873. DOI: 10.1103/PhysRevB.14.4854.
- [39] D.A. Frickey. “Conversions between S, Z, Y, H, ABCD, and T parameters which are valid for complex source and load impedances”. In: *IEEE Transactions on Microwave Theory and Techniques* 42.2 (1994), pp. 205–211. DOI: 10.1109/22.275248.
- [40] Marianina Calvo et al. “Development of Kinetic Inductance Detectors for Cosmic Microwave Background experiments”. In: *Experimental Astronomy* 28 (Dec. 2010), pp. 185–194. DOI: 10.1007/s10686-010-9197-y.
- [41] A. B. Pippard. “An Experimental and Theoretical Study of the Relation between Magnetic Field and Current in a Superconductor”. In: *Proceedings of the Royal Society of London. Series A, Mathematical and Physical Sciences* 216.1127 (1953), pp. 547–568. ISSN: 00804630. (Visited on 01/09/2023).
- [42] J. Volder. “The CORDIC Computing Technique”. In: *Managing Requirements Knowledge, International Workshop on*. Vol. 1. Los Alamitos, CA, USA: IEEE Computer Society, Mar. 1959, p. 257. DOI: 10.1109/AFIPS.1959.57.
- [43] Sean McHugh et al. “A readout for large arrays of microwave kinetic inductance detectors”. In: *Review of Scientific Instruments* 83.4 (2012), p. 044702. DOI: 10.1063/1.3700812.
- [44] F.J. Harris. “On the use of windows for harmonic analysis with the discrete Fourier transform”. In: *Proceedings of the IEEE* 66.1 (1978), pp. 51–83. DOI: 10.1109/PROC.1978.10837.
- [45] A Abinaya and M Maheswari. “A survey of digital down converter architecture for next generation wireless applications”. In: *IOP Conference Series: Materials Science and Engineering* 872.1 (June 2020), p. 012037. DOI: 10.1088/1757-899X/872/1/012037.

- [46] G Presta et al. “The first flight of the OLIMPO experiment: instrument performance”. In: *Journal of Physics: Conference Series* 1548.1 (May 2020), p. 012018. DOI: 10.1088/1742-6596/1548/1/012018.
- [47] Steven Hailey-Dunsheath et al. “Kinetic inductance detectors for the Origins Space Telescope”. In: *Journal of Astronomical Telescopes, Instruments, and Systems* 7.1 (2021), p. 011015. DOI: 10.1117/1.JATIS.7.1.011015. URL: <https://doi.org/10.1117/1.JATIS.7.1.011015>.
- [48] James A. Schlaerth. “Microwave kinetic inductance detector camera development for millimeter-wave astrophysics”. PhD thesis. University of Colorado, Boulder, Jan. 2010.

## A new readout electronics for Kinetic Inductance Detectors

A. Limonta<sup>1,2</sup> · M. Zannoni<sup>1,2</sup> · G. Coppi<sup>1,2</sup> ·  
G. Conenna<sup>1</sup> · F. Boussaha<sup>3</sup> · A. Tartari<sup>4,5</sup> ·  
M. Gervasi<sup>1,2</sup> · F. Nati<sup>1,2</sup> · A. Passerini<sup>1,2</sup> ·  
P. de Bernardis<sup>6,7</sup> · A. Coppolecchia<sup>6,7</sup> · G.  
D'Alessandro<sup>6,7</sup> · S. Masi<sup>6,7</sup> · A. Paiella<sup>6,7</sup> · M.  
Bersanelli<sup>8,9</sup> · C. Franceschet<sup>8,9</sup> · E. Manzan<sup>8</sup> · A.  
Mennella<sup>8,9</sup>

the date of receipt and acceptance should be inserted later

**Abstract** With this contribution we show the readout electronics for Kinetic Inductance Detectors (KIDs) that we are developing based on a commercial IQ transceivers from National Instruments and using a Virtex 5 class FPGA. It will be the readout electronics of the COSMO (COSmic Monopole Observer) experiment, a ground based cryogenic Martin-Puplett Interferometer searching for the Cosmic Microwave Background (CMB) spectral distortions. The readout electronics require a sampling rate in the range of tens of kHz, which is both due to a fast rotating mirror modulating the signal and the time constant of the COSMO KIDs. In this contribution we show the capabilities of our readout electronics using Niobium KIDs developed by Paris Observatory for our 5 K cryogenic system. In particular, we demonstrate the capability to detect 23 resonators from frequency sweeps and to readout the state of each resonator with a sampling rate of about 8 KHz. The readout is based on a finite-state machine where the first two states look for the resonances and generate the comb of tones, while the third one performs the acquisition of phase and amplitude of each detector in free running. Our electronics are based on commercial modules, which brings two key advantages: they can be acquired easily and it is relative simple to write and modify the firmware within the LabView environment in order to meet the needs of the experiment.

**Keywords** KIDS • Electronic Readout • CMB

### 1 Introduction to COSMO experiment

COSMO (COSmic Monopole Observer)<sup>1</sup> is a ground based cryogenic Martin-Puplett Interferometer to be operated in Dome-C, Antarctica, aiming at measuring the isotropic y-distortions of the Cosmic Microwave Background (CMB)<sup>2</sup>. Such distortions are produced by physical processes commonly referred to as the thermal Sunyaev-Zeldovich (SZ) effect, arising from energy exchange between CMB photons and hot electrons along the thermal history of the Universe. However, to date, no isotropic spectral distortions have been

1 Università di Milano Bicocca, Milano, Italy · 2 INFN sezione di Milano – Bicocca, 20126 Milano, Italy · 3 Observatoire de Paris, 92195 Meudon, France · 4 Università di Pisa, Pisa, Italy · 5 INFN Sezione di Pisa, 56127 Pisa, Italy · 6 Università di Roma – La Sapienza, Roma, Italy · 7 INFN Sezione di Roma, 00185 Roma, Italy · 8 Università degli studi di Milano, Milano, Italy · 9 INFN Sezione di Milano, 20133 Milano, Italy  
E-mail: a.limonta12@campus.unimib.it

detected at mm wavelengths, and the upper limit is  $\sim 10^{-5}$ , as placed by COBE-FIRAS (1990)<sup>3</sup> and then confirmed by other experiments, e.i. the TRIS experiment<sup>4</sup>.

COSMO exploits a cryogenic differential Fourier Transform Spectrometer (FTS) to measure the spectral brightness of the sky in two frequency bands, the low frequency channel at 120-180 GHz and the high frequency channel at 210-300 GHz. The instrument will measure the difference in brightness between the radiation coming from the sky and the radiation coming from the internal cryogenic reference blackbody. An ambient temperature spinning wedge mirror allows for fast sky modulation (2400 rpm expected) to remove the atmospheric emission and its fluctuations. There will be two focal planes equipped by 9 pixels for each array of multi-mode Kinetic Inductance Detectors (KIDs)<sup>5,6</sup>, which are designed to have a time constant of about  $\tau = 60\mu s$ . This time constant value requires a fast readout electronics: indeed the frequency noise of the detectors goes up to their maximum frequency, in the order of  $3/\tau$ . For this reason, together with the fast scanning mirror we need a fast readout electronics of about 60 KHz.

## 2 Readout Electronics

The system is based on a commercial bus architecture (PXI) developed by National Instruments. It is composed of two FPGAs Xilinx Virtex-5 NI7966R<sup>†</sup>, on PXI express bus operating two transceivers NI5791<sup>‡</sup>. Two transceivers are used along with power combiners to double the RF bandwidth. (see Fig. 1). The signal is digitally generated in the I-Q

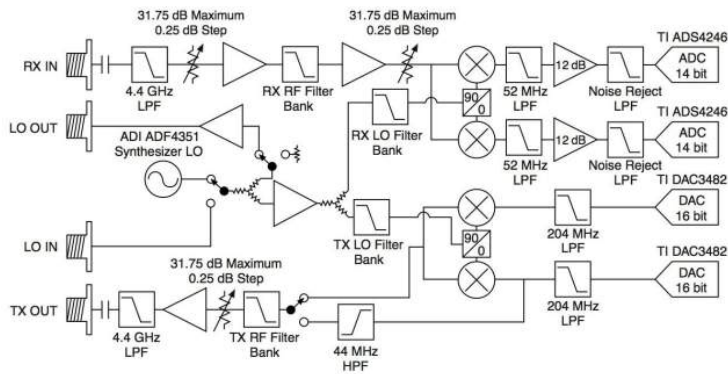


Fig. 1: Architecture of NI 5791 (picture taken from the NI data sheet).

domain by the two FPGAs and converted to analogue by the four Digital to Analog Converters (DACs) inside the transceivers. The two RF signals are added together by a Wilkinson power divider, attenuated by a programmable attenuator (PXI-5695), and fed into the cryostat. Stainless Steel and Niobium coaxial cables are used inside the cryostat to reduce thermal loading. The signal emerging from the KIDs is divided by another Wilkinson power divider, fed into the two transceivers' inputs and I-Q detected. A schematic drawing of our

<sup>†</sup><https://www.ni.com/pdf/manuals/373047b.pdf>

<sup>‡</sup><https://www.ni.com/pdf/manuals/373845d.pdf>

readout is in Fig. 2.

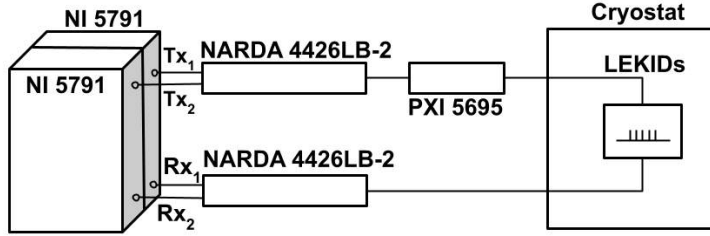


Fig. 2: Block-diagram of our readout based on two NI transceivers (model 5791). The two outputs are added by a Wilkinson power divider (Narda 4426LB-2). After that, the sum signal is attenuated by a programmable variable attenuator (PXI-5695) to adjust the power level. The comb signal enters the cryostat by means of a vacuum feedthrough and a sequence of a Stainless Steel coaxial cable and a Nb coaxial cable to minimize the heat load. The same kind of cables are used to reach a second feedthrough. With this set-up there is no need for a LNA. The signals coming out of the cryostat are split with a second Wilkinson power divider before being fed into the two transceivers.

Our readout electronics operate as a finite state machine that works in three states. In the first state our algorithm performs a sweep to find the resonant tones of the KIDs. The sweep is made using an up-chirp signal varying the frequency over time. In the second state each resonant tones are generated by a COordinate Rotation DIgital Computer algorithm (CORDIC)<sup>7</sup>, then added together to form a comb, which is acquired only once and thus it is saved in a look-up table. In the end, during the third state the signal is transmitted. We acquire I and Q signals so that we can easily evaluate the amplitude and phase in order to measure the variation of the working point of the KIDs. Each KID resonance frequency is evaluated by means of a Direct Down Converter (DDC) algorithm. This is the same approach used for the first time in the NIKA experiment<sup>8</sup>. This method was preferred to the poly-phase filter banks approach<sup>9</sup> because it is more computationally efficient and requires fewer resources with our small number of detectors.

We implemented a Graphical User Interface (GUI) using a LabView environment. Two examples of its functionalities are shown in Fig. 3 and Fig. 4. The presence of a GUI allows the user to monitor status and set FPGA parameters easily without modifying the software at lower levels. In addition, a real time plot of the amplitude helps to have a visual feedback during the first and the third state of the machine. It is also possible to manually set the comb frequencies, or to select peaks found during a sweep corresponding to resonator frequencies. The GUI also greatly simplifies the tuning of the input signal parameters such as the trigger, the output power or the number of samples to be used.

In both Fig. 3 and Fig. 4 it is possible to see the 23 tones that we detect. We added a test tone for each FPGA, the frequency for the first one is 1.9030 GHz, and for the second one is 1.9760 GHz. Thus, we can receive and transmit 25 tones in total. We chose these values because at these frequencies the signal is not attenuated by any other close resonance. The presence of the test tones allows us to check the behaviour of the resonant tones and to have an estimation of the noise.

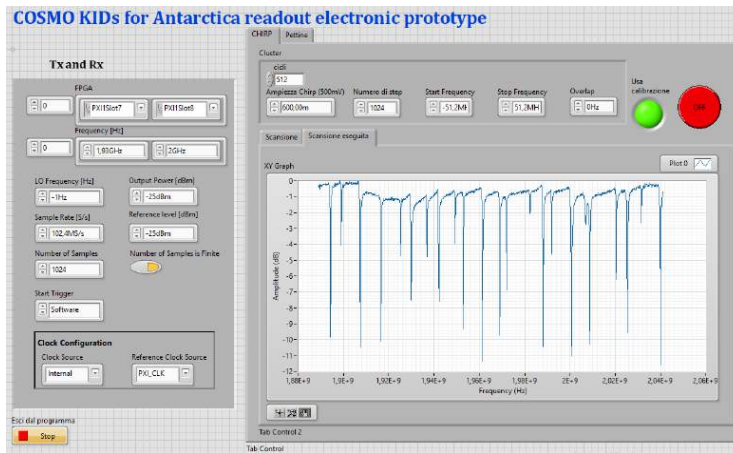
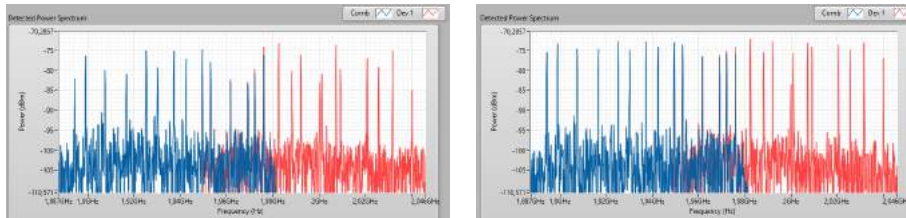


Fig. 3: An example of the functionalities of our GUI, which is made to interactively control the readout electronics. The FPGA parameters can be set in the left box, while in the right one we can visualize the real time plot of the first (here), and third (see Fig. 4) state of the machine. We can also set the parameters of the state.



(a) KIDs response while the base temperature is at its lowest level.

(b) KIDs response while the base temperature is at its highest level.

Fig. 4: An example of the functionalities of our GUI, showing the comb signal (third state). The signal is depicted by using two colors, representing the two transceivers. We reported two different time instants in order to appreciate the amplitude variation with respect to the temperature oscillations (lowest level on the left, highest level on the right).

### 3 Test results

We use Niobium KIDs (designed at AstroParticule et Cosmologie in Paris and manufactured at Paris Observatory) to test our electronics with real devices. The transition temperature of these KIDs is around 9 K and their measured quality factors are higher than 5000 at 4.9 K. This is the working temperature of our cryostat maintained by an RDK-408 SHI GM cryocooler under the set-up heat load. The Q factor could be higher but, for the purpose of this study, it was enough to have well defined resonances with a frequency spacing around 5-10 MHz so we adopted this device that was optimised for other studies. However, the COSMO detectors will be made by Aluminum to be compliant with the frequency coverage of the experiment<sup>10</sup> and they will work in the 0.3 K COSMO cryostat.

To date, we can reach a sampling rate of around 8 kHz on the 25 frequencies (23 effective resonances plus two test tones) saving in HDF5 format. We are still a factor of 8 far from

the COSMO requirements (18 detectors sampled at 60 kHz). To increase the sampling frequency we plan to improve the data saving with binary compressed format and to move the calculation of the amplitude and phase shift of each tone to the FPGA.

Due to the intrinsic mechanical oscillations of the cooler, the temperature has a fluctuations of  $\sim 20$  mK with a frequency  $\sim 1$  Hz, typical of the cooler. The temperature oscillations make the initial search for resonators difficult and for this reason we repeat the sweep multiple times. Indeed, in this way we can map the oscillations of the resonances and find the minimum transmission. This state corresponds to the minimum temperature achieved by the cryocooler with the installed set-up and consequentially gives the information about the tone of each resonance. Moreover, we can test some key parameters of the readout system with these oscillations. In fact, we use the temperature oscillations to verify that the system can track the tones during testing phase. Their presence is also a prominent feature that should be clearly visible in the phase time stream plot (Fig. 5) and can be used to evaluate the quality of our analysis.

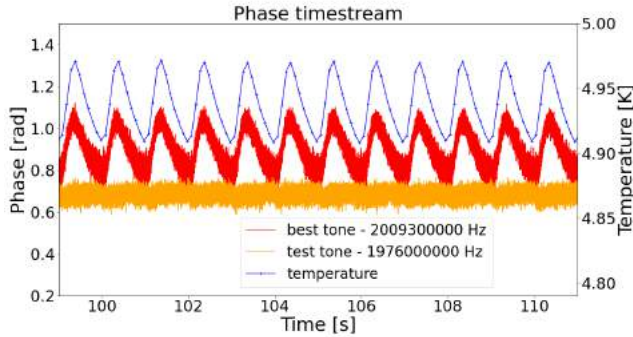


Fig. 5: Chunk of the phase timestream. The test tone (frequency 1.976 GHz) is depicted in orange, the resonant tone (2.00930 GHz) is in red and the temperature oscillations are in blue.

In figure Fig. 5 we present a chunk of the phase time stream. We decided to show only the tone at resonant frequency 2.00930 GHz because it is one of the deepest (-11.264 dB), but we have obtained similar wave-forms for the other frequency tones. In the same plot we report the temperature fluctuations and we can notice a sync between this signal and the phase timestream. This evidence confirms that the KID responds correctly with respect to the variation of the quasi-particles density. On the contrary, we can also see the behaviour of the test tone (frequency 1.976 GHz), which is not affected by the change of temperature, as expected.

By repeating the comparison between the test tone (1.976 GHz) and one resonant tone (2.00930 GHz), we analyzed different kinds of noise: the phase and IQ noise [ $\sqrt{I_{noise}^2 + Q_{noise}^2}$ ] of KIDs signal (Fig. 6), the noise arising from the cold loop back signal (Fig. 7) and the noise arising from the warm loop back signal (Fig. 8). With cold loop back we mean the signal passing through everything inside the cryostat, except the array of KIDS, while the warm loop back is the signal without passing through the cryostat.

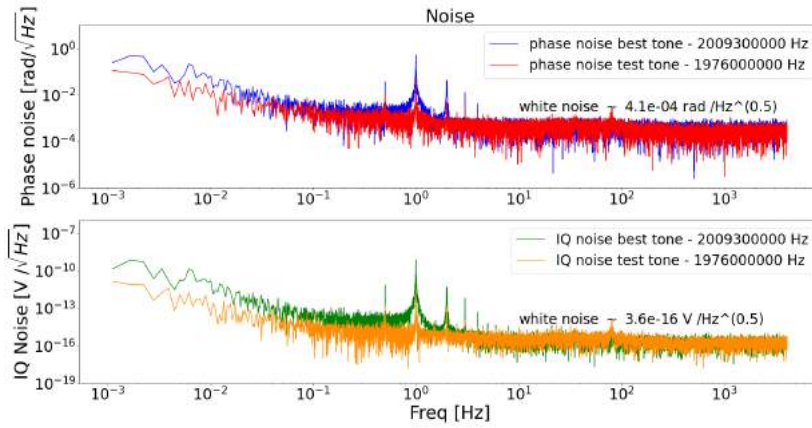


Fig. 6: Data noise. Upper plot: the phase noise of the best tone is plotted in blue, the one of the test tone is in red. Lower part: the noise of the IQ signal of the best tone is depicted in green, the one of the test tone is in orange.

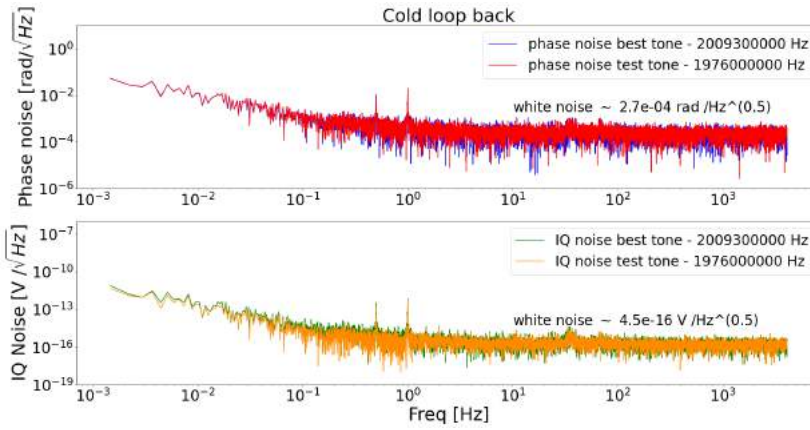


Fig. 7: Cold noise (loop back). Upper plot: the phase cold loop back of the best tone is plotted in blue, the one of the test tone is in red. Lower part: the cold loop back of the IQ signal of the best tone is depicted in green, the one of the test tone is in orange.

In Fig. 6 the phase noise is shown in the upper part: as expected the resonant tone (2.00930 GHz) is higher than the test tone. Thus also the white noise level is higher compared to the test tone one. In addition, we can notice the presence of the 1 Hz peak also in the test tone. Indeed, as we can see in the cold loop back signal (in Fig. 7 - upper part), the resonant tone and the test tone are very comparable and the 1 Hz peak is due to the presence of the Nb cables which transmission is slightly modulated by the temperature. Concerning the cold noise (without the presence of the KIDs) in Fig. 7, the white noise is lower compared to Fig. 6 since the signal is not attenuated by any resonant frequencies. The same consideration applies also looking at the warm loop back noise in Fig. 8. Looking at IQ signals, the noise is in Fig. 6 - lower part, while the cold loop back and the warm loop back are in Fig. 7 -

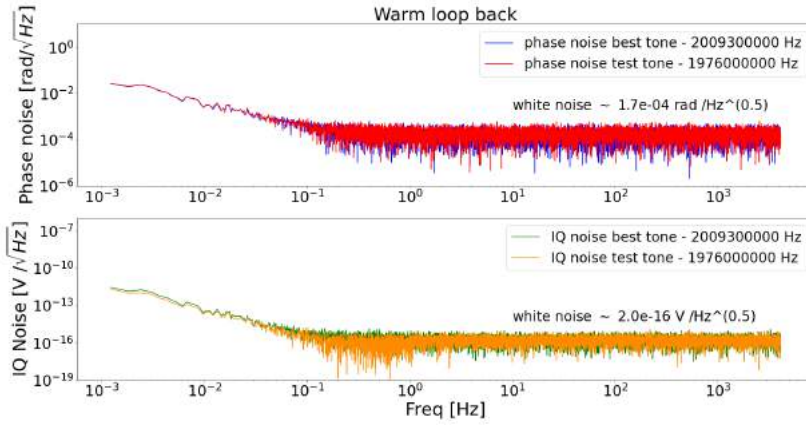


Fig. 8: Warm noise (loop back). Upper plot: the phase warm loop back of the best tone is plotted in blue, the one of the test tone is in red. Lower part: the warm loop back of the IQ signal of the best tone is depicted in green, the one of the test tone is in orange.

lower part and Fig. 8 - lower part. The same considerations about the white noise applies here, with the exception of the cold loop back noise.

All the data were collected for about 30 minutes so that it is possible appreciate also the  $1/f$  noise (on the right part of the plots). All the plots end at frequency of about 4 KHz, and thus our sampling rate is around 8 KHz.

#### 4 Conclusion and Next Step

This contribution demonstrates that we can develop a working readout electronics for KIDs with a modular architecture using commercial devices which are capable of a bandwidth of 100 MHz per module and a sampling rate (still not optimized) of about more than 8 kHz for 23 effective resonators plus two test tones. The main advantage of our readout electronics is the access to hardware and software solutions which greatly reduce the time needed to achieve a working readout chain and to develop a Graphical User Interface.

In the future, we are planning to use a single FPGA with a transceiver with a RF bandwidth wider than the sum of the two employed in this experiment. We also think that using a single FPGA could speed-up the sample rate because we will avoid the sharing of the data bus.

Finally, a complete NEP investigation will be performed on each single component (especially on the COSMO KIDs) in order to achieve better NEP performance. Indeed in the current version of our readout we are not using a LNA and thus the estimation of the noise can be overestimated.

**Acknowledgements** These activities were partially funded by the Italian Space Agency contracts 2016-19-H.0 and 2017-42-H.0. G. Coppi is supported by the European Research Council under the Marie Skłodowska Curie actions through the Individual European Fellowship No. 892174 PROTOCALC. G. Conenna is supported by PRIN-MIUR 2017 COSMO.

---

**References**

1. L. Mele *et al.*, *J. Low Temp. Phys.* **this special Issue** (2021)
2. Penzias, A. A. and Wilson, R. W., *A Measurement of Excess Antenna Temperature at 4080 Mc/s.*, *ApJ*, 1965,142, 419-421, DOI:10.1086/148307
3. D.J. Fixen *et al.*, *ApJ* **473**, 576, (1996), DOI: 10.1086/178173
4. M. Zannoni *et al.* *ApJ* **668**, 12-23, (2008), DOI: 10.1086/592133
5. Mazin, B. A., Day, P. K., Zmuidzinas, J., *et al.* 2002, *Low Temperature Detectors*, 605, 309. doi:10.1063/1.1457652
6. P. Day *et al.* *Nature* **425**, 817-821, (2003), DOI: 10.1038/nature02037
7. J. Volder *et al.*, *IRE Transactions on Electronic Computers* **8**, 330-334, (1959), DOI: 10.1109/TEC.1959.5222693
8. O. Bourrion *et al.*, *JINST* **6**, P06012, (2011), DOI: 10.1088/1748-0221/6/06/P06012
9. S. McHugh *et al.*, *Review of Scientific Instruments* **83**, 044702, (2012), DOI: 10.1063/1.3700812
10. A. Paiella *et al.* *J. Low Temp. Phys.* **184**, 97–102, (2016), DOI: 10.1007/s10909-015-1470-z



# Readout Electronics for Kinetic Inductance Detectors for COSMO

G. Conenna<sup>1</sup>, A. Limonta<sup>1,2</sup>, M. Zannoni<sup>1,2</sup>, G. Coppi<sup>1,2</sup>, F. Boussaha<sup>3</sup>, A. Tartari<sup>4,5</sup>, M. Gervasi<sup>1,2</sup>, F. Nati<sup>1,2</sup>, A. Passerini<sup>1,2</sup>, P. de Bernardis<sup>6,7</sup>, A. Coppolecchia<sup>6,7</sup>, G. D'Alessandro<sup>6,7</sup>, S. Masi<sup>6,7</sup>, A. Paiella<sup>6,7</sup>, M. Bersanelli<sup>8,9</sup>, C. Franceschet<sup>8,9</sup>, E. Manzan<sup>8</sup>, and A. Mennella<sup>8,9</sup>

<sup>1</sup>Università di Milano Bicocca, Milano, Italy

<sup>2</sup>INFN sezione di Milano - Bicocca, 20126 Milano, Italy

<sup>3</sup>Observatoire de Paris, 92195 Meudon, France

<sup>4</sup>Università di Pisa, Pisa, Italy

<sup>5</sup>INFN Sezione di Pisa, 56127 Pisa, Italy

<sup>6</sup>Università di Roma - La Sapienza, Roma, Italy

<sup>7</sup>INFN Sezione di Roma, 00185 Roma, Italy

<sup>8</sup>Università degli studi di Milano, Milano, Italy

<sup>9</sup>INFN Sezione di Milano, 20133 Milano, Italy

## ABSTRACT

We describe the readout electronics for Kinetic Inductance Detectors (KIDs) that we are developing based on a commercial IQ transceivers from National Instruments and using a Virtex 5 class FPGA. It will be the readout electronics of the COSmic Monopole Observer (COSMO) experiment, a ground based cryogenic Martin-Puplett Interferometer searching for the Cosmic Microwave Background spectral  $y$ -distortions. The COSMO readout electronics requires a sampling rate in the range of tens of kHz, due to both a fast modulation of the signal with a spinning optical element and the short time constant of the Kinetic Inductance Detectors (KIDs) used in COSMO. In this contribution we show the capabilities of our readout electronics using Niobium KIDs developed by Paris Observatory for our 5 K cryogenic system. In particular, we demonstrate the capability to detect 23 resonators from frequency sweeps and to readout the state of each resonator with a sampling rate at about 12 kHz.

**Keywords:** KIDs, electronic readout, CMB,  $y$ -distortions

## 1. INTRODUCTION

Since its revolutionary first detection made by A. Penzias and R. Wilson working at Bell Labs,<sup>1</sup> it has been clear that the Cosmic Microwave Background (CMB) had the potential to transform our understanding of the Universe by providing crucial information about its origin, evolution and composition.

After many decades of measurements, CMB is now providing key results, in the so-called precision cosmology era. To date, two crucial aspects of our  $\Lambda$ CDM model related to CMB are still not detected: the power spectrum of the B-mode<sup>2</sup> originated from primordial tensor perturbations, and the spectral distortions. The former, which requires polarization sensitive instruments, is considered the smoking-gun of cosmological inflation. In the following we focus on the latter.

In the early Universe (redshift  $z \geq 2 \times 10^6$ ), processes such as Compton scattering, bremsstrahlung and double Compton scattering maintain a strict blackbody spectrum of the CMB. On the contrary, in more recent epoch ( $z < 10^6$ ) these interactions become less efficient due to the expansion of the Universe, and thermalization becomes

---

Further author information:

G. Conenna: g.conenna1@campus.unimib.it

A. Limonta: a.limonta12@campus.unimib.it

inefficient. As a result, CMB spectral distortions are created by processes that drive matter and radiation out of thermal equilibrium.

It is possible to distinguish two types of CMB distortions with respect to the epoch of the energy release:  $\mu$ -type and  $y$ -type distortions. The former are characterized by a frequency-dependent chemical potential, and are created between the double Compton scattering decoupling ( $z \sim 10^6$ ) and the thermalization decoupling by Compton scattering ( $z \sim 10^5$ ). Thus they cannot be generated at recent epochs and for this reason directly probe events in the pre-recombination era. The latter are produced after the thermalization decoupling by Compton scattering, when it became inefficient. The  $y$ -distortions, on the other hand, can probe the thermal history during recombination and reionization.

Therefore, a measurement of spectral distortions of the CMB is a powerful tool for investigating the thermal history of the Universe.

One of the major physical process generating spectral distortions is the Compton scattering, that couples matter and radiation, and it also has observable consequences in low-energy environments, where small energy transfers occur. Indeed, the Sunyaev-Zel'dovich effect,<sup>3</sup> arising from the scattering of the CMB radiation field with electrons in clusters of galaxies, is used to measure the properties of the intracluster gas, and it is considered a means of measuring the motions of clusters of galaxies and hence of studying the evolution of the structures in the Universe.

On the experimental side, a very strong upper limit was placed by COBE/FIRAS,<sup>4</sup> that did not observed CMB distortions within its sensitivity, proving constrains on the order of

$$y < 1.5 \times 10^{-5} \quad (1)$$

$$|\mu| < 9.0 \times 10^{-5} \quad (2)$$

at 95% confidence level.

More recently, other experiments in the low frequency range, such as TRIS<sup>5</sup> and ARCADE,<sup>6</sup> contributed additional upper limits.

COSMO<sup>7</sup> is a ground-based cryogenic Martin-Puplett Interferometer aiming at the detection of the isotropic  $y$ -distortions of the CMB. It will be placed at Dome-C, in the high Antarctic plateau. COSMO exploits a cryogenic differential Fourier Transform Spectrometer (FTS) to measure the spectral brightness of the sky in two frequency bands, the low frequency channel at 120-180 GHz and the high frequency channel at 210-300 GHz. The instrument has two input ports and it is intrinsically differential, measuring the difference in brightness between the radiation coming from the sky and the radiation coming from the internal, cryogenic, reference blackbody. For calibration purposes only, a second blackbody with a temperature different from the internal one, replaces the sky on the sky port. An ambient temperature spinning wedge mirror allows for fast sky modulation (2400 rpm expected) to remove the atmospheric emission and its fluctuations. Alternative optical techniques for fast sky modulation are also under study. There will be two focal planes equipped by 9 pixels for each array of multi-mode KIDs,<sup>8</sup> which are designed to have a time constant of about  $\tau = 60\mu s$ . This time constant value requires a fast readout electronics: indeed the frequency noise of the detectors goes up to their maximum frequency, in the order of  $3/\tau$ . For this reason, together with the fast scanning mirror we need a fast readout electronics at about 60 kHz.

KIDs are superconducting photon detector working at cryogenic temperatures. KIDs measure the change in quasi-particle population within the volume of a superconducting film upon photon absorption. Indeed, if a photon with energy  $h\nu > 2\Delta$  (where  $\Delta$  is the superconducting gap energy) is absorbed in a superconducting film cooled to a temperature  $T \ll T_c$ , it breaks the Cooper pairs and a number  $N_{qp} = \eta h\nu/\Delta$  of quasiparticle excitations is created (where  $\eta < 1$  is the efficiency of quasiparticles creation). When the number density of quasiparticles  $n_{qp}$  increases, the surface impedance  $Z_S = R_S + i\omega L_S$  of the film changes as  $\frac{\delta Z_S}{Z_S} \approx \frac{\delta n_{qp}}{2N_0\Delta}$  with  $N_0$  the number of quasiparticles which did not absorb photons. The film is part of a resonant microwave LC circuit shunting a feedline at and near its resonance frequency. The effect of: the effect of the surface inductance  $L_S$  is to increase the total inductance  $L$ , while  $R_S$  makes the inductor slightly lossy. Thus, when a photon arrives, are generated and increase both  $L_S$  and  $R_S$ .  $L_S$  moves the resonance to lower frequency, while  $R_S$  makes the dip broader and shallower. They both contribute to changing the amplitude and phase of a microwave probe signal

transmitted past the circuit.

The most relevant advantage of using KIDs is that high multiplexing factors can be reached, allowing up to thousands of resonators to be read out through a single coaxial cable and a single low noise, wide bandwidth cryogenic amplifier.

## 2. READOUT ELECTRONICS

We use a system based on a commercial bus architecture (PXI) made by National Instrument: two FPGAs Xilinx Virtex-5 NI7966R<sup>†</sup> and two transceivers NI5791<sup>‡</sup> are operation on PXI express bus. We use two transceivers along with power combiners in order to double the RF bandwidth (see Fig. 1). A schematic drawing of our

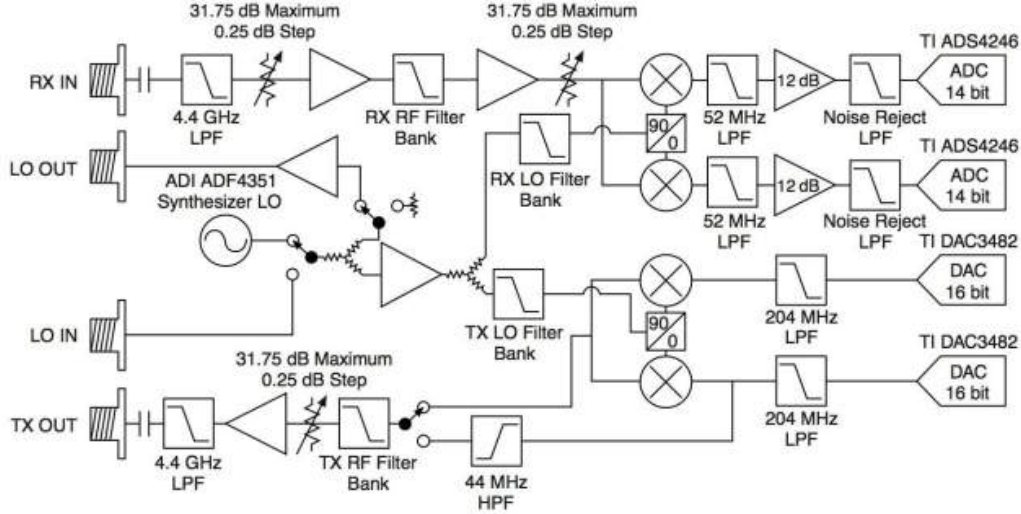


Figure 1: Architecture of NI 5791 (picture taken from the NI data sheet).

readout is in Fig. 2: the two FPGAs digitally generate the signal in the I-Q domain, then the signal is converted to analogue by the four Digital to Analog Converters (DACs) inside the transceivers. The two RF signals are added together by a Wilkinson power divider, attenuated by a programmable attenuator (PXI-5695), and fed into the cryostat. Stainless Steel and Niobium coaxial cables are used inside the cryostat to reduce thermal loading. The signal emerging from the KIDs is divided by another Wilkinson power divider, fed into the two transceivers' inputs and I-Q detected.

The architecture of our readout electronics is a finite state machine organized in three states. The three states can be summarized as:

1. Sweep the frequency to find the resonant tones of the KIDs. This is done by using an up-chirp signal and increasing the frequency over time.
2. Each of the resonant tones is generated by a COordinate Rotation DIGital Computer algorithm (CORDIC),<sup>9</sup> then they are added together to form a comb, which is defined only once and stored into a look-up table.
3. The signal is transmitted and received.

The final output of our electronics are the I and Q signals for each of the frequency (related to each KID). From those signals we perform some tests in order to check the behaviour of each resonant frequency. In addition, we

<sup>†</sup><https://www.ni.com/pdf/manuals/373047b.pdf>

<sup>‡</sup><https://www.ni.com/pdf/manuals/373845d.pdf>

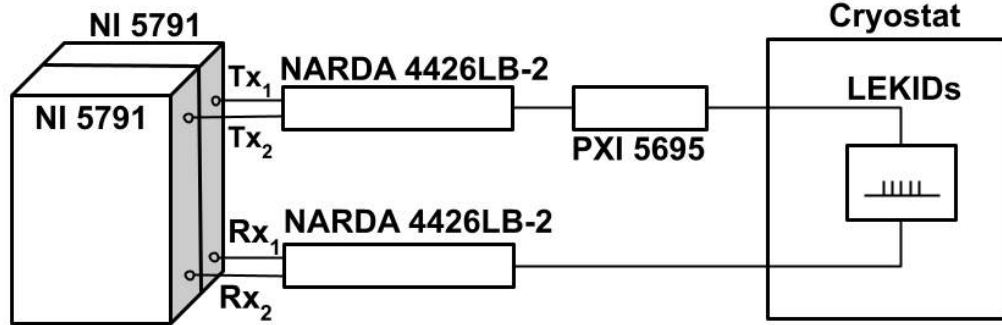


Figure 2: Block-diagram of our readout based on two NI transceivers (model 5791). The two outputs are added by a Wilkinson power divider (Narda 4426LB-2). After that, the sum signal is attenuated by a programmable variable attenuator (PXI-5695) to adjust the power level. The comb signal enters the cryostat by means of a vacuum feedthrough and a sequence of a Stainless Steel coaxial cable and a Nb coaxial cable to minimize the heat load. The same kind of cables are used to reach a second feedthrough. With this set-up there is no need for a LNA. The signals coming out of the cryostat are split with a second Wilkinson power divider before being fed into the two transceivers.



(a) Rack in our lab.



(b) Detail: rack with UPS.

Figure 3: Rack configuration - from the top to the bottom: keyboard, NI crate, rack UPS.

can easily evaluate the amplitude and phase so that we measure the variation of the working point of the KIDs. Each KID resonance frequency is evaluated by means of a Direct Down Converter (DDC) algorithm. The computer we use to acquire data is a workstation precision Dell 3930 Rack, equipped with an Intel core i9 processor, 64 GB of ram and 7.3 TB of memory. Together with the other components, the electronics readout is placed in a rack, as shown in Fig 3.

Since we need both a visual feedback and to set manually some parameters, we implemented a Graphical User Interface (GUI) using a LabView environment, shown in Fig. 4. Our GUI allows the user to monitor the status and easily set FPGA parameters without modifying the software at lower levels. Moreover, we can have a real time plot of the amplitude to have a visual feedback during the first and the third state of the machine. In addition, it is also possible to manually set the comb frequencies, or to select peaks found during the first state sweep corresponding to resonator frequencies. The GUI also greatly simplifies the tuning of the input signal parameters such as the trigger, the output power or the number of samples to be used.

### 3. TEST RESULTS

As said before, we are developing the electronics readout for COSMO, whose detectors will be made by Aluminum to be compliant with the frequencies covered by the experiment.<sup>10,11</sup> However, the cryofacility we have in our

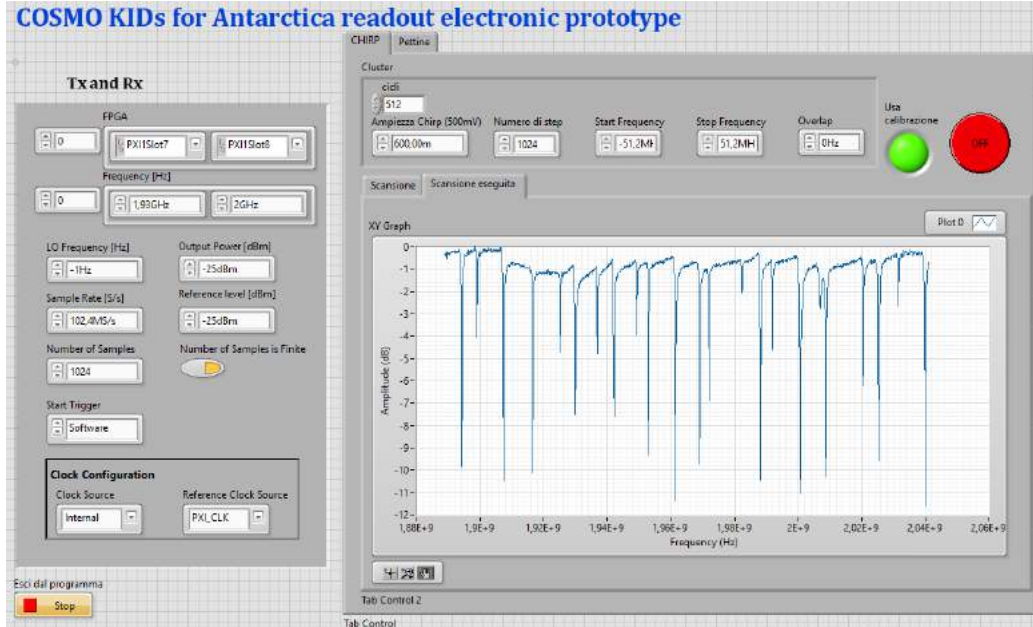


Figure 4: An example of the functionalities of our GUI, which is made to interactively control the readout electronics. The FPGA parameters can be set in the left box, while in the right one we can visualize the real time plot of the first (here), and third state of the machine. We can also set the parameters of the state.

lab, operated by a RDK-408 SHI GM cryocooler, can reach a temperature of around 5 K with the heat load of the current set-up. For this reason we use an array of 25 Niobium KIDs for  $\sim 200$  MHz band around 2 GHz designed at AstroParticule et Cosmologie in Paris and manufactured at Paris Observatory in order to test our electronics with real devices. The transition temperature of these KIDs is around 9 K and their measured quality factor resonances,  $Q$ , is higher than 5000 already at 5 K, the working temperature of our cryofacility. The  $Q$  factor value is enough for our purpose, since we need to have well defined resonances with a frequency spacing around 5-10 MHz.

As shown in Fig. 4, we can detect the 23 tones detectable at 5 K of our KIDs array. We work with two FPGAs, and the separation frequency between the two is 1.9677 GHz. We decided to add a test tone for each FPGA, respectively at 1.9030 GHz for the first, and 1.9760 GHz for the second one. Thus, at the end we can receive and transmit 25 tones in total. We chose these frequencies values for the test tone because there the signal is not attenuated by any other close resonance. The presence of the test tones allows us to check the behaviour of the resonant tones and to have an estimation of the intrinsic noise, which is of the order of about  $10^{-6}$  V.

To date, we can reach a sampling rate of around 12 kHz on the 25 frequencies (23 effective resonances plus 2 test tones) saving in HDF5 format. However, we are still a factor of 5 far from the COSMO requirements (sampling rate at about 60 kHz). Currently we are improving the data saving in order to increase the sampling rate and we are exploring all the possibilities given by the HDF5 format. We got a remarkable improvement also dividing the data in chunk of about the same amount of time corresponding to the one occupied by the sampling frequency. We also plan to improve the data synthesizing the calculus of the amplitude and phase shift of each tone on the FPGA.

During the data saving we also collect the temperatures that have oscillations of  $\sim 20$  mK from the mean value, with a frequency  $\sim 1$  Hz, typical of the cooler. The temperature oscillations make the initial search for resonators difficult and for this reason we need to repeat the sweep multiple times. The aim of this process is to map the oscillations of the resonances and find the minimum transmission. The state of minimum transmission corresponds to the minimum temperature achieved by the cryocooler with the installed set-up and consequentially gives the information about the tone of each resonance. However, these annoying oscillations allows us to test some key parameters of the readout system:

- they are used to verify that the system can track the tones during testing phase;
- their presence is a prominent feature that should be clearly visible in the phase time stream plot (Fig. 5) and in the rolling mean amplitude time stream plot (Fig. 6).

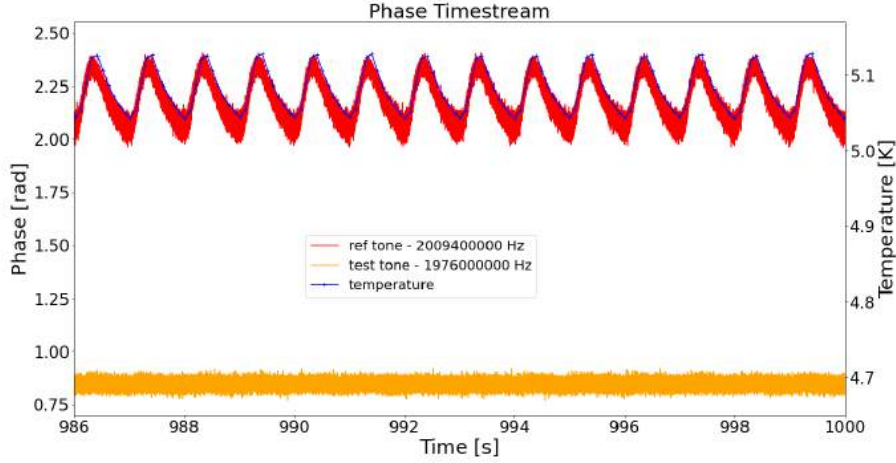


Figure 5: Chunk of the phase time stream. The test tone (frequency 1.976 GHz) is depicted in orange, the resonant tone (2.0094 GHz) is in red and the temperature oscillations are in blue.

In figure Fig. 5 we present a chunk of the phase time stream. We decided to show only the tone at resonant frequency 2.0094 GHz because it is one of the deepest (-11.264 dB), but we have obtained similar wave-forms for all the other frequency tones. In the same plot we report the temperature oscillations and we can notice a sync between this signal and the phase time stream. This evidence confirms that the KID responds correctly with respect to the variation of the quasi-particles density. At the same time, we can also see the behaviour of the test tone (frequency 1.976 GHz), which is not affected by the change of temperature, as expected.

In figure Fig. 6 we present the amplitude time stream of the resonant tone at frequency 2.0094 GHz together

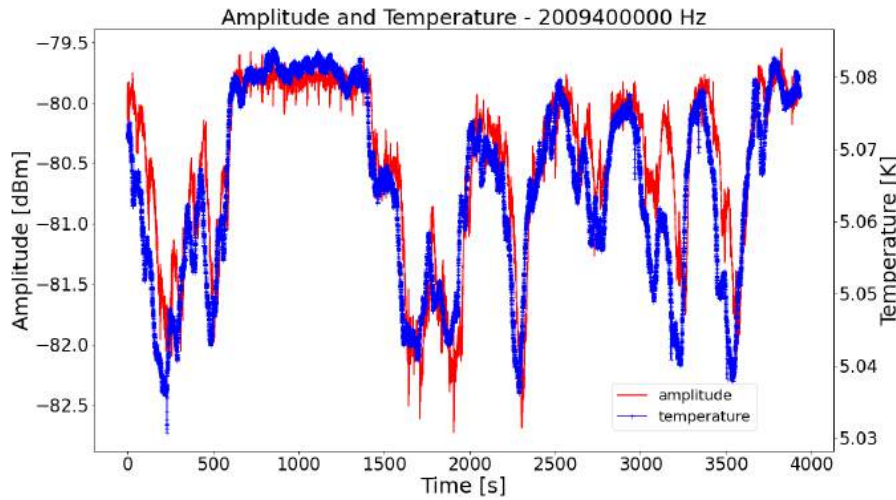


Figure 6: Amplitude and temperature time stream. The resonant tone (2.0094 GHz) is in red and the temperature is in blue.

with the temperature values. As above, we have obtained similar wave-forms for the all the other frequency tones.

We perform a moving average on both the amplitude and the temperature data so that we can see the long time fluctuations of the cooler and not the oscillations, that are averaged away. The period of each window is the sampling rate ( $\sim 12000$  Hz) for the amplitude data, while for the temperature data it is 10, which corresponds to the sensibility of our CTC100 Cryogenic Temperature Controller <sup>†</sup>. As we can see in Fig. 6 the variation of moving average of the amplitude and the temperature are synchronous, as expected.

We performed the noise analysis by comparing the phase noise and the IQ noise ( $\sqrt{I^2 + Q^2}$ ) in three different conditions: when the signal passes through the KIDs, when there are no KIDs (cold loop back), and when the signal does not enter in the cryostat (warm loop back). We report the result for the 2.00940 GHz resonant tone in Fig. 7 regarding the phase noise, while in Fig. 9 for the IQ noise. In Fig. 8 and Fig. 10 we did the same analysis but using the test tone (1.976 GHz).

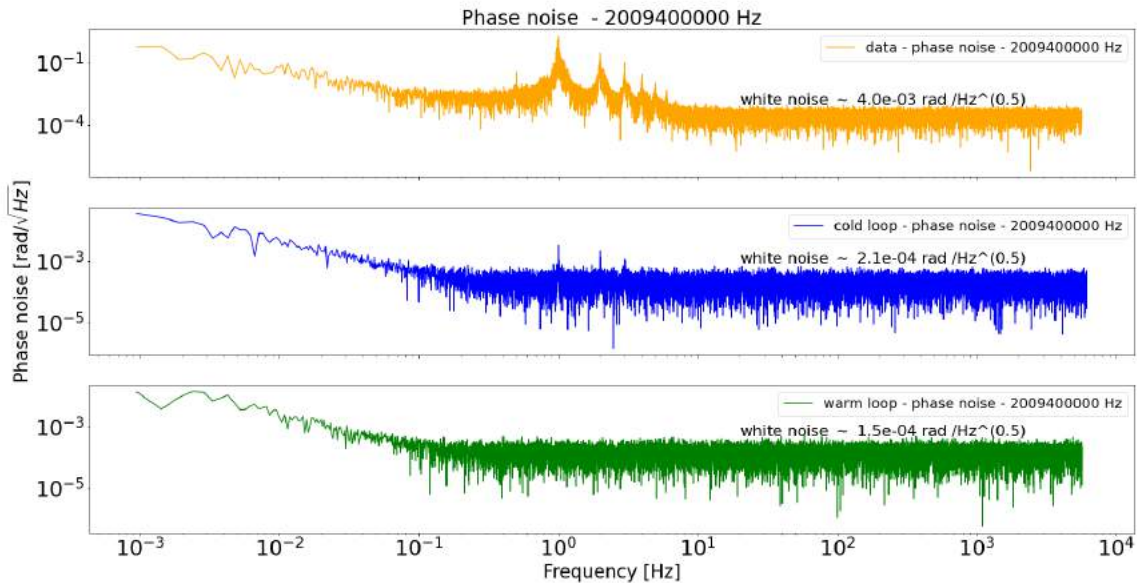


Figure 7: Phase noise of the reference tone (2.00940 GHz) in three different conditions: when the signal passes through the KIDs (upper plot, in orange), when there are no KIDs (cold loop back, central plot in blue), and when the signal does not enter in the cryostat (warm loop back, lower plot in green).

In all the four figures (Fig. 7, Fig. 9, Fig. 8 and Fig. 10) it is possible to notice that the white noise level decreases starting from the upper to the lower plots, since the signal is not attenuated by any resonant frequencies. The level of the test tones (Fig. 8 and Fig. 10) are always lower compared to the reference one (Fig. 7 and Fig. 9), as expected. Moreover the resonant tone and the test tone values and shape are very comparable. Concerning the peak at  $\sim 1$  Hz, we can notice that it is present also in the cold loop back (the blue plots). This is due to the presence of the Nb cables which transmission is slightly modulated by the temperature. For this reason there is no peak in the warm loop back (the green plots).

All these data were collected for about 30 minutes so that it is possible appreciate also the  $1/f$  noise (on the left part of the plots). All the plots end at frequency of about 6 kHz because our sampling rate is around 12 kHz.

#### 4. CONCLUSIONS AND NEXT STEP

With this contribution we demonstrated that we can develop a working readout electronics for KIDs with a modular architecture based on commercial devices which are capable of a bandwidth of 100 MHz per module and a sampling rate (still not optimized) of about more than 12 kHz for 23 effective resonators plus 2 test tones.

<sup>†</sup><https://www.thinksrs.com/products/ctc100.html>

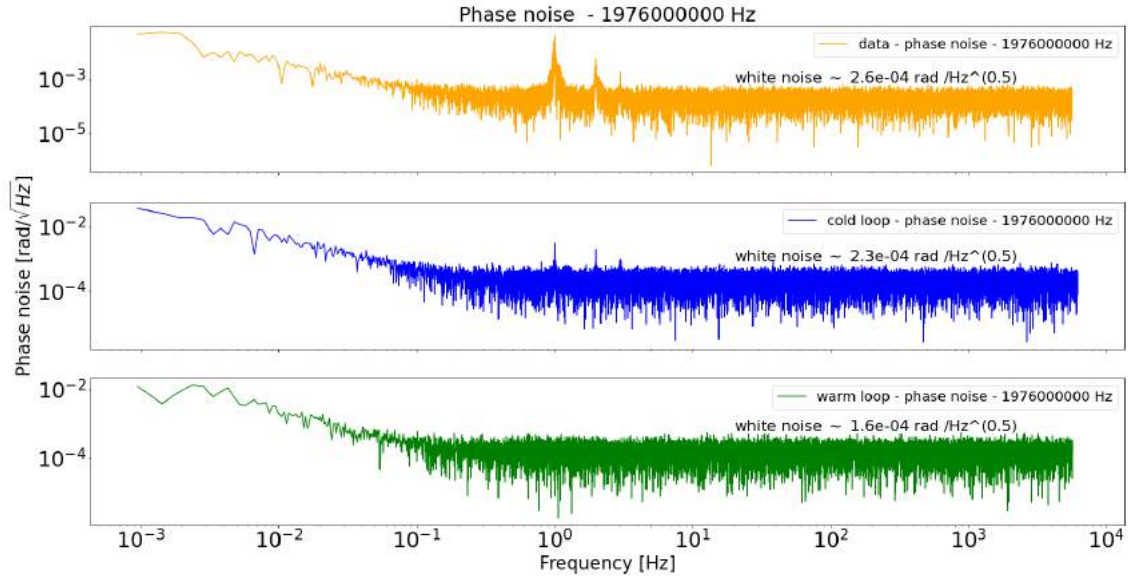


Figure 8: Phase noise of the test tone (1.976 GHz) in three different conditions: when the signal passes through the KIDs (upper plot, in orange), when there are no KIDs (cold loop back, central plot in blue), and when the signal does not enter in the cryostat (warm loop back, lower plot in green).

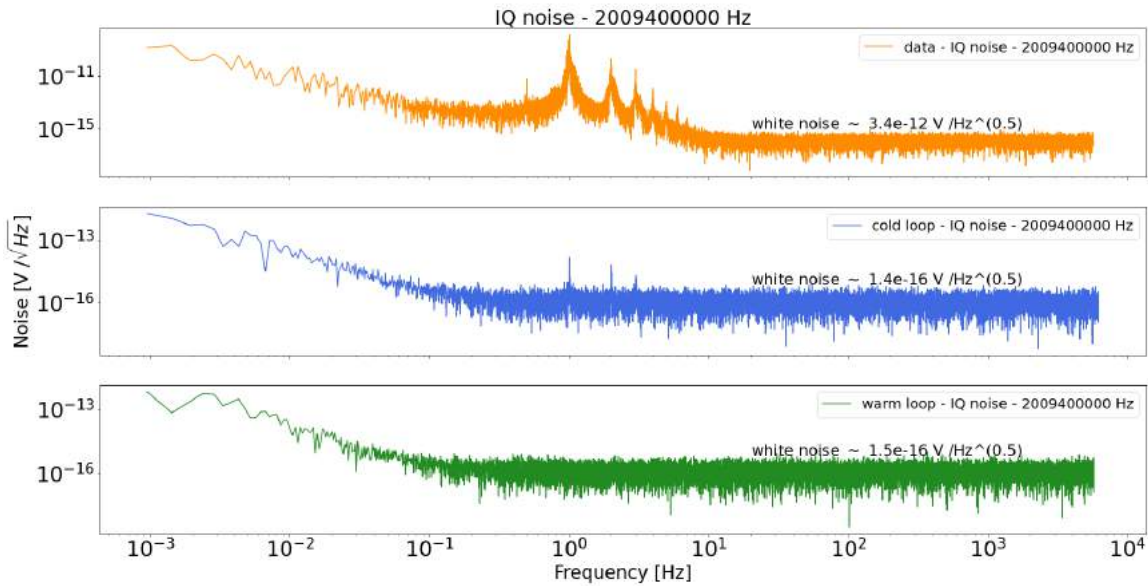


Figure 9: IQ noise of the reference tone (2.0094 GHz) in three different conditions: when the signal passes through the KIDs (upper plot, in orange), when there are no KIDs (cold loop back, central plot in blue), and when the signal does not enter in the cryostat (warm loop back, lower plot in green).

The main advantage of our readout electronics is the access to hardware and software solutions which greatly reduce the time required to realize a working readout chain and to develop a Graphical User Interface. As the next step, we are planning to use a single FPGA with a transceiver with a RF bandwidth wider than the sum of the two implemented in this Set-Up. We think that using two FPGAs slowed down the performance, as they have to share a single data bus, and we can speed up the sampling rate just using a single FPGA.

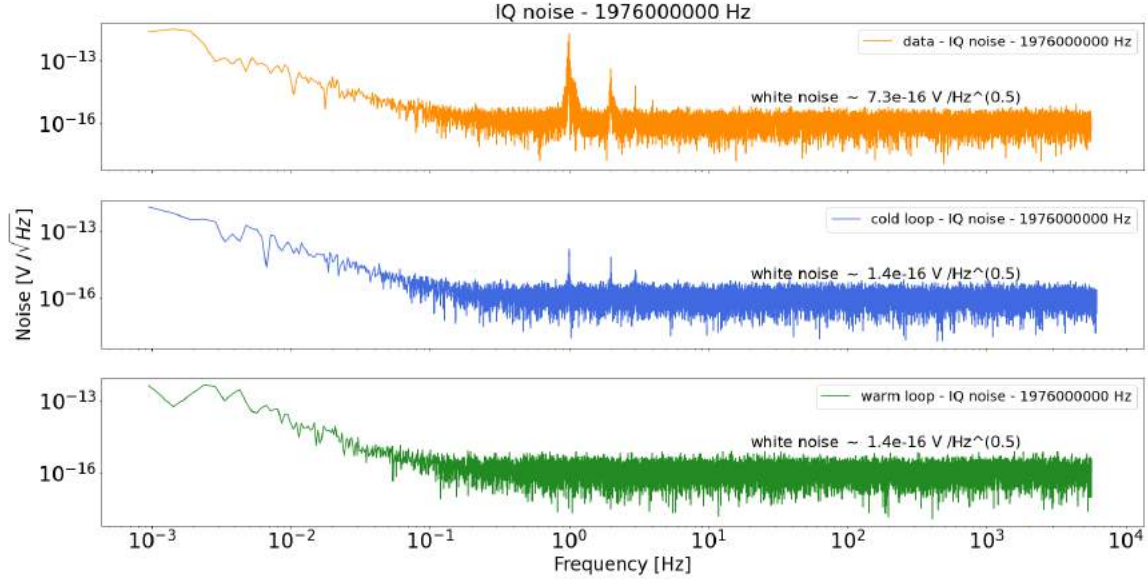


Figure 10: IQ noise of the test tone (1.976 GHz) in three different conditions: when the signal passes through the KIDs (upper plot, in orange), when there are no KIDs (cold loop back, central plot in blue), and when the signal does not enter in the cryostat (warm loop back, lower plot in green).

Finally, a complete NEP investigation will be performed on the COSMO KIDs.

## ACKNOWLEDGMENTS

COSMO is funded by PNRA 14-00063 (Programma Nazionale Ricerche in Antartide) and by PRIN 16-00266 (Programmi di Rilevante Interesse Nazionale). These activities were partially funded by the Italian Space Agency contracts 2016-19-H.0 and 2017-42-H.0. G. Coppi is supported by the European Research Council under the Marie Skłodowska Curie actions through the Individual European Fellowship No. 892174 PROTOCOLC. G. Conenna is supported by PRIN-MIUR 2017 COSMO.

## REFERENCES

- [1] Penzias, A. A. and Wilson, R. W., “A Measurement of excess antenna temperature at 4080-Mc/s,” *Astrophys. J.* **142**, 419–421 (1965).
- [2] Guth, A. H., “Inflationary universe: A possible solution to the horizon and flatness problems,” *Phys. Rev. D* **23**, 347–356 (Jan 1981).
- [3] Sunyaev, R. A. and Zeldovich, Y. B., “Small-Scale Fluctuations of Relic Radiation,” **7**, 3–19 (Apr. 1970).
- [4] Fixsen, D. J., Cheng, E. S., Gales, J. M., Mather, J. C., Shafer, R. A., and Wright, E. L., “The Cosmic Microwave Background Spectrum from the Full COBE FIRAS Data Set,” **473**, 576 (Dec. 1996).
- [5] Zannoni, M., Tartari, A., Gervasi, M., Boella, G., Sironi, G., Lucia, A. D., Passerini, A., and Cavaliere, F., “TRIS. i. absolute measurements of the sky brightness temperature at 0.6, 0.82, and 2.5 GHz,” *The Astrophysical Journal* **688**, 12–23 (nov 2008).
- [6] Kogut, A., Fixsen, D., Fixsen, S., Levin, S., Limon, M., Lowe, L., Mirel, P., Seiffert, M., Singal, J., Lubin, P., and Wollack, E., “ARCADE: Absolute radiometer for cosmology, astrophysics, and diffuse emission,” *New Astronomy Reviews* **50**, 925–931 (dec 2006).
- [7] Masi, S., Battistelli, E., de Bernardis, P., Coppolecchia, A., Columbro, F., D’Alessandro, G., De Petris, M., Lamagna, L., Marchitelli, E., Mele, L., Paiella, A., Piacentini, F., Pisano, G., Bersanelli, M., Franceschet, C., Manzan, E., Mennella, D., Realini, S., Cibella, S., Martini, F., Pettinari, G., Coppi, G., Gervasi, M., Limonta, A., Zannoni, M., Piccirillo, L., and Tucker, C., “The COSmic Monopole Observer (COSMO),” *arXiv e-prints*, arXiv:2110.12254 (Oct. 2021).

- [8] Mazin, B. A., Day, P. K., Zmuidzinas, J., and Leduc, H. G., “Multiplexable kinetic inductance detectors,” *AIP Conference Proceedings* **605**(1), 309–312 (2002).
- [9] Volder, J. E., “The cordic trigonometric computing technique,” *IRE Transactions on Electronic Computers* **EC-8**(3), 330–334 (1959).
- [10] Paiella, A., Coppolecchia, A., Castellano, M., Colantoni, I., Cruciani, A., D’Addabbo, A., Bernardis, P., Masi, S., and Presta, G., “Development of lumped element kinetic inductance detectors for the w-band,” *Journal of Low Temperature Physics* **184** (07 2016).
- [11] Paiella, A., Battistelli, E. S., Castellano, M. G., Colantoni, I., Columbro, F., Coppolecchia, A., D’Alessandro, G., de Bernardis, P., Gordon, S., Lamagna, L., Mani, H., Masi, S., Mauskopf, P., Pettinari, G., Piacentini, F., and Presta, G., “Kinetic inductance detectors and readout electronics for the OLIMPO experiment,” *Journal of Physics: Conference Series* **1182**, 012005 (feb 2019).